HIERARCHICAL CONTROL STRATEGIES FOR SPATIOTEMPORALLY VARYING SYSTEMS WITH APPLICATION TO AIRBORNE WIND ENERGY

by

Alireza Bafandeh

A dissertation submitted to the faculty of
The University of North Carolina at Charlotte
in partial fulfillment of the requirements
for the degree of Doctor of Philosophy in
Mechanical Engineering

Charlotte

2018

Approved by:

_____
Dr. Christopher Vermillion

_____
Dr. Scott Kelly

_____
Dr. Russell Keanini

_____
Dr. Tao Hong

_____
Dr. Yogendra Kakad

Abstract

ALIREZA BAFANDEH. Hierarchical Control Strategies for Spatiotemporally Varying Systems with Application to Airborne Wind Energy. (Under the direction of DR. CHRISTOPHER VERMILLION)

Wind energy represents a leading renewable resource for the production of clean and sustainable electricity for on- and off-grid networks. Nevertheless, tower and foundation costs, which typically represent about 30 percent of the total installation cost of existing wind turbines, limit the operating altitude (hub height) of conventional turbines to no more than 220m. Consequently, conventional systems are not able to utilize significantly stronger winds that are present at higher altitudes. Airborne wind energy (AWE) systems eliminate both the tower and foundation by using tethers and a lifting body to reach higher altitudes where stronger wind exists. In the target installation sites, it is desirable to maximize the percentage of total energy generated from the wind, recognizing that the AWE system will need to be supplemented with conventional sources. This leads to two critical control challenges: (i) Optimizing the operating altitude of an AWE system to maximize the energy generated from the wind and (ii) developing a supervisory controller for an integrated AWE-battery-generator system, recognizing that the optimal control of the overall system requires strategic coordination of the three elements.

This dissertation describes and validates, using real wind data, a statistical modeling and hierarchical control approach to addressing the aforementioned challenges. Specifically, physics-driven models are used to characterize the AWE system itself, whereas statistical models are used to characterize the stochastically varying wind profile and electricity demand. A hallmark of the proposed modeling approach lies in the development surrogate regret metrics from these statistical models (termed the energy deficit metric for a stand-alone AWE system and generator excess metric for the integrated system), which provide estimates of the difference between the

optimal output of the system and the existing output of the system. Ultimately, these surrogate regret metrics are used to manage a balance between exploration and exploitation of the spatiotemporally varying environment, through several novel candidate hierarchical control structures. Each of the hierarchical control structures fuses coarse, global control at an upper level with fine, local control at a lower level, using a combination of model predictive control and extremum seeking tools.

ACKNOWLEDGEMENTS

Firstly, I would like to express my sincere gratitude to my advisor Dr. Chris Vermillion for the continuous support of my Ph.D study and related research, for his kind heart, patience, motivation, and immense knowledge. His guidance helped me in all the time of research and writing of this dissertation. I could not have imagined having a better advisor and mentor for my Ph.D study.

Besides my advisor, I would like to thank the rest of my thesis committee: Dr. Russell Keanini , Dr. Scott Kelly, and Dr. Tao Hong.

My sincere thanks also goes to Dr. Hosam Fathy and Dr. Scott Moura, who provided me helpful comments and hints.

I thank my fellow lab mates for the stimulating discussions, for the endless meetings we had about our research achhievements and obstacles, and for all the fun we have had in the last two years. Also I thank my friends in the Altaeros Energies. In particular, I am grateful to Mr. Ben Glass, who provided me an opportunity to join their team as intern, and who gave access to the laboratory and research facilities.

Last but not the least, I would like to thank my family: my wife, my parents and my brother and sisters for supporting me spiritually throughout writing this dissertation and my life in general.

Contents

List of Figures

List of Tables

Nomenclature

μ	mean of wind velocity
ω_H	high-pass filter frequency
σ	standard deviation of wind velocity
θ	pitch angle
β_i	coefficients of linear regression model
ϵ	switching threshold in LSES
η	low-level noise
η_{bat}	efficiency of the battery
η_g	regenerative efficiency of the winches
η_m	efficiency of the motors of winches
γ	amplitude shrink factor in LSES
$\mathbf{D}$	matrix of previous wind velocity measurements
$\mathbf{x}_{DP}$	dynamic programming states
ω	perturbation frequency
ω_L	low-pass filter frequency
ϕ	roll angle
ξ	filtered control input
A	rotor area
a	perturbation amplitude

a_0 full-size perturbation amplitude

A_{ref} reference area for calculating lift

C_L lumped coefficient of lift

C_P power coefficient of turbine

$C_{\mathbf{b}}$ battery state of the charge

$C_{\mathbf{max}}$ maximum capacity of the battery

D_t day of the week

$E_{\mathbf{bat}}$ energy discharged from the battery

$E_{\mathbf{d}}$ generator energy deficit

$E_{\mathbf{gen}}$ energy from auxiliary generator

F_b buoyant force

H_t hour of the day

$I_{\mathbf{lb}}$ lower boundary of the confidence interval

$I_{\mathbf{ub}}$ upper boundary of the confidence interval

J_a Jacobian used in LSES

K integrator gain

k time-step

k_2 coefficient of power required to maintain the altitude in energy generation model

k_3 coefficient of power required to change the altitude in energy generation model

L total lift force

M_t month of the year

m_0 coefficient in calculation of standard deviation

m_1 coefficient in calculation of standard deviation

m_2 coefficient in calculation of standard deviation

$M_{\mathbf{sur}}$ surrogate generator excess energy

n number of altitude bins

n_f number of single forecasts

N_{DP} number of function evaluations for DP

N_{exh} number of function evaluations for exhaustive search

p uncertaintainty quantization level in DP

$P_{\mathbf{gen}}$ generator power expenditure

P_w wind turbine power output

P_{act} actual power deficit

P_{cur} current power output

P_{net} net power output

P_{sur} surrogate power deficit

P_{tur} wind turbine power output

Q_l electricity demand

r number of allowable altitudes in DP

r_{max} maximum rate of change in altitude

T ambient temperature

V Lyapunov function in LSES

v_{r} rated wind speed of the turbine

v_{w} wind velocity

v_{ave} average tether release speed

x_a average state variable

z altitude

z^* optimum altitude

z_{sp} altitude setpoint

ARIMA autoregressive integrated moving average method

AWE Airborne Wind Energy

BAT Buoyant Airborne Turbine

DP dynamic programming

GLSES globalized LSES

KNN K nearest neighbors method

LSES Lyapunov-based switched extremum

MLR multiple linear regression method

MPC model predictive control

PJM Pennsylvania, Jersey, Maryland Power Pool

CHAPTER 1: Introduction

1.1 Wind Energy, Clean and Cheap

According to the U.S. Energy Information Administration [10], renewable energy accounted for more than 10% of total energy consumption and about 15% of total electricity generation in United States in 2016. These figures, along with numerous studies, show that the fossil fuels are being replaced by renewable energy resources. Wind is one of several clean and renewable resources with the capacity for displacing fossil fuels. According to the American Wind Energy Association, the total energy produced by wind turbines exceeded 5.5% of total US electricity generation in 2016 [11]. These facts and statistics demonstrate that wind energy is becoming a significant player in the U.S. energy market.

1.1.1 Components of a Contemporary Wind Turbine

A typical wind turbine has the following components, which are shown in Figure 1.1: Anemometer, blades, brake (mechanical, electrical, or hydraulic), gear box, generator, high-speed shaft, low-speed shaft, nacelle, rotor, tower, wind vane, yaw drive, and yaw motor.

The capital cost breakdown of these components is shown in Figure 1.2. It can be seen that tower and foundation parts of a contemporary wind turbine are costly and restricting, often representing as much as a one third of the whole system cost, and more in remote environments [2]. Additionally, tower heights limit the achievable altitude, whereas wind usually is stronger at higher altitudes. Transportation and installation of the tower, along with implementation of the foundation, is time

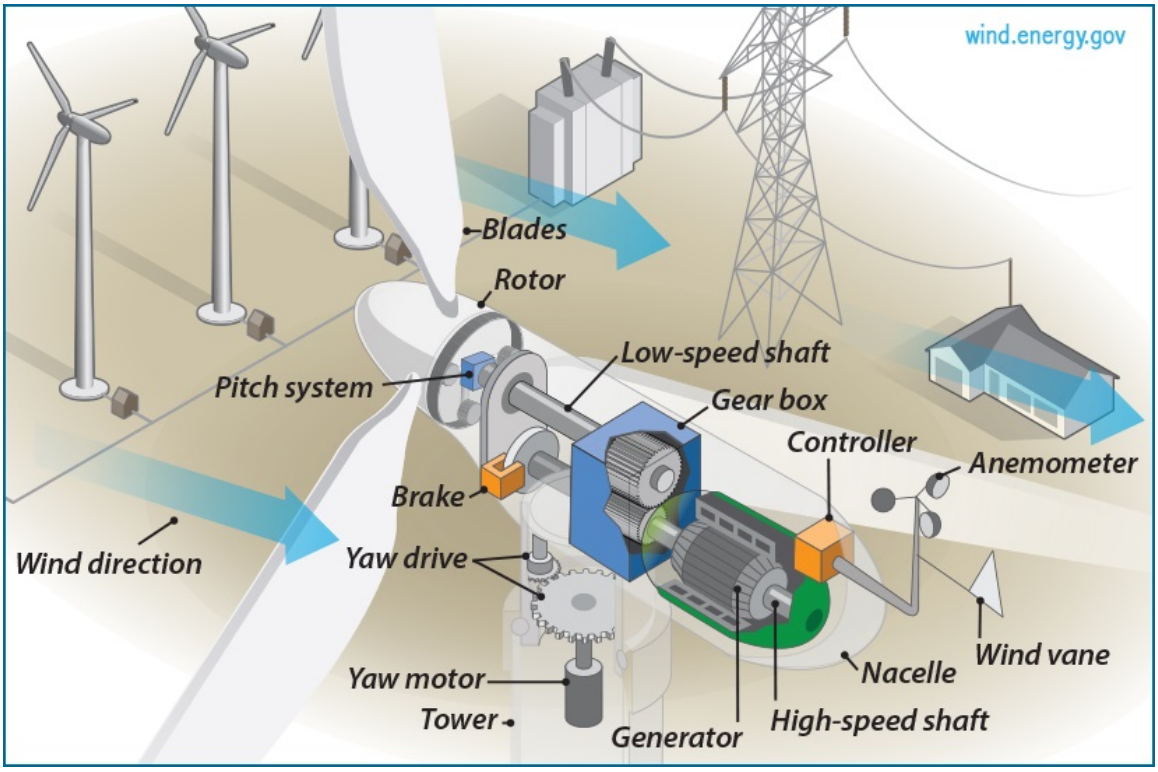

Figure 1.1: Components of a wind turbine (U.S. Department of Energy [1])

consuming and takes three to five months. These deficiencies of conventional wind turbines motivate the need to develop a new system without the tower. The next section introduces the technology of Airborne Wind Energy (AWE) systems, which accomplishes this precise objective.

1.2 Airborne Wind Energy Systems

Wind is generally stronger and more consistent as the altitude from Earth's surface increases. Since wind power is a function of wind speed cubed, it is desirable to operate a wind turbine at as high an altitude as possible to maximize the power production. Joby Energy Inc. ([3]) has modeled tropospheric winds using the available worldwide data for the years between 1979 and 2008, and developed global maps of wind speed and wind power. Two sample global average wind power density maps are

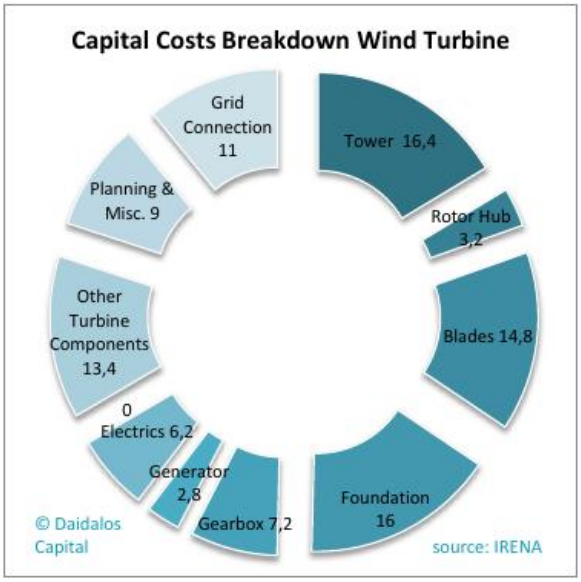

Figure 1.2: Capital cost breakdown of a typical wind turbine (The International Renewable Energy Agency [2])

displayed in Figure 1.3. These maps indeed show that a significant increase in power production will occur by moving the wind turbine to a higher altitude. In particular, installing wind turbines at altitudes of 600 m or greater introduces many more attractive potential wind farm sites. At these new heights, the energy production will be high enough to economically justify an investment.

However, the higher altitude means a taller and heavier tower, and consequently a stronger foundation. As a result, it is not cost effective to install a towered wind turbine at these altitudes due to the extreme tower and foundation expenses. To mitigate these extreme costs and still achieve high altitude operation, airborne wind energy systems are being developed. The idea is to install the wind turbine on a *lifting body* (a wing or aerostat) in order to reach higher altitudes and harness wind energy with less cost. This type of wind system is called an Airborne Wind Energy (AWE) system.

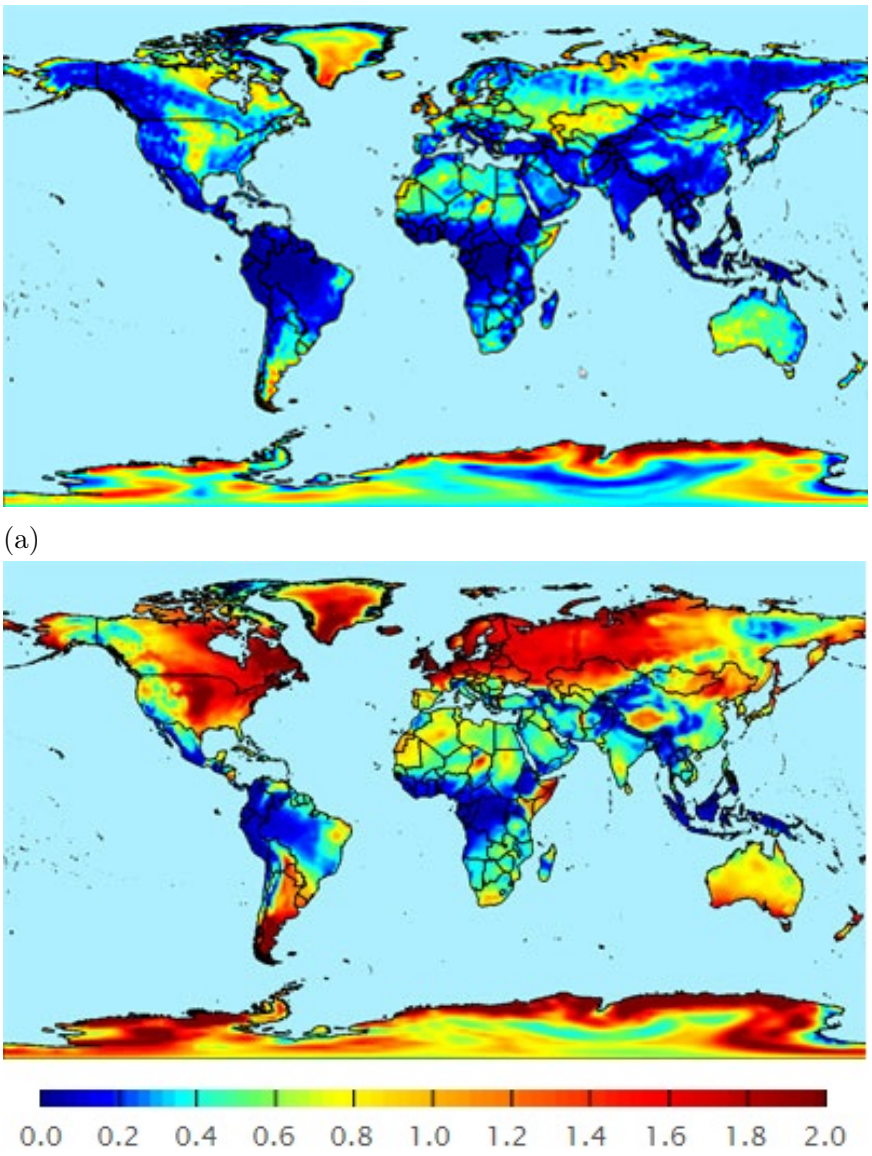

(a)

(b)

Figure 1.3: Global average wind power density in kW/m^2 for altitudes of (a) 120 m (400 ft) and (b) 600 m (2000 ft) [3].

1.3 Description of the Technology

AWE systems replace conventional towers with tethers and a lifting body (a kite, aerostat, or rigid wing). In comparison with conventional systems that operate at fixed altitudes, it is possible to adjust the altitude of an AWE system in order to reach wind speeds that align more closely with the rated wind speed of the turbine. This ability enables tethered systems to reach capacity factors of 50 percent or greater (compared to 20-30 percent capacity factors seen by conventional systems) [12], while operating with relatively high rated wind speeds and avoiding excessive wind speeds.

Researchers explored the use of wind turbines installed on kites as power sources as early as the 19th century. However, Miles Loyd was the first person who quantified the potential power production from airborne wind energy systems in 1980 [13]. There are two major ways to harness the wind energy from tethered systems. In first setup, the generated electricity must be transferred to the ground via conductive cables. This approach is called *Fly-Gen*. Another technique considered by Loyd is to use the force exerted by the lifting body on the tethers to generate the electricity using equipment on the ground station, which is known as a *Ground-Gen* system. While companies including Altaeros Energies [6], Google-based Makani [5], and Sky Windpower [14] are developing systems which the generator is on the lifting body (Fly-Gen), some other companies including Ampyx Power[15], Enerkite, Kitegen Research, Kitenergy [16], and Windlift [17] generate electricity on the ground (Ground-Gen).

1.3.1 Ground-Gen Airborne Wind Energy Systems

A Ground-Gen AWE system operate in a two phase cycle. Electrical energy is produced during the generation phase, while a small amount is consumed during the recovery phase. A rope connected to the aircraft is wound around a winch that is connected to an electric generator. The aircraft produces a lift force that, in turn,

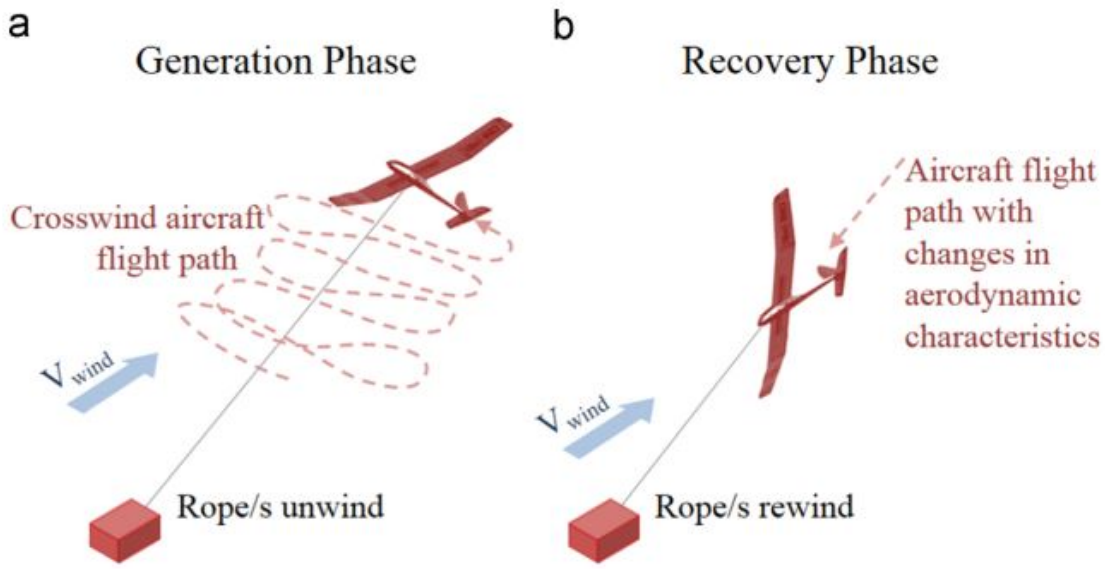

Figure 1.4: Generation phase and recovery phase of Ground-Gen airborne wind energy systems [4]

produces the traction force, resulting in the rotation of the generator. During the traction phase, a crosswind flight pattern is ideal because it maximizes lift, thereby maximizing tether tension (Figure 1.4 (a)).

It is important that the generation phase produces more electrical energy than the recovery phase consumes; ideally much more than the amount being consumed. The crosswind flight mode produces a greater apparent wind on the aircraft, which results in increased tension on the rope. During the recovery phase (Figure 1.4 (b)), motors rewind the ropes to place the aircraft back into its original position in the sky.

1.3.2 Fly-Gen Airborne Wind Energy Systems

Fly-gen AWE systems produce electricity in the sky and transmit it to the ground station using conductive cable(s). In these systems, a wind turbine is installed on the wings of the plane (Figure 1.5 (a)), Aircraft (Figure 1.5 (b)), inside an aerostat body (Figure 1.5 (c)), or in another configuration like the quadrotor shown in Figure 1.5 (d). The wind power harnessed by the rotor is converted to electricity via an airborne

generator. This electrical power is conditioned by an inverter and transformer to reduce the electrical and heat waste inside the cables. Finally, electricity is transmitted to the ground station and delivered to the grid or storage system there.

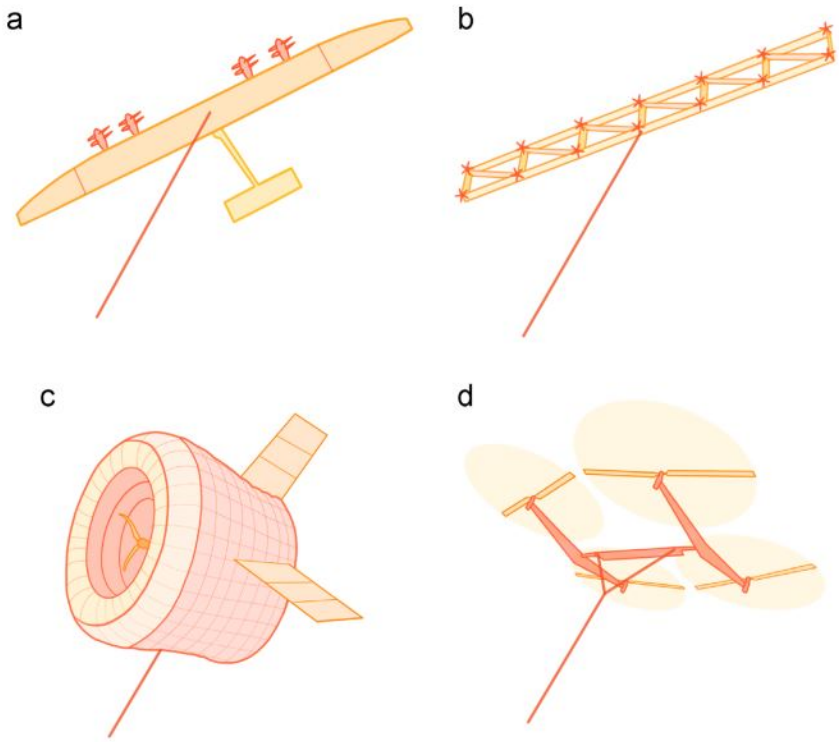

Figure 1.5: Different configurations of Fly-Gen systems. (a) Plane with four turbines, designed by Makani Power [5]. (b) Aircraft composed of a frame of wings and turbines, designed by Joby Energy [3]. (c) Toroidal lifting aerostat with a wind turbine in the center, designed by Altaeros Energies [6]. (d) Static suspension quadrotor in auto rotation, designed by Sky WindPower [4].

1.4 Control Opportunities for AWE Systems

There are two main mechanisms in the AWE literature for enhancing the energy output of an AWE system: (1) moving the system in a crosswind motion by controlling the aerodynamic surfaces and tethers, and (2) optimizing the operating altitude of the AWE system.

Figure 1.6: Altaeros Buoyant Airborne Turbine (BAT) [6]

1.4.1 Crosswind Flight

A large body of research focuses on applying crosswind motion to kite- and wing-based systems in order to increase net energy output. For example, the generation operating cycle of a KiteGen system, whose design is described in [18, 19, 20, 21], is optimized in [22]. In [23], the non-convex optimal control problem of kite-based AWE systems is replaced with a convex problem by introducing fictitious forces and moments at critical stages of the dynamics. Traction force and output power of a ground-based AWE system are maximized in [24] and [25] by optimizing general crosswind path parameters. Similarly, [26] optimizes the way-points that describe an AWE system's figure-8 crosswind path using an iterative learning control-based approach. Authors of [27] show that the optimal performance under crosswind motion occurs on the verge of closed-loop instability of the system. In [28] flight characteristics of a laboratory-scale model of Altaeros Buoyant Turbine (BAT) are studied in a water channel experimental setup. The same setup was used by [29] to evaluate the closed-loop optimal control of a multi-tethered aerostat in crosswind motion. Crosswind

motion has been also studied by other researchers in [30, 31, 32, 33, 34].

1.4.2 Optimize the Operating Altitude Trajectory

The possibility of harnessing more energy from wind by adjusting the altitude of the AWE system is studied in a relatively smaller body of literature. Prior to the research described in this dissertation, those who have examined the impact of altitude adjustment ([35],[36]) had assumed a deterministic, monotonic wind shear profile (wind velocity vs. altitude), which implies that the optimal operating altitude is predictable (in reality, it is not, as evidenced by data presented in this work).

1.5 The Key Challenges in Altitude Optimization of AWE Systems

This section explores the key challenges in optimizing the operating altitude of an AWE system to maximize the net power generation. First, we economically evaluate the methods available for measuring the wind shear profile in real-time. Then, the two main challenges in developing an optimal control solution to the altitude optimization problem are introduced. These challenges originate from a spatiotemporally varying and partial observable wind environment.

1.5.1 Why not simply measure the wind shear profile?

One may pose the following question: "If flying at an altitude where $v_{\mathrm{w}} = v_{\mathrm{r}}$ is so important, why not simply use a weather balloon or other type of wind speed measurement device to measure the instantaneous wind velocity at different altitudes (wind shear profile) instead of designing and implementing a controller that hunts for the optimal altitude?"

Light Detection and Ranging (LiDAR) and Sonic Detection and Ranging (SODAR)

systems are Doppler effect measurement devices, which can be used to measure the wind velocity remotely. Another approach for measuring the wind speed involves installing and moving a weather balloon continuously to explore the space and measure the wind velocity for different altitude in a short time. Unfortunately, according to Report no. 79 published by World Meteorological Organization, the hourly cost of using a wind profiler to measure the wind velocity in an onshore site is about 12.39 € ($ 13.85) per hour [37]. The operation and maintenance of the profiler during the lifetime of AWE system is another issue that must be considered. On the other hand, developing a control system to optimize (in real-time) the power production of the AWE system is a one-time effort that can utilize the available wind measurements from the on-board anemometer that is already part of the system.

Table 1.1 shows a preliminary cost comparison for different wind profiling technologies, including LiDAR, SODAR, and a weather balloon to map the wind velocity at different altitudes. An interest rate of 5% is considered in the calculation of cost. It is also worth noting that the LiDAR system of Table 1.1 is only capable of measuring wind speeds up to 200 m. Hence, the cost of a LiDAR system that is capable of measuring wind speeds up to 1500 m is likely to be even higher.

Table 1.1: Cost Comparison for Different Technologies of Mapping Wind Velocity

Technology	Capital Cost	Annual Operational Cost	Total Cost
LiDAR [38]	$190,000	$32,000	$588,790
SODAR [37]	$990,000	$36,000	$1,634,000
Weather Balloon	$10,000	$10,000	$134,620

For the weather balloon approach, the costs of winches and cabling have also been considered in the cost. Altaeros Energies estimates that the total cost of an AWE system of 30kW capacity will be around $500,000. It can be seen that the cost of the wind profiling hardware is considerable compared to the total cost of an AWE system. Additionally, there are potential issues that could arise during operation of

the wind profiling hardware. This motivates a control strategy that determines an optimum altitude in real-time, using sensors that are already available, as opposed to measuring the wind velocity at all altitudes within the working domain.

1.5.2 Partial observability

The previous subsection shows that it is not economically feasible to measure the wind shear profile during the operation of an AWE system. Hence, wind speed is only measurable with the anemometer or other wind measurement devices that are installed on the AWE system. This means that the wind velocity is only known at the operating altitude of the system, and the wind speed at other altitudes is unknown. This makes the altitude optimization of AWE systems a partially observable problem.

1.5.3 Wind shear profile changes spatially and temporally

The optimal altitude for maximizing the net energy production in an AWE system changes dynamically with the *wind shear* profile (i.e., wind speed vs. altitude). The wind shear profile at lower altitudes is often assumed to follow a monotonic structure, conforming closely to either a power law or logarithmic approximation [39]. However, while these simplified wind shear models have been proven accurate for the prediction of *average* wind shear profiles over long periods of time, they are often extremely inaccurate for predicting *instantaneous* and *short-term* wind shear profiles. One example of the non-conformity of the wind shear profile to well-known power and logarithmic laws lies in the presence of low-level jets [40, 41]. Fig. 1.7 shows the instantaneous wind shear profile based on the data from a wind profiler in Cape Henlopen State Park in Lewes, Delaware [7]. This figure shows a complex wind shear profile between 100 m and 1600 m in the presence of a low level jet, which is an especially common occurrence during warmer months.

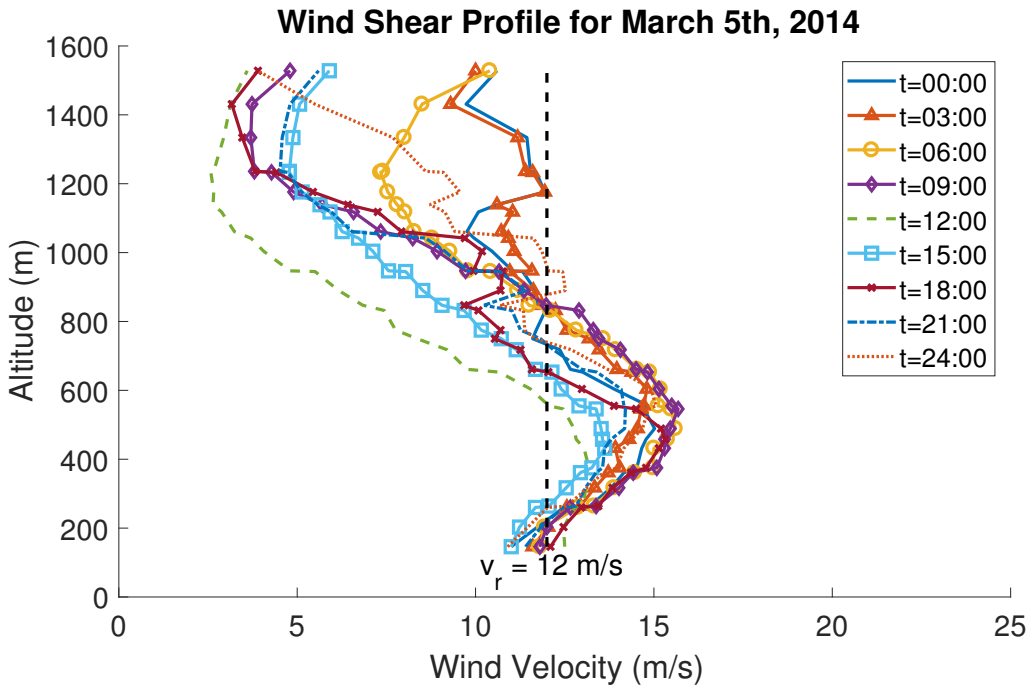

Figure 1.7: Instantaneous wind shear profile based on the data obtained from Dr. Archer's group at the University of Delaware [7]

This figure clearly shows that the wind shear profile is not only monotonic, but also temporally varying [42]. Therefore, altitude optimization of AWE systems is a challenging real-time optimization problem that must be solved in a spatiotemporally varying, partially observable environment.

1.6 Problem Statement

The wind turbine of an AWE system, like all the other wind energy systems, has a rated wind speed (v_r) at which the power production is maximized. Higher wind speeds will not increase the amount of energy produced, but they will increase the lift and drag forces to the lifting body. Consequently, the amount of energy required to control the altitude of the airborne system will increase due to bigger forces, resulting in reduced net energy production. As a result, it is desirable to find the altitude at

which the wind velocity is closest to the rated wind speed rather than just searching for the altitude with the fastest wind. Fig. 1.8 compares the power curves for the wind turbine alone and the net power output of a 100kW BAT with rated wind speed of $12\frac{m}{s}$, operating at a constant altitude. This figure shows an increasing difference between the net output power of the full AWE system and the power generated by the wind turbine alone. This difference arises because a portion of the energy output of the turbine is required to reject typical levels of atmospheric disturbances. Additionally, while the power production of the turbine alone remains constant for velocities greater than the rated wind speed (v_{r}), the net power generation of the AWE system *decreases* in this region because the energy required to maintain altitude in the presence of disturbances increases with wind velocity squared (v_{w}^2).

Because the wind shear profile is partially observable (wind speed is only measured at the AWE system's operating altitude), optimizing altitude involves a balance between exploration and exploitation. Exploration involves physically adjusting the AWE system's altitude to maintain an accurate estimate of the wind shear profile. Exploitation, on the other hand, involves operating at the estimated optimal altitude. Furthermore, for an integrated AWE-battery-generator system, it is possible to prioritize exploration during times of low electricity demand and high energy storage (when large amounts of wind energy production are unnecessary) and prioritize exploitation during high electricity demand or low energy storage (when large amounts of wind energy production are highly valuable).

In light of these challenges, this dissertation focuses on two key problems in the optimal control of an AWE system:

1. Optimization of the operating altitude of an AWE system in a partially observable, spatiotemporally varying wind environment;

2. Optimal control of an integrated AWE-battery-generator system.

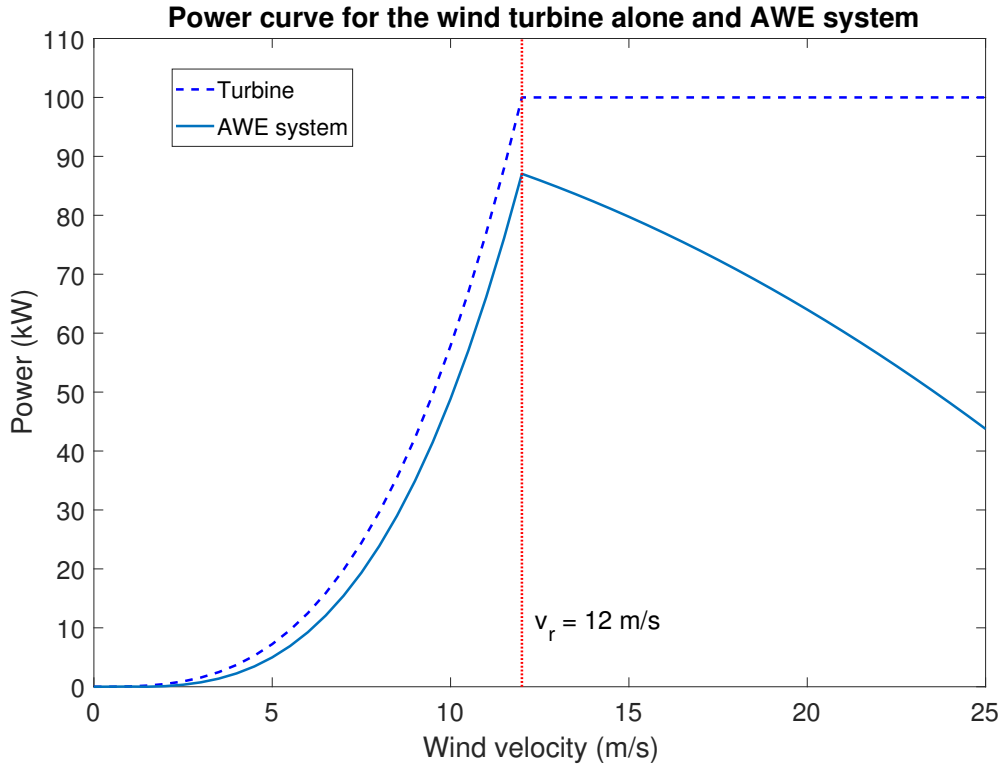

Figure 1.8: Sample power output curve for the wind turbine alone and the full AWE system. The maximum instantaneous power of the AWE system is produced when the wind speed is close to v_{r}, since greater wind speeds require more energy to reject the disturbance and control the AWE system to desired altitude set-point under typical turbulence levels.

For this purpose, an integrated AWE system consisting of a $100kW$ Altaeros Buoyant Airborne Turbine (BAT), a battery storage system and an auxiliary generator are considered (see Figure 1.9).

1.7 Proposed Solution

For the purpose of optimally controlling an integrated AWE system, two candidate "core" control tools are used in this dissertation, namely Lyapunov-based extremum seeking (LSES) and model predictive control (MPC). These control tools are detailed in Chapter 4. Comparing LSES and MPC control schemes, LSES is computationally

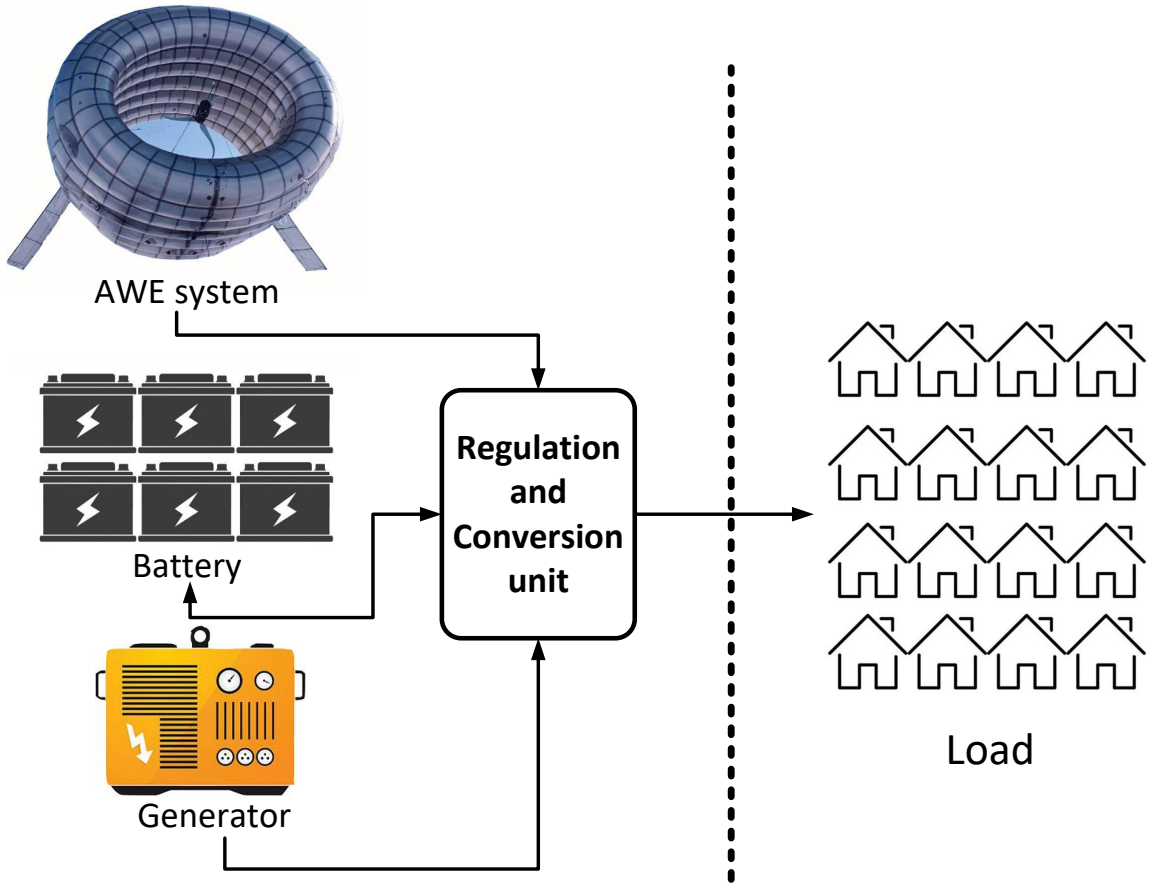

Figure 1.9: Schematic of an integrated AWE system including the airborne turbine (here Altaeros BAT [6]), battery, and auxiliary generator ([8]).

cheap but only guarantees convergence to the local optimum. On the other hand, MPC can use a global optimization which is capable of accounting for statistical and historical measurements. However, achieving global optimality is contingent upon using an exhaustive search or dynamic programming (DP) optimization for the MPC operation. Not only is this computationally burdensome, but it is only global up to the finite horizon length of the MPC optimization and the grid resolution used by the underlying optimization technique. Unfortunately, fine grid resolution and long horizon length wreak havoc on computational complexity. Based on these observations, a fused hierarchical structure incorporating both LSES and MPC is introduced and evaluated in this dissertation to leverage pros and address cons of the two control techniques.

This hierarchical structure is based on a coarse, global optimization technique at an upper level and a fine, local one in a middle control level. The low-level controller in this proposed hierarchy is the flight controller. The structure of this controller and the candidate control tools for each level of hierarchy used in altitude optimization problem, are introduced in Subsections 1.7.1 and 1.7.2, respectively.

The power produced by renewable energy systems depends on the availability of the renewable resource. The varying nature of wind velocity causes fluctuations in the power delivery of an AWE system. Hence, a high-penetration AWE system typically must be integrated with an energy storage system. The ultimate objective for an integrated AWE-battery-generator system is to minimize the excess energy that is required from the auxiliary generator in addressing the electricity demand. Therefore, in addition to developing controllers that seek to to maximize the net power production of an AWE system, another set of candidate hierarchical structures that minimize the excess generator energy have also been developed in this research. These controllers are evaluated for both standalone and integrated AWE systems, and are detailed in Chapters 5 and 6, respectively.

1.7.1 Hierarchical Control Structure for Altitude Optimization of an AWE System

For altitude optimization of an AWE system, multiple candidate controllers are built on a simple hierarchical strategy wherein a global (up to the horizon length and grid resolution) computation provides an input to a fine, local controller. For the hierarchical architectures considered in this work, Table 1.2 shows the controller options for upper and middle levels. In the first candidate control strategy, an upper-level coarse, global MPC selects an altitude set-point that dictates the local domain of altitudes that can be explored by a mid-level LSES controller. In the second candidate strategy, an upper-level coarse, global MPC selects an altitude that dictates the local domain of altitudes that can be explored by a fine mid-level MPC optimization. In these two controllers, the upper level MPC finds the global optimum up to the grid resolution and finite horizon length, and the mid-level controller explores within the optimal altitude "bin". Finally, in the third candidate strategy, the upper-level controller estimates the difference between the optimal power output of the system and the output at the present altitude; this estimated difference, termed the surrogate power deficit, is used to adjust the perturbation amplitude for a mid-level LSES controller, and this hierarchical structure is termed globalized LSES (GLSES).

The hierarchical control structures for optimizing standalone and integrated AWE systems are shown in Figs. 1.10 and 1.11, respectively. These block diagrams also include a lower-level flight controller that regulates the altitude to its set-point, along with a turbine torque controller. The turbine torque controller is similar to the system described in [43], and the flight control system for the Altaeros BAT is discussed in [44]. Because these lower-level controllers have been validated through simulations and experiments in legacy work, they are not the focal point of this research.

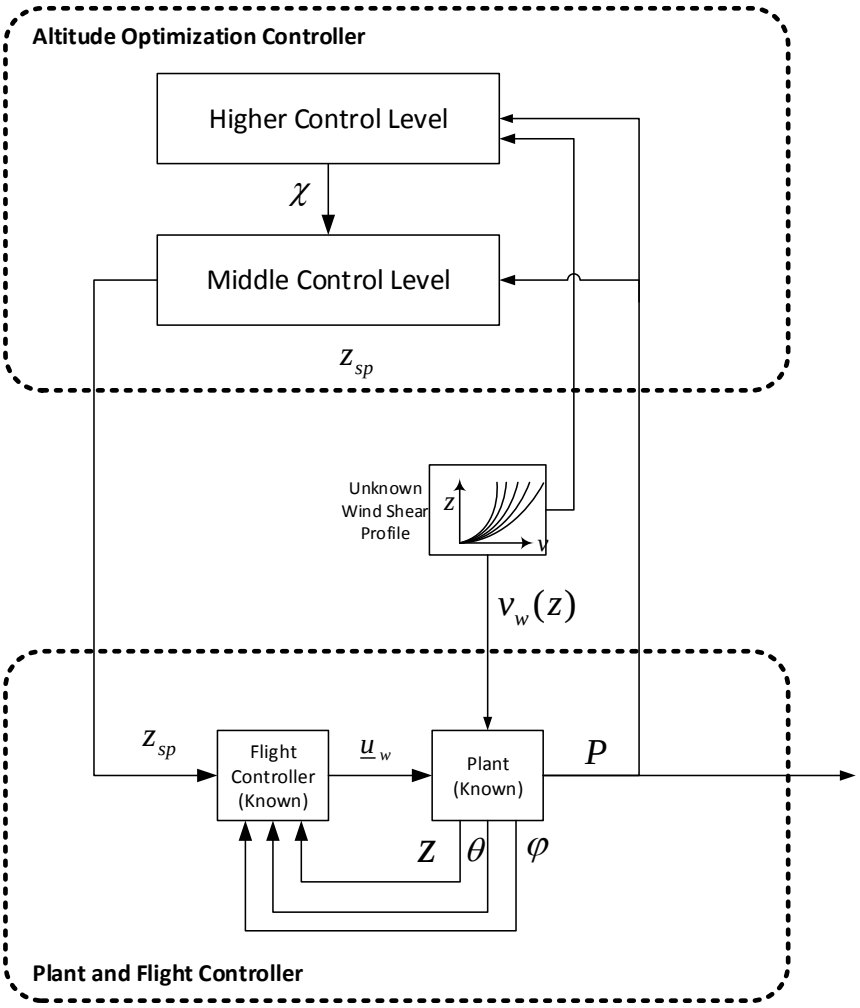

Figure 1.10: Basic block diagram showing the common proposed hierarchical altitude control structure for an AWE system.

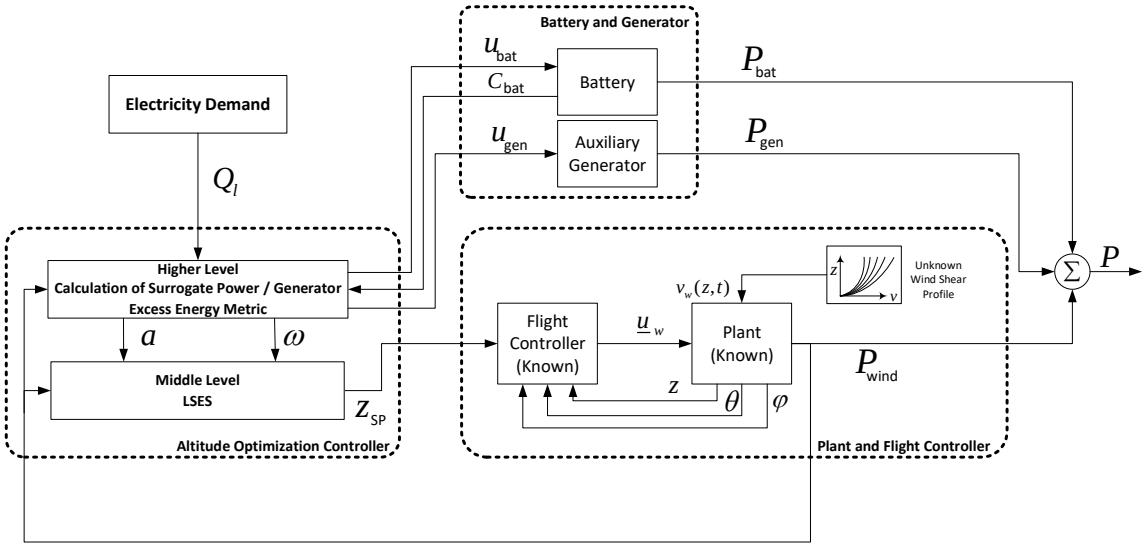

Figure 1.11: Basic block diagram of the GLSES controller for altitude optimization of an integrated AWE system ([8])

Table 1.2: Controller Choice for Each Level of Candidate Hierarchical Structures

Candidate Structure	Upper level	Mid-level
MPC – LSES	Coarse MPC	LSES
MPC – MPC	Coarse MPC	Fine MPC
GLSES	Calculation of LSES perturbation based on surrogate power deficit	LSES

1.7.2 Controller Choices for Different Levels of the Hierarchy

One of the most prevalent methods for optimization of unknown systems is extremum seeking (ES). ES is a (typically) non-model-based control scheme that is used to find the optimal operating point of an unknown system in real time [45]. Here, a modified ES control scheme is used, where the amplitude of the perturbation signal is diminished upon convergence to the optimal point. This controller, termed

Lyapunov-based switched ES (LSES), is discussed in Section 4.1. Another control tool for different levels of the hierarchical control structure is model predictive control (MPC), which is briefly described in Section 4.3.

One metric for evaluating the performance of the altitude controller is to calculate how much more energy could be produced by selecting other altitudes as the setpoint. This deficiency is termed the *power deficit*. However, finding the maximum available power at each time step requires omniscient knowledge of the wind velocity over all altitudes in the domain. In light of this, the power deficit is *estimated* by calculating a metric named *surrogate power deficit* which is detailed in Section 3.3.1.

The proposed hierarchical control structure, as shown in Figs. 1.10 and and 1.11 and described in Chapters 5 and 6, includes the following components:

1. *Model Predictive Control (MPC)*: One of the control choices for both the top and middle levels is model predictive control (MPC). The coarse MPC is capable of finding the global optimum in upper control level if a global optimization tool is used. The local, fine MPC is used for the mid-level controller. The statistical characterization of wind velocity used in MPC and the MPC controller are developed and included in Section 3.1 and Chapter 4, respectively.

2. *Lyapunov-Based Switched Extremum Seeking (LSES)*: Another candidate for the middle control level is LSES, which is a computationally fast but local controller. The use of LSES for altitude optimization of AWE systems is detailed in Chapter 4.

3. *Calculation of Surrogate Metric*: In the GLSES control scheme introduced in Section 1.7.1, a surrogate deficit metric, which estimates the amount by which the present operating condition falls short of the optimum, is calculated in the upper level. This metric is used to adjust the amplitude and frequency of the perturbation in the lower-level LSES. This surrogate metric is either an

estimate of the difference between the maximum possible and current power production (surrogate power deficit), or an estimate of the difference between the minimum possible and current generator energy excess (surrogate generator excess energy). These two surrogate metrics are detailed in Chapters 5 and 6.

4. *Flight Controller*: The lower-level flight controller regulates altitude to its set-point, along with a turbine torque controller. The turbine torque controller is similar to the system described in [43], and the flight control system for the Altaeros BAT is discussed in [44]. Because these lower-level controllers have been validated through simulations and experiments in legacy work, they are not the focal point of this research.

1.8 Wind Shear Profile and electricity Demand Data

In order to design and evaluate candidate controllers for the altitude optimization problem at hand, wind velocity and electricity demand data are required. In this research, we used the real wind and load data as described in Subsections 1.8.1 and 1.8.2, respectively.

1.8.1 Wind Shear Profile

The wind data set used in this research includes wind velocity at 30 minute time intervals, at 48 altitudes between 146 and 3000m, over the course of one year (2014). Considering the practical limitations of AWE system flight altitude, the portion of data involving altitudes up to $1km$ was considered for this research. Fig. 1.12 illustrates the variability and (common) non-monotonicity of the wind shear profile for four sample days, plotted at 3 hour intervals. This figure demonstrates the progres-

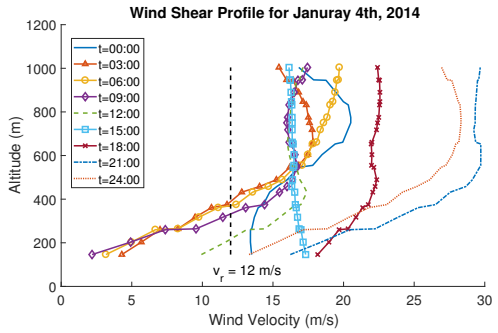

(a) Jan. 4 2014

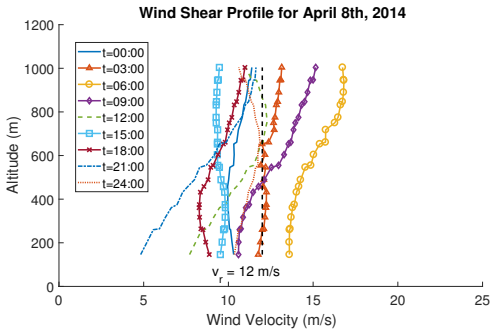

(b) Apr. 8 2014

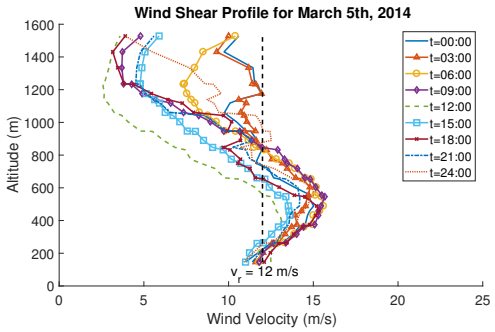

(c) Mar. 5 2014

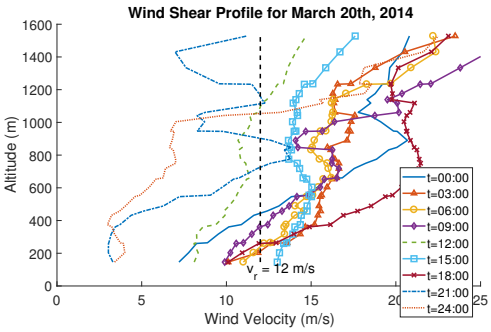

(d) Mar. 20 2014

Figure 1.12: Sample real wind shear profiles based on real data from a wind profiler in Cape Henlopen State Park, Lewes, Delaware. Selected dates: (a) January 4th, (b) Apr. 8th, (c) March 5th and (d) March 20th, 2014 at three hour intervals [7]. While in some cases the wind shear roughly conforms with the power law, (subplots(a) and (b)), there are many cases at which the wind shear profile can be non-monotonic (subplots(c) and (d)). Additionally, these plots clearly show that the wind shear profile exhibits significant temporal variability. Moreover, the optimal operating point corresponding to a rated wind velocity of $12\frac{m}{s}$ (which is assumed in this paper), varies noticeably.

sion of the wind shear profile over a 24 hour period, with instantaneous wind shear profiles plotted at each 3 hour interval. It can be inferred from this figure that the wind shear profile at any given time does not fit neatly into a power law or logarithmic approximation.

1.8.2 Electricity Demand Data

Real hourly electricity demand data for this study were obtained from the PJM Interconnection website [46]. This data is for the same geographical location as the

wind data. To emulate an AWE system configuration where the AWE system can supply a large fraction of the total energy demand, the research results presented here utilize a scaled load profile where the average electricity demand is two thirds of the AWE system's rated power.

1.9 List of Contributions

In this dissertation, candidate hierarchical structures are developed for altitude optimization of an integrated AWE system. Specifically, this research makes the following contributions:

1. A novel altitude optimization algorithm for an integrated AWE-battery-generator system is developed;

2. AN LSES controller is applied in isolation to the partial observable, spatiotemporally varying problem of AWE altitude optimization;

3. A mechanism is developed for globalizing an initially local LSES controller;

4. A probability-based surrogate power deficit metric is introduced for standalone AWE systems;

5. A probability-based surrogate generator energy excess metric is introduced for integrated AWE systems;

6. Candidate hierarchical optimization strategies are simulated and verified for a 100kW AWE system, using real wind and electricity demand data for 15 days.

1.9.1 Dissertation Outline

This dissertation is organized as follows: Chapter 2 details the deterministic modeling tools required for the proposed controllers. These models characterize the energy generation of an AWE system with integrated battery and generator. Statistical models are described in Chapter 3, including a conditional probability model for the wind speed and details of the surrogate power deficit and surrogate generator excess energy metrics. Chapter 4 introduces the candidate control tools for the upper and middle levels in the hierarchical structure. Then, Chapters 5 and 6 detail the hierarchical control structure for standalone and integrated AWE systems, respectively.

CHAPTER 2: Physical Modeling Tools

Because the focus of this dissertation lies in the optimal control of an integrated AWE-battery-generator system, it is important for both simulations and control to have adequate models of the AWE system (in terms of its power curve and control energy required to adjust/maintain altitude), as well as the battery dynamics and generator behavior.

2.1 The Energy Generation Model of an AWE system

An appropriately-designed altitude optimization should take into account not only the energy generated by the turbine, but also the energy consumed in both adjusting and maintaining the altitude of the AWE system. This results in an instantaneous power generation function that contains three elements and is given as follows [47]:

$$P_{\text{net}} = k_1 \min(v_{\text{w}}(z), v_{\text{r}})^3 - k_2 v_{\text{w}}^2 + P_z(v_{\text{w}}, \dot{z}), \tag{1}$$

where z is the operating altitude, $v_{\text{w}}(z)$ is the wind speed at the operating altitude, v_{r} is the turbine's rated wind speed, and P_z is the instantaneous power required for or regenerated by adjusting altitude. k_1 and k_2 are constant parameters that depend upon the turbine's power curve and flight control system (comprising both the controller and the aerodynamics of the lifting body), respectively. Generally, the power produced by a wind turbine can be modeled as:

$$P_{\text{tur}} = \frac{1}{2}\rho A v_{\text{w}}^3 C_P \tag{2}$$

in which ρ is the air density, A is the rotor area, and C_P is the power coefficient.

Accordingly, k_1 can be defined as:

$$k_1 = \frac{P_{tur}}{v_{\mathrm{w}}^3} = \frac{1}{2}\rho A C_P \tag{3}$$

In order to calculate k_2, it is important to consider that maintaining altitude requires the tethers to apply a total force that overcomes the lifting force on the BAT. The application of this force alone does not require energy - however, in the presence of turbulence (or any wind environment that is less than perfect), small adjustments are necessary to maintain altitude - the power required to make these adjustments is proportional to the tension in the tethers. The lifting force on the aerostat body is given by:

$$L = \frac{1}{2}\rho A_{ref} v_{\mathrm{w}}^2 C_L + F_b, \tag{4}$$

where L is the total lift force, A_{ref} is the reference area for the BAT, C_L is the lumped coefficient of lift, and F_b is the buoyant force. Under high wind conditions (under which the tether tensions are significant), F_b is much smaller than the aerodynamic lifting force, and the lifting force can be approximated by:

$$L = \frac{1}{2}\rho A_{ref} v_{\mathrm{w}}^2 C_L. \tag{5}$$

Since the power expenditure for maintaining altitude is proportional to this lifting force, that power expenditure, P_{maint}, can be expressed as:

$$P_{\mathrm{maint}} = \frac{1}{2}\rho A_{ref} v_{\mathrm{w}}^2 v_{ave} C_L, \tag{6}$$

where v_{ave} is the average tether release speed over typical operation. Accordingly, k_2 can be defined as:

$$k_2 = \frac{P_{maint}}{v_{\mathrm{w}}^2} = \frac{1}{2}\rho A_{ref} v_{ave} C_L. \tag{7}$$

The power required to adjust altitude, P_z, is given as follows:

$$P_z(v_{\mathrm{w}}, \dot{z}) \;=\; \begin{cases} \frac{k_3}{\eta_m} \dot{z} v_{\mathrm{w}}^2, & \dot{z} \leq 0 \\ k_3 \eta_g \dot{z} v_{\mathrm{w}}^2, & otherwise. \end{cases} \tag{8}$$

Here, η_m is the efficiency of the motors that drive the winches, η_g is the regenerative efficiency of the winches, and k_3 is a constant parameter that depends on the aerodynamics of the lifting body and its trim pitch angle. Because any upward altitude adjustment of the system must later be compensated with a downward altitude adjustment (the system must land eventually), and because it is not the explicit objective of a system with airborne energy generation to strategically leverage additional energy through regeneration on the ground, it is possible to simplify the objective function for the system, which should be maximized, as follows:

$$P = k_1 \min(v_{\mathrm{w}}(z), v_{\mathrm{r}})^3 - k_2 v_{\mathrm{w}}^2 - \bar{k}_3 v_{\mathrm{w}}^2 |\dot{z}|, \tag{9}$$

where $\bar{k}_3$ is a lumped parameter that is dependent on overall winch efficiency and aerodynamics of the lifting body.

2.2 Battery Model and Generator Energy Calculation

In this study, we use a simple difference equation to model the battery storage system. This is appropriate for high-level dynamic modeling of battery systems, as discussed in [48]. Specifically, the battery state of the charge at time step $k+1$, denoted by $C_{\mathbf{b}}(k+1)$, is equal to the previous state of charge of the battery plus the amount of additional energy stored in or discharged from the battery, considering charging and discharging efficiency of the storage system:

$$C_{\mathbf{b}}(k+1) = \begin{cases} C_{\mathbf{b}}(k) - \frac{1}{\eta_{bat}} E_{\mathbf{bat}}(k), & E_{\mathbf{bat}}(k) > 0 \\ C_{\mathbf{b}}(k) - \eta_{bat} E_{\mathbf{bat}}(k), & \text{otherwise.} \end{cases} \tag{10}$$

Here, $E_{\mathbf{bat}}(k)$ is the amount of energy discharged from the battery at step k, and η_{bat} is the efficiency of the battery during charging/discharging .

In our formulation, $E_{\mathbf{bat}}(k)$ is the amount of energy discharged from the battery to supply the balance of energy, termed the *deficit*, that is not provided by the wind turbine. This energy deficit, denoted by $E_{\mathbf{d}}(k)$, is given by:

$$E_{\mathbf{d}}(k) = (Q_l(k) - P_w(k))\,\Delta t \tag{11}$$

where Q_l and P_w are electricity demand and wind turbine power output, respectively. The energy supplied by the battery, which is limited by the state of charge of the storage system, is given by:

$$E_{\mathbf{bat}}(k) = \begin{cases} \eta_{bat} C_{\mathbf{b}}(k), & E_{\mathbf{d}}(k) > \eta_{bat} C_{\mathbf{b}}(k) \\ \frac{1}{\eta_{bat}}(C_{\mathbf{b}}(k) - C_{\mathbf{max}}), & E_{\mathbf{d}}(k) < \frac{1}{\eta_{bat}}(C_{\mathbf{b}}(k) - C_{\mathbf{max}}) \\ E_{\mathbf{d}}(k), & \text{otherwise} \end{cases} \tag{12}$$

Here, $C_{\mathbf{max}}$ is the maximum capacity of the battery.

In typical applications of integrated AWE system, fossil fuels are expensive, and it is therefore desirable to address the electricity demand through the AWE system and battery prior to resorting to the generator. Hence, the generator is considered as the last option for energy supply. The generator is responsible to supply the remainder of the electricity demand that is not supplied through either the wind turbine or the battery:

$$E_{\mathbf{gen}}(k) = \max\{0, E_{\mathbf{d}}(k) - E_{\mathbf{bat}}(k)\} \tag{13}$$

CHAPTER 3: Statistical Modeling Tools

In addition to modeling AWE power production, battery dynamics, and generator behavior, it is of great use to develop statistical models that characterize the stochastic properties of the wind shear and electricity demand profiles. It is also required to assess the performance of the candidate controllers in real-time as they operate in a partially observable environment. For this, we will describe in this chapter a surrogate power deficit metric and a surrogate generator excess metric. These metrics are used in the higher control level to evaluate how much better the mid-level controller can perform.

3.1 Statistical Characterization of Wind Shear Profile

In this section, a statistical model for wind shear profile, based on historical data, is described. The first subsection describes the spatiotemporal behavior of the wind. Next, the basics of statistical wind shear profile characterization are discussed, and finally, the appropriate mathematical structure for the modeling the conditional standard deviation of the statistical model is discussed.

3.1.1 Spatiotemporal Characterization of the Wind Shear Profile

Figure 3.1 shows the spatial variation of wind speed at 31 separate instances during January, 2014. All the measurements were taken at a specific time, t_0, during each day (which happened to be midnight). To illustrate the spatial variability of wind shear profiles taken at significantly different times (all at least 24 hours apart from each other), Figure 3.1 plots the *difference* between the wind speed at a particular

altitude, z, and the wind speed at a reference altitude, z_0 (which is taken as 546m in Figure 3.1), denoted by $\Delta v_{\mathrm{w,spatial}}(\Delta z, t_0, z_0)$:

$$\begin{aligned} \Delta v_{\mathrm{w,spatial}}(\Delta z, t_0, z_0) &= v_{v_{\mathrm{w}}}(t_0, z_0 + \Delta z) \\ &\quad - v_{\mathrm{w}}(t_0, z_0) \end{aligned} \tag{1}$$

$\Delta v_{\mathrm{w,spatial}}(\Delta z, t_0, z_0)$ increases with increasing Δz. From an altitude optimization perspective, this implies, unsurprisingly, that one's ability to predict wind speed at a particular altitude depends on the proximity of that altitude to ones where data has already been gathered.

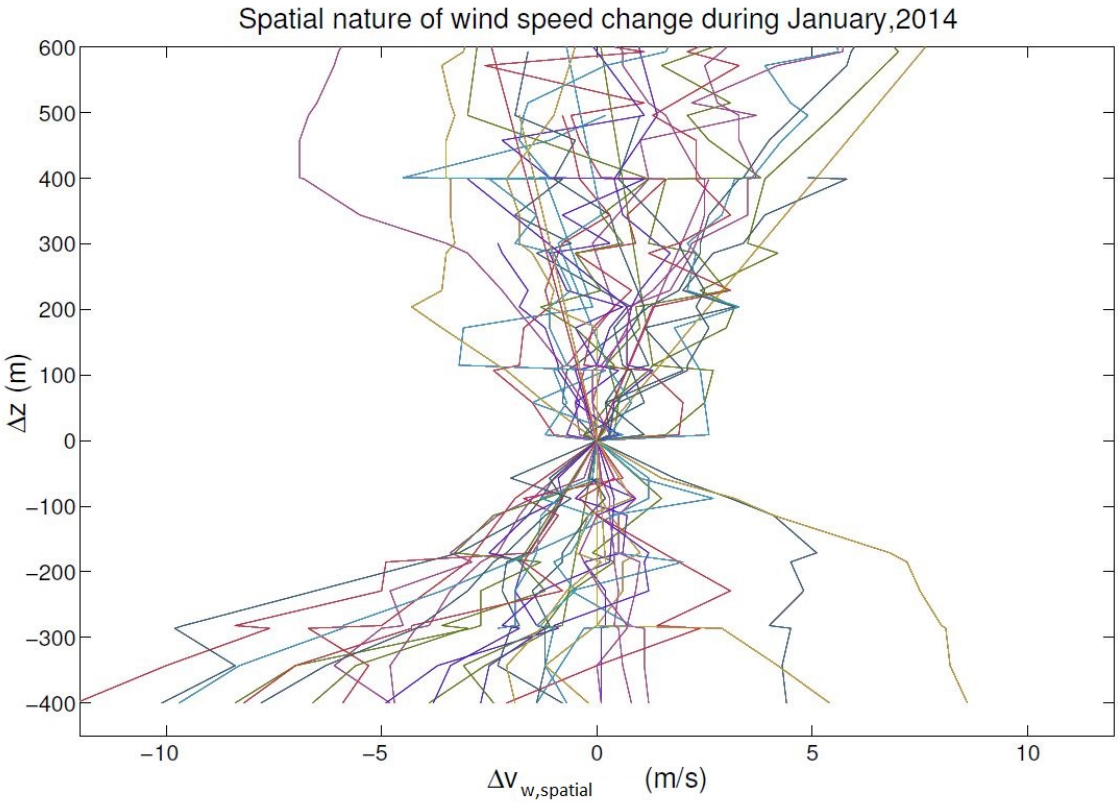

Figure 3.1: Spatial variation in wind speed, with respect to wind speed at a base altitude (z_0) of 546m (at 00.00 hour, i.e., midnight), for 31 days during the month of January, 2014 [9].

Figure 3.2 shows the temporal nature of wind speed over the 31 days in January, 2014, at a constant altitude $z_0 = 146m$. As with Figure 3.1, Figure 3.2 plots the *difference* in wind speed between time t and a reference time t_0, denoted by $\Delta v_{\mathrm{w,temporal}}(\Delta t, t_0, z_0)$:

$$\begin{aligned} \Delta v_{\mathrm{w,temporal}}(\Delta t, t_0, z_0) &= v_{\mathrm{w}}(t_0 + \Delta t, z_0) \\ &\quad - v_{\mathrm{w}}(t_0, z_0). \end{aligned} \tag{2}$$

Figure 3.2 shows that, given a measurement of wind speed at time t_0, the proximity of wind speed to $v_{\mathrm{w}}(t_0, z_0)$ diminishes with increasing time. From an altitude optimization perspective, Figures 3.1 and 3.2 show that in order to maintain accurate knowledge of the wind shear profile, it is necessary to continually *explore* different altitudes; otherwise, the uncertainty in wind speed grows to be very large. Large-scale analysis of the data from Cape Henlopen can be (and was) used to quantify the statistical variability of wind speed with respect to time and altitude, thereby providing the appropriate mathematical mechanism for encouraging exploration, which is detailed in Section 3.1.

3.1.2 Statistical Wind Shear Profile Characterization

For spatiotemporal optimizations where the random variable is partially observable in space (such as the altitude optimization problem, where wind speed is partially observable in altitude at which AWE system is flying), an appropriate balance between *exploitation* and *exploration* must be achieved. *Exploitation* involves making the best decision given the current information. *Exploration*, on the other hand, involves information gathering. In the case of AWE systems, exploitation involves using past and present wind data to determine and go to the optimal altitude for maximum energy generation. However, if the AWE system sits at a fixed altitude for a long

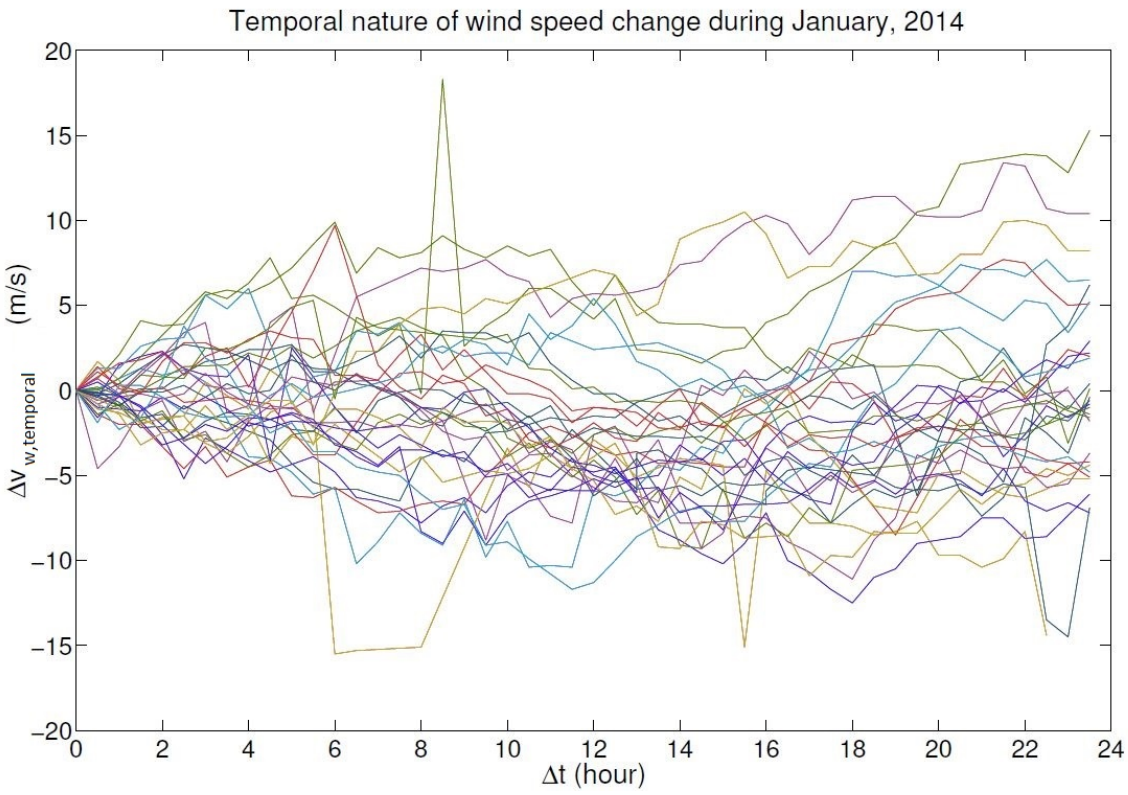

Figure 3.2: Temporal variation of wind speed, with respect to base data taken at time t_0, at an altitude of 146m, for 31 days during the month of January, 2014 [9].

time, the knowledge of the wind velocity at altitudes it visited earlier becomes less effective, as earlier wind velocity measurements could be very different from the wind velocities at the present instant (see Figure 3.2).

To quantify the need for exploration, the statistical characteristics of the wind shear profile are very important. Instantaneous wind velocity has traditionally been characterized by 2-parameter Weibull distributions [49], 1-parameter Rayleigh distributions [50], and 2-parameter log normal (LN2) distributions [51], all of which yield reasonable statistical characterizations. In this work, we consider a 2-parameter log normal (LN2) distribution, whose probability density function (PDF) and cumulative density function (CDF) are:

$$f(x;\mu,\sigma) = \frac{1}{x\sigma\sqrt{2\pi}} \exp\left[-\frac{(\ln x - \mu)^2}{2\sigma^2}\right], x > 0 \tag{3}$$

and

$$F(x;\mu,\sigma) = \frac{1}{2} + \frac{1}{2}\mathrm{erf}\left[\frac{\ln x - \mu}{\sigma\sqrt{2}}\right] \tag{4}$$

respectively. Here, x is the random variable, and the parameters μ and σ are the mean and standard deviation of $ln(x)$. $erf()$ is the error function from the normal distribution.

In the AWE application, x is taken as the *ratio* of the wind velocity (v_w) to a reference wind velocity, v_0:

$$x = \frac{v_\mathrm{w}}{v_0}. \tag{5}$$

In striking the appropriate balance between exploration and exploitation, we are interested in understanding the value of new data in terms of predicting wind speed. As such, we are interested in the *conditional statistical* characteristics of wind speed, *conditioned upon past and present measurements.* These can be characterized through a conditional mean and conditional standard deviation, denoted by:

$$\mu^c \triangleq \mu(ln(x(t,z))|\mathbf{D}) \tag{6}$$

and

$$\sigma^c \triangleq \sigma(ln(x(t,z))|\mathbf{D}), \tag{7}$$

respectively, where $\mathbf{D}$ represents a matrix of m previously-measured wind speeds and corresponding measurement points. $\mathbf{D}$ is specified by:

$$\mathbf{D} = \begin{bmatrix} t_0 & \dots & t_{m-1} \\ z_0 & \dots & z_{m-1} \\ v_\mathrm{w}(t_0,z_0) & \dots & v_\mathrm{w}(t_{m-1},z_{m-1}) \end{bmatrix}. \tag{8}$$

To precisely characterize the aforementioned conditional statistics, $\mathbf{D}$ should include *all* previously-acquired data points; however, for practical purposes, considering a finite set m of recent points is sufficient to accurately approximate the quantities, as distant past measurements provide little predictive value.

Available wind shear data was used to characterize the conditional distributions in (6) and (7). Figure 3.3 provides the conditional standard deviation, σ^c, *conditioned upon a single data point*, $\mathbf{D} = [\ t_0 \quad z_0 \quad v_{\mathrm{w}}(t_0, z_0)\ ]^T$. The trends in the figure represent earlier qualitative observations that the predictability of wind speed diminishes as time and altitude are taken farther away from previously-measured data points. However, the data-based analysis presented in Figure 3.3 provides a quantification of this phenomenon, which will be incorporated into the subsequent MPC-based altitude optimization.

To describe the aforementioned conditional mean and standard deviation in a way that is usable for the subsequent EMPC-based optimization, estimates of these quantities, denoted by $\hat{\mu}^c$ and $\hat{\sigma}^c$, are parameterized as follows:

$$\mu^c \triangleq \mu(ln(x(t,z))|\mathbf{D}) \tag{9}$$

$$\hat{\sigma}^c(ln(x(t,z))|\mathbf{D}) = m_0 \prod_{i=0}^{n-1}(1 - e^{-m_1 \Delta t_i} e^{-m2\Delta z_i}). \tag{10}$$

Here i is the altitude bin number, $t(i)$ is the time of latest wind speed measurement at altitude $z(i)$, and Δt_i and Δz_i represent the time that has passed since measurement i and the difference in altitude between the present altitude and z_i, respectively, i.e.:

$$\Delta t_i = t - t_i, \tag{11}$$

$$\Delta z_i = |z - z_i|. \tag{12}$$

While heuristic, the approximations of $\hat{\mu}^c$ and $\hat{\sigma}^c$ in (9) and (10) capture important

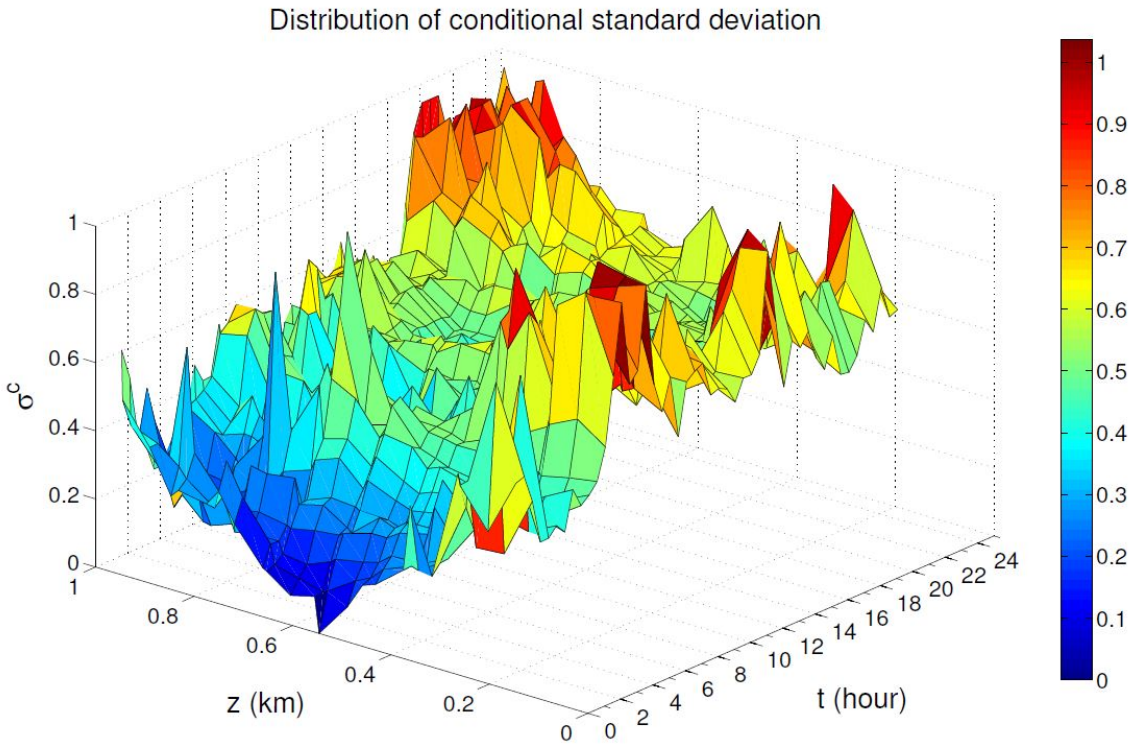

Figure 3.3: Spatial and temporal distribution of conditional standard deviation $\sigma(ln(x(t,z))|v_{\mathrm{w}}(t_0,z_0))$, conditioned upon a single measurement of wind speed $v_w(t_0,z_0)$, at time t_0 (00.00 hour), altitude z_0 (546m) [9].

properties that are observed in practice and in the plot of Figure 3.3, namely:

- The conditional mean of wind velocity at each altitude bin is equal to the latest observation at that altitude (i.e., it is assumed that the most recently observed wind will persist in the future);
- The conditional standard deviation increases with variation in time and altitude, and asymptotes to a maximum value (m_0), which is observed in the data;
- Availability of additional data points results in reduced conditional standard deviation, reflecting an increase in prediction certainty with more data.

Available wind shear data was used to identify the values of m_0, m_1, and m_2 in (9) and (10) that minimize the squared error between actual and estimated conditional

mean and standard deviation. Figure 3.4 provides the graphical representation of (9) and (10), conditioned upon the same single measurement point as in Figure 3.3.

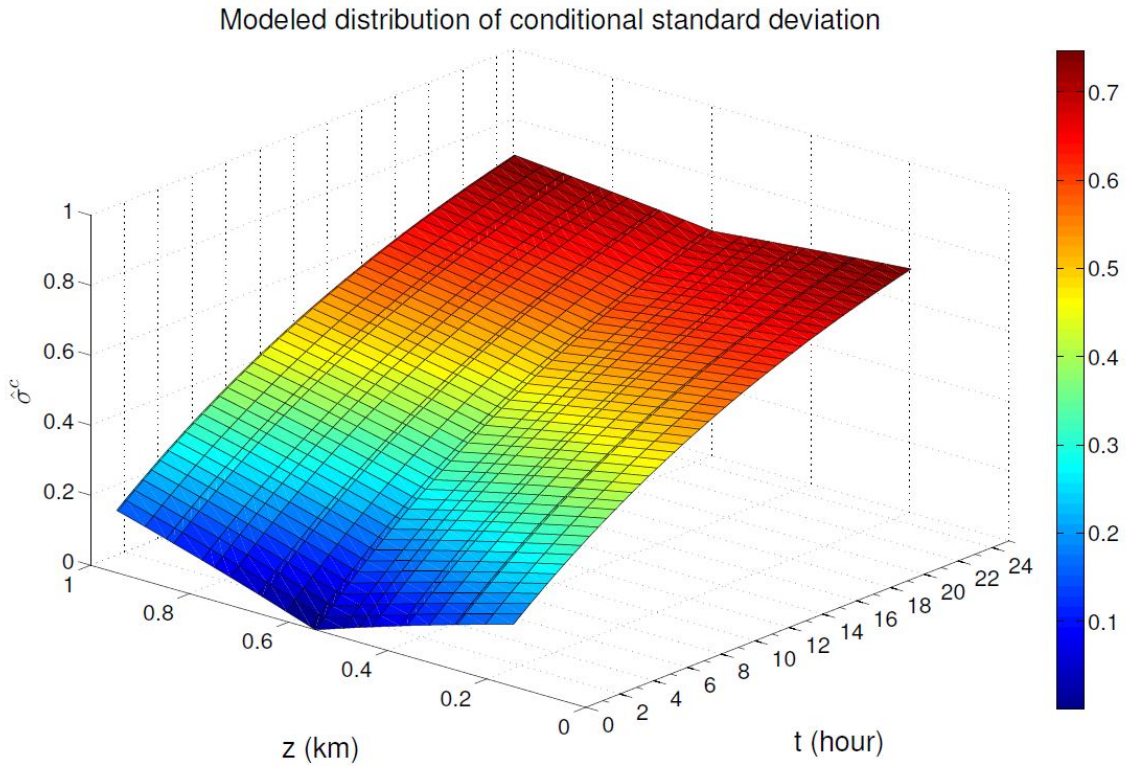

Figure 3.4: Modeled spatial and temporal distribution of conditional standard deviation $\hat{\sigma}^c(ln(x(t,z))|v_{\mathrm{w}}(t_0,z_0))$, conditioned upon a single measurement of wind speed $v_w(t_0,z_0)$ at time t_0 (00.00 hour), altitude z_0 (546m). [9]

3.1.3 Calculation of Expected Power as a Function of Expected Wind Velocity

Reference [52] suggests the use of a Taylor expansion to find the moments of a function P of a random variable x, provided that P is sufficiently differentiable and that the moments of x are finite:

$$E[P(x)] \approx P(\mu_x) + \frac{P''(\mu_x)}{2}\sigma_x^2 \tag{13}$$

$$var[P(x)] \approx (P'(\mu_x))^2\sigma_x^2 \tag{14}$$

where μ_x and σ_x are mean and standard deviation of $ln(x)$, respectively, and $x = \frac{v}{v_0}$.

The power generation function, as introduced in (9), is not differentiable at v_{r}. To overcome this problem, we approximate the power function at v_{r} with a quadratic function, and the first and second derivatives of $P(v)$ with respect to the random variable x at the rated wind speed are approximated as:

$$P'(v_{\mathrm{r}}) \approx 2av_{\mathrm{r}} + b \tag{15}$$

$$P''(v_{\mathrm{r}}) \approx 2a \tag{16}$$

where $x_r = \frac{v_r}{v_0}$, and a and b are the coefficients of the quadratic fit to P at v_r.

Consequently, the mean and standard deviation of available power in the i^{th} altitude bin are:

$$E[P_i(x)] = \begin{cases} (k_1(v_0\hat{\mu}_i)^3 - (k_2 + k_3|\dot{z}|)(v_0\hat{\mu}_i)^2) + (3k_1v_0^3\hat{\mu}_i - (k_2 + k_3|\dot{z}|))\, v_0^2\hat{\sigma}_i^2 & v < v_{\mathrm{r}} \\ (k_1v_{\mathrm{r}}^3 - (k_2 + k_3|\dot{z}|)(v_0\hat{\mu}_i)^2) - \quad (k_2 + k_3|\dot{z}|)\, v_0^2\hat{\sigma}_i^2 & v > v_{\mathrm{r}} \\ k_1v_r^3 - (k_2 + k_3|\dot{z}|)(v_{\mathrm{r}})^2 + a\hat{\sigma}_i^2 & v = v_{\mathrm{r}} \end{cases} \tag{17}$$

$$var[P_i(x)] = \begin{cases} (3k_1v_0\hat{\mu}_i^2 - 2(k_2 + k_3|\dot{z}|)\hat{\mu}_i)^2\, v_0^2\hat{\sigma}_i^2 & v < v_r \\ (2(k_2 + k_3|\dot{z}|)\hat{\mu}_i)^2\, v_0^2\hat{\sigma}_i^2 & v > v_r \\ (2av_r + b)^2\hat{\sigma}_i^2 & v = v_r \end{cases} \tag{18}$$

3.2 Load Forecasting

Short-term load forecasting has been extensively addressed in the literature [53]. Within the available load forecasting techniques proposed in the literature, this dissertation works with a combined forecast based on three forecasting techniques: (1) multiple linear regression (MLR), (2) autoregressive integrated moving average (ARIMA) model, and (3) k-nearest neighbors (KNN) techniques. In other words, we fuse one set of forecasts based on regression, one set of forecasts based on time-series analysis, and one set of forecasts based on a machine learning technique, which is the K nearest neighbors. Then, using the electricity demand data for years 2007 to 2012 as the training data, we forecast the load for the year 2013 using each of the individual forecasting techniques. Finally, we use a sequential quadratic programming (SQP) algorithm to assign weights to each individual forecast in the combined model. These forecasting techniques are briefly described in the following subsections. The electricity demand data are obtained from PJM [46], as described in Subsection 1.8.2.

3.2.1 Multiple Linear Regression

Multiple linear regression (MLR) forecasting has been extensively used for short-term load forecasting. In this technique, load forecast is calculated using explanatory variables such as weather and non-weather variables, which influence the electrical load [54]. For this purpose, [55] introduced Tao's Vanilla benchmark model:

$$\hat{y}_t = \beta_0 + \beta_1^{1\times 11} M_t^{11\times 1} + \beta_2^{1\times 6} D_t^{6\times 1} + \beta_3^{1\times 23} H_t^{23\times 1} + \beta_4^{1\times 138} D_t H_t^{138\times 1} + f_1(T_t)^{105\times 1} \quad (19)$$

where β is the vector of coefficients, $M_t^{11\times 1}$, $D_t^{6\times 1}$, and $H_t^{23\times 1}$ are normalized month of the year, day of the week, and hour of the day classification variables corresponding

to the same hour t, respectively. T_t is the temperature at time t. We normalized the variables before using them in the linear regression forecasting model.

In the model of (19), it is important to distinguish between quantitative and classification variables. Quantitative variables, like temperature, represent a quantity, while classification variables are used for categorizing the observations. For example, the day of the week variable here, categorizes the observations into 7 categories. In fact, we just need to add 6 elements to the regressor vector representing each day. Then, we check for each observation if it occurs in Sunday or not (0 or 1), in Monday or not (0 or 1) and so on, and if all 6 elements are 0, it means that the Day is Saturday. Therefore, Sunday and Saturday correspond to $[1 \quad 0 \quad 0 \quad 0 \quad 0 \quad 0 \quad]^T$ and $[0 \quad 0 \quad 0 \quad 0 \quad 0 \quad 0 \quad]^T$, respectively. Hence, β_2 and D_t have 6 elements. Similarly, the size of a month of the year and hour of the day are 11 and 23, respectively.

$f_1(t)$ is a nonlinear function of T and interaction between temperature and classification variables:

$$f_1(T_t) = \beta_5 T_t + \beta_6 T_t^2 + \beta_7 T_t^3 + \beta_8 T_t M_t + \beta_9 T_t^2 M_t + \beta_{10} T_t^3 M_t + \beta_{11} T_t H_t + \beta_{12} T_t^2 H_t + \beta_{13} T_t^3 H_t \quad (20)$$

Therefore, the regressor vector to forecast the electricity demand using the Tao's Vanilla benchmark model has 284 elements.

Typically, the electric electricity demand at the current hour is affected by the weather conditions in the recent preceding hours. Accordingly, [55] proposed to account for the *recency* effect by adding lagged temperature to the formulation above. Specifically, this work introduced two sets of lag variables namely lagged temperature variables ($\sum_g f_1(T_{t-g})$, $g = 0, 1, 2, 3, ...$) and lagged daily moving average temperature variables ($\sum_d f_1(\tilde{T}_{t,d})$, $d = 0, 1, 2, 3, ...$). $\tilde{T}_{t,d}$ is the daily moving average temperature

of the dth day:

$$\tilde{T}_{t,d} = \frac{1}{24} \sum_{i=24d-23}^{24d} T_{t-i} \tag{21}$$

Finally, the family of sister forecasting models based on the recency effect are built by varying g and d:

$$\hat{y}_t = \beta_0 + \beta_1 M_t + \beta_2 D_t + \beta_3 H_t + \beta_4 D_t H_t + f_1(T_t) + \sum_g f_1(T_{t-g}) + \sum_d f_1(\tilde{T}_{t,d}) \tag{22}$$

For the purpose of this research , we compared 9 MLR sister models by varying g and d from 0 to 2, termed LinReg00, LinReg01, etc. where the first and second numbers indicate g and d, respectively.

3.2.2 K Nearest Neighbors

K nearest neighbors (KNN) is a non-parametric method which is used in the machine learning community. The main idea is to find one or more similar points in the feature space to classify the desired point according to these nearest neighbors. In this paper, the feature space consists of the elements of the Tao's Vanilla benchmark introduced in 3.2.1. Specifically, we use the norm of the regressor vector $\tilde{y}$, which is defined similarly to (19):

$$\tilde{y}_t = [1; M_t^{11\times 1}; D_t^{6\times 1}; H_t^{23\times 1}; D_t H_t^{138\times 1}; f_1(T_t)^{105\times 1}] \tag{23}$$

In this work, it is assumed that the load forecast at a given point in the feature space is the simple average of the k nearest neighbors:

$$\hat{Q}_{l,kNN} = \frac{1}{k}\sum_{i=1}^{k}\hat{Q}_{l,i} \tag{24}$$

Here, $\hat{Q}_{l,kNN}$ is the load forecast based on the KNN method and $\hat{Q}_{l,i}$ is ith nearest neighbor of the desired point. We use $k = 2$ and $k = 8$ nearest neighbors, denoted as 2NN and 8NN, respectively, as the members of the sister forecasts of this family. These two sisters are selected based on the evaluation of error for the individual forecasts for $k = 1$ to 10.

3.2.3 Autoregressive Integrated Moving Average Model

Time series approaches to load forecasting have been widely studied in the literature. The ARIMA model as a time-series technique uses load's lag value to reflect the variation of electricity demand. This model is comprised of two parts: autoregressive AR and moving average MA models. In the autoregressive model, $AR(p)$, the current value of the process is expressed as a linear combination of p previous values of the process and an error term. In the moving average model, $MA(q)$, the current value of the process is expressed as a linear combination of previous error terms. Non-stationary processes can be modeled by differencing the original process to obtain a stationary time-series, which is called autoregressive integrated moving average. Also, it is advantageous to use a seasonal ARIMA model for load forecasting due to the periodic nature of the load [56]. Here, we use two ARIMA models, which have the same values for AR lag of $p = 7$, MA lag of $q = 6$, and integrator lag of 1 and vary in the seasonality ($s = 6$ and $s = 10$), denoted as ARIMA6 and ARIMA10.

3.2.4 Combined Load Forecast

The combined load forecast model used in this paper consists of 9 linear regression models, two KNN models, and two ARIMA models, as described above. Ultimately, the load forecast $\hat{Q}$ is the weighted average of the 13 individual forecasts:

$$\hat{Q}_l = \sum_{i=1}^{n_f} w_i \hat{Q}_{l,i} \tag{25}$$

where $\hat{Q}_l$ is the load forecast, n_f is the number of individual forecasts (here 13), w_i is the weight of ith forecast in the model, and $\hat{Q}_{l,i}$ is the ith individual forecast which is selected from 13 individual forecasts of LinReg00 to LinReg22, ARIMA6 and ARIMA10, 2NN and 8NN. Since we ultimately use this combined load forecast model in the upper level controller to estimate the surrogate generator excess energy over a horizon length, we modified the combined model by varying the weights of each individual forecast over the horizon:

$$\hat{Q}_l(k+j|k) = \sum_{i=1}^{n_f} w_{i,j} \hat{Q}_i(k+j|k) \tag{26}$$

Here, $Q_l(k+j|k)$ is the load forecast for j step ahead calculated at the kth time-step, and $w_{i,j}$ is the weight of ith individual forecast in the jth time-step.

In order to find the optimum set of weights for this paper, we calculated all 13 individual forecast over a 4 time-step horizon for 8760 hours of year 2013 based on the real load data of 2007 to 2012, as described in 1.8.2. Then we formulated the following optimization problem to find the optimum weights:

$$\begin{aligned} \underset{\underline{w}}{\text{minimize}} \quad & \text{MAPE} = \frac{1}{n} \sum_{i=1}^{n} \left(\frac{|Q_{l,i} - \hat{Q}_{l,i}|}{Q_{l,i}} \right) \\ \text{subject to} \quad & \sum_{i=1}^{13} w_{i,j} = 1, \ j = 1, 2, ..., 4 \\ & 0 \preceq \underline{w} \preceq 1. \end{aligned} \tag{27}$$

where MAPE is the mean absolute percentage error, and $Q_{l,i}$ and $\hat{Q}_{l,i}$ are the actual and foretasted electricity demand at step i, and n is the size of training data. The optimization problem at hand has a nonlinear cost function and linear constraints. Therefore, the optimum set of weights for individual forecasts in the combined forecast

Table 3.1: Comparison of MAPE for Combined and 13 individual Forecast Models

Forecasting Model	MAPE
ARIMA10	0.0855
ARIMA6	0.0556
LinReg00	0.0810
LinReg01	0.0731
LinReg02	0.0710
LinReg10	0.0787
LinReg11	0.0718
LinReg12	0.0707
LinReg20	0.0745
LinReg21	0.0697
LinReg22	0.0710
2NN	0.0707
8NN	0.0602
Combined Model	0.0419

model is obtained using sequential quadratic programming (SQP).

Table 3.1 compares the MAPE of the candidate forecast models and the combined forecast model. This comparison is done by forecasting the electricity demand in 2013 using training data from 2007 to 2012. This table clearly shows that the combined model is more accurate than each of the individual forecasts.

3.3 Real-Time Performance Assessment via Surrogate Power Deficit and Generator Excess Metrics

In this section, surrogate power deficit and generator excess metrics are developed to assess in real-time the performance of standalone and integrated AWE systems, respectively.

3.3.1 Surrogate Power Deficit Metric

In optimizing altitude, our goal is to operate the AWE system at an altitude where the net power generation is maximized. As such, we wish to minimize the difference between the power output of the system at the altitude set-point and the maximum available power over all allowable altitudes. We term this quantity the *power deficit*. However, calculating the power deficit requires knowledge of the wind velocity over all allowable altitudes. Because wind speed is only measurable at the system's operating altitude, this information is not available. To address this issue of partial observability, we propose a surrogate metric that correlates closely with the power deficit but does not require the omniscient knowledge.

To derive a surrogate power deficit metric that can be computed under partial observability, we quantize the domain of allowable altitudes into finite number of "bins", then use the conditional probability model of available power at different altitude bins to estimate the power deficit. To do so, we derive a 95% confidence interval band for power output for each altitude bin. Then, we calculate the portion of this interval that exceeds the power production at the current altitude. Finally, we sum these portions over all altitude bins. The confidence interval is parameterized as follows:

$$I_{\mathbf{lb}}(i) = \max\left(0, E[P_i] - 1.96 * \sigma_i\right) \tag{28}$$

$$I_{\mathbf{ub}}(i) = \min\left(P_r, E[P_i] + 1.96 * \sigma_i\right) \tag{29}$$

$$CF_i = [L_i, H_i] \tag{30}$$

where $I_{\mathbf{lb}}$ and $I_{\mathbf{ub}}$ are the boundaries of the confidence interval of the i^{th} altitude bin, CF_i is the 95% confidence band, and $E[P_i]$ and σ_i are conditional probability characteristics of the available power at altitude bin i.

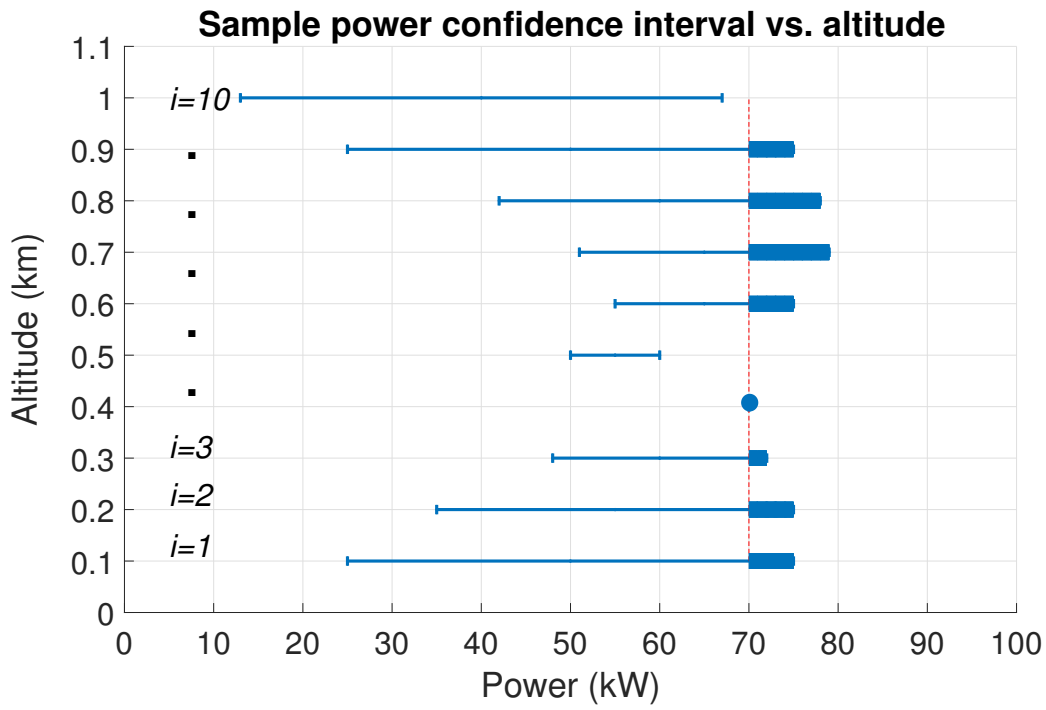

Figure 3.5: Sample visualization of 95% confidence intervals for available power at different altitude bins. Here, it is assumed that the AWE system is flying in bin no. 4. The portions of the confidence band beyond 70 kW (which are bold) are used in computing P_{sur}.

The surrogate power deficit P_{sur} is calculated using the formula:

$$P_{\text{sur}} = \sum_{i=1}^{n} \max\left((I_{\mathbf{ub}}(i) - P_{\text{cur}}), 0\right). \tag{31}$$

Here n is the number of bins, $I_{\mathbf{ub}}(i)$ is the upper bound for confidence interval in the i^{th} altitude bin, and P_{cur} is the current power output of the system. Fig. 3.5 illustrates how we calculate this surrogate metric.

To evaluate the correlation between this surrogate power deficit and the actual power deficit, the actual and surrogate power deficits are plotted in Fig. 3.6 over a period of one day. The actual power deficit P_{act} is the difference between the maximum available power at the given time in the available altitude domain:

$$P_{\text{act}} = \max(P_i) - P(z), i = 1, ..., n \tag{32}$$

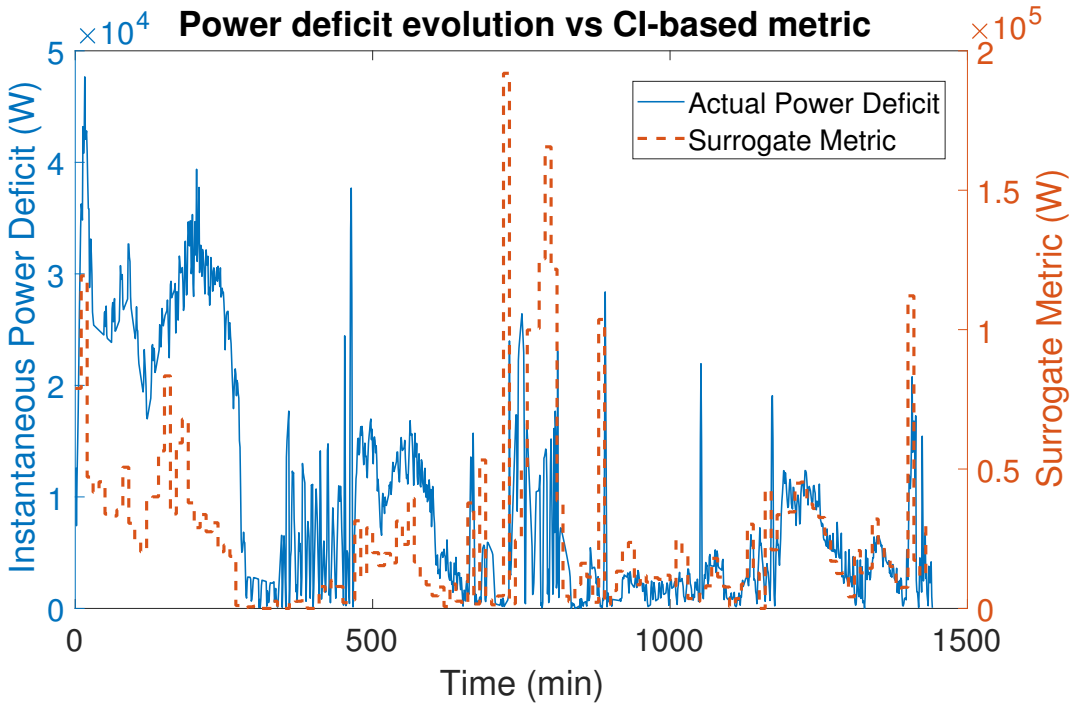

Figure 3.6: Actual vs. surrogate power deficit over a 24 hour simulation.

where P_i is the available power at altitude bin n.

Fig. 3.6 shows that the surrogate power deficit follows the changes in actual power deficit closely. Because the surrogate power deficit is summed over all altitude bins in equation (31), its raw magnitude will depend linearly on the number of bins used for the computation. In this case, where 10 bins are used, the P_{sur} is approximately one order of magnitude larger than P_{act}. It is important to note, however, that it is not the *magnitude* of the surrogate power deficit that is important but rather its *correlation* with the actual power deficit.

The surrogate metric defined here is similar to the idea of the upper confidence bound (UCB) used in machine learning. Both algorithms are based on the principle of optimism in the presence of uncertainty. In UCB algorithm, the next action is are chosen assuming that the environment is as nice as possible. The surrogate metric is also considers the same condition. However, the difference between the two algorithm lies in the decision that is made after bound is calculated. The UCB algorithm will go

to the spatial location with the highest upper confidence bound. In essence, the UCB algorithm is optimistic in the face of uncertainty; it assumes that the best possible outcome will arise from its actions, recognizing that even if the result is not as good as the optimistic prediction, at least the uncertainty will go down. The problem with using such a strategy in the case of altitude optimization is that one pays a significant price in terms of energy expenditure and lost opportunity in pursuing such a strategy. To address this issue, the algorithms described herein merely use the derived bounds to guide either the perturbation size in ES or the cost function in MPC.

3.3.2 Surrogate Generator Excess Metric

In an integrated AWE-battery-generator system, it is desirable to minimize the energy that is required from the auxiliary generator rather than just maximizing the net power production. While this difference may initially appear to be subtle, focusing on generator energy expenditure enables exploration during times of low electricity demand, benefiting the system at future time instances (due to increased certainty regarding the wind shear profile). Therefore, in place of the surrogate power deficit metric introduced in Section 3.3.1, a new metric is developed in this chapter to evaluate the performance of the mid-level controller. This metric, termed surrogate generator excess energy $M_{\mathbf{sur}}$, is based on the calculation of energy required from the auxiliary generator.

In order to determine $M_{\mathbf{sur}}$, we need to calculate $\tilde{E}_{\mathbf{gen}}$, which is a vector of the difference between energy expenditure of the auxiliary generator and the minimum energy that *could be* expended by the generator by operating at the optimum altitude $\hat{E}_{\mathbf{gen}}(i, k+j|k)$:

$$\tilde{E}_{\mathbf{gen}}(i,k+j|k) = \hat{E}_{\mathbf{gen}}(i,k+j|k)(i) - \min(C_{\mathbf{max}} - C_{\mathbf{bat}}(k+j|k), P_w(k+j|k)\Delta t) \quad (33)$$

where $\hat{E}_{\mathbf{gen}}(i,k+j|k)$ is the energy expended by the auxiliary generator, calculated at current time-step k, under the condition that the AWE system is flying in altitude bin i at time step $k+j$.

Then the new confidence intervals are calculated as:

$$I_{\mathbf{lb}}(i,k+j|k) = E_{\text{sur}}(i,k+j|k) - 1.96\sigma(i) \quad (34)$$

$$I_{\mathbf{ub}}(i,k+j|k) = E_{\text{sur}}(i,k+j|k) + 1.96\sigma(i) \quad (35)$$

where $I_{\mathbf{lb}}(i,k+j|k)$ and $I_{\mathbf{lb}}(i,k+j|k)$ are the upper and lower confidence interval bounds for the surrogate metric for the time-step $k+j$, calculated at current time-step k. In order to calculate $\hat{E}_{\mathbf{gen}}(i,k+j|k)$, it is required to forecast energy production and electricity demand over the horizon. Here, we assume that the operating altitude of the AWE system is constant over the horizon, and electricity demand is changing. Therefore, the statistical properties of the wind velocity are calculated for the same altitude bin. Consequently, the mean value of the wind velocity will be constant because new measurements over the future horizon are not yet known. On the other hand, the uncertainty increases for all altitudes in domain other than the current altitude as j increases, because the time passed from the latest measurement at those altitudes increases. The load forecast, denoted as $\hat{Q}_l$, is used in calculation of expected energy expenditure of the generator as detailed in (11).

The surrogate metric, $M_{\mathbf{sur}}$, is sum of the portions of these confidence intervals

that are less than the current energy output of the generator $E_{\mathbf{gen}}$:

$$M_{\mathbf{sur}} = \sum_{j=1}^{N} \sum_{i=1}^{n} \max(0, E_{\mathbf{gen}} - I_{\mathbf{lb}}(i, k+j|k)) \tag{36}$$

where N is the number of time-steps in the horizon.

This process is illustrated in Fig. 3.7, where the upper and lower plots demonstrate the calculation procedures of the surrogate power deficit and surrogate generator excess energy metric, respectively.

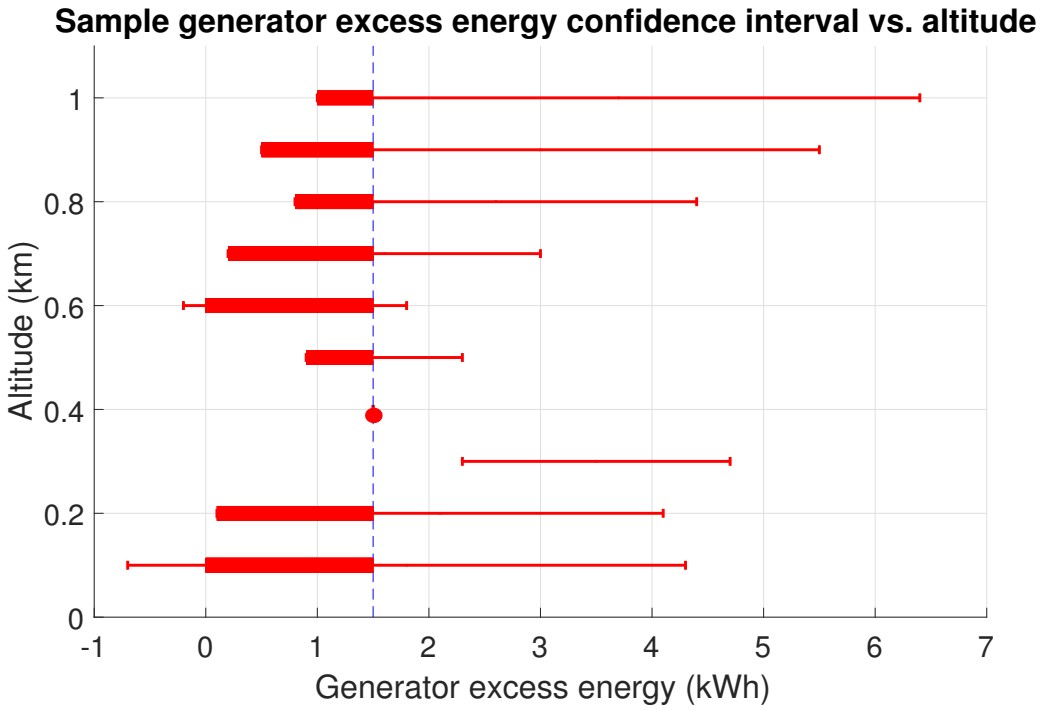

Figure 3.7: Sample visualization of 95% confidence intervals for generator excess energy for a single time step. Here, it is assumed that the AWE system is flying in bin no. 4.

One key difference between the two surrogate metrics lies in the fact that the surrogate power metric is only calculated for one step ahead, while effective implementation of surrogate generator excess energy metric requires this metric to be calculated over a receding horizon. The necessity of the receding horizon calculation arises mainly because the one step calculation does not incentivize exploration when the wind and

battery resources alone can address the full electricity demand.

Calculation of generator energy over a receding horizon requires a forecast of the electricity demand for future time steps. In this research, we use short-term load forecasting techniques. The short-term load forecasting used in this work is detailed in section 3.2. There, a combined load forecast model is built based on 13 individual forecasts. The first set of load forecasting models is based on a linear regression model with Tao's Vanilla benchmark model. These 9 sister forecasts are created by choosing the number of hourly and daily averaged lags from 0, 1, and 2, termed LinReg00 to LinReg22, where the first number denotes the number of hourly lag and the second is the number of daily averaged lags. The second forecast set consists of two sisters from the k-nearest neighbor forecasts family, termed 2NN and 8NN. Finally, two sister forecasts from the ARIMA model family, termed ARIMA6 and ARIMA10 are used, where the degrees of autoregressive and moving average models are 7 and 6, respectively, the integrator lag is one, and the seasonality is chosen between 6 and 10.

Since we ultimately use this combined load forecast model in the upper level controller to estimate the surrogate generator excess energy over a horizon length, we modified the combined model by varying the weights of each individual forecast over the horizon:

$$\hat{Q}_l(k+j|k) = \sum_{i=1}^{n_f} w_{i,j}\hat{Q}_i(k+j|k) \tag{37}$$

Here, $Q_l(k+j|k)$ is the load forecast for j step ahead calculated at the kth time-step, and $w_{i,j}$ is the weight of ith individual forecast in the jth time-step.

In order to find the optimum set of weights for this paper, we calculated all 13 individual forecast over a 4 time-step horizon for 8760 hours of year 2013 based on the real load data of 2007 to 2012 as described in 1.8.2. Then we formulated the following optimization problem to find the optimum weights:

$$\begin{aligned} \underset{\underline{w}}{\text{minimize}} \quad & \text{MAPE} = \frac{1}{n}\sum_{i=1}^{n}\left(\frac{|Q_{l,i} - \hat{Q}_{l,i}|}{Q_{l,i}}\right) \\ \text{subject to} \quad & \sum_{i=1}^{13} w_{i,j} = 1,\ j = 1, 2, ..., 4 \\ & 0 \preceq \underline{w} \preceq 1. \end{aligned} \tag{38}$$

where MAPE is the mean absolute percentage error, and $Q_{l,i}$ and $\hat{Q}_{l,i}$ are the actual and foretasted electricity demand at step i, and n is the size of training data. The optimization problem was solved by sequential quadratic method.

CHAPTER 4: Candidate Control Tools

In this chapter, the candidate control tools upon which the proposed hierarchical control structure is built are described. The first candidate tool is a Lyapunov-based switched extremum seeking (LSES) controller, which is detailed in Section 4.1. The second controller used in this research is model predictive control (MPC), which is described in Section 4.3. In order to assess the real-time performance of theses controllers, the surrogate power deficit metric is used. This metric is detailed in Section 3.3.1.

One of the most prevalent methods for optimization of unknown systems is extremum seeking (ES). ES is a (typically) non-model-based control scheme that is used to find the optimal operating point of an unknown system in real time [45]. ES has been applied to both static plants ([57, 58, 59]) and dynamic ones ([60, 61, 62]). ES strategies typically employ a periodic perturbation signal to hunt for an optimal operating condition. A well-documented challenge of perturbation-based extremum seeking occurs when the controller has identified the optimum setpoint. At this point, the system will enter a limit cycle around the optimal point rather than converging to the optimal value. Because of this, optimality is sacrificed because the controller operates around, but not at, the optimal point. Furthermore, substantial control effort is expended in applying continual perturbations around the optimal operating point.

In response to the aforementioned challenges surrounding conventional ES, [63] and [64] have developed a Lyapunov-based switched extremum Seeking (LSES) strategy that decreases the amplitude of the perturbation when convergence upon the optimal operating point has been detected. This consequently diminishes the size of the limit

cycle around the optimal point. The aforementioned LSES strategy, which has been applied to maximum power point tracking (MPPT) for photo-voltaic (PV) arrays in [63], [64], [65], [66], and [67], represents an ideal formulation for the present altitude optimization problem. This is because it is essential to optimize *net* power output, which requires a balance between hunting for the optimal altitude and curtailment of the control energy that is expended in hunting once the optimal altitude has been converged upon. Section 4.1 details an initial LSES scheme that has been implemented and validated in isolation within this research.

On the other hand, MPC is capable of employing global optimization tools for minimizing its underlying cost function, which makes it a seemingly strong candidate control tool for the altitude optimization problem. However, the global nature of the solution is limited to the finite horizon length of the MPC optimization and the grid resolution used by the underlying optimization scheme. This becomes particularly important when the optimization is performed over a partially-observable randomly-varying environment, where uncertainty (modeled through a standard deviation of variance of an estimated state) must be included as a part of the system state in order to use deterministic optimization tools. An MPC formulation for the altitude optimization problem at hand is described in details in Section 4.3.

4.1 Extremum Seeking Control

The first attempt to solve the altitude optimization problem in this work was to implement extremum seeking (ES) controller in isolation to optimize the net energy production of the AWE system. This controller is also implemented as a part of the final hierarchical structures, as described in Chapters 5 and 6. In this chapter, after a brief introduction of conventional ES and Lyapunov-based ES (LSES), the control strategy used to optimize the energy production without having a prior knowledge of the wind shear profile is described.

4.1.1 Mathematical Formulation

Extremum seeking control is a (typically) non-model-based real-time optimization approach for systems where the knowledge of the optimal operating point is limited or unknown. A conventional ES scheme, which is described in [45], is illustrated in the context of the present altitude optimization problem in Fig. 4.1. Variables of the block diagram are introduced in Table 4.1.

4.1.2 Conventional Extremum Seeking Control

In the conventional configuration of ES and in order to find the optimal control input of z^*, the signal z is formed by adding a sinusoidal perturbation $a_0 \sin(\omega t)$ to $\hat{z}$, where $\hat{z}$ is the *estimated* value of the optimal operating altitude. Upon driving the physical system to the altitude, z, the AWE system produces a net power output approximated by P, which is a function of the wind speed at altitude z:

$$P = k_1 \min(v_{\mathrm{w}}(z), v_{\mathrm{r}})^3 - k_2 v_{\mathrm{w}}^2 - \bar{k}_3 v_{\mathrm{w}}^2 |\dot{z}| \tag{1}$$

The calculated output then passes through a washout filter and is multiplied by the same perturbation signal, $\sin(\omega t)$. The resulting signal passes through a low-pass filter and then an integrator, and a new estimate of $\hat{z}$ is produced in the direction of increasing P.

4.1.3 Lyapunov-Based Switched Extremum Seeking Control

While ES converges to a local minimum or maximum (in an average sense) of an unknown nonlinearity in real-time, conventional ES enters a limit cycle around this point instead of asymptotically converging. In order to mitigate losses in optimality that result from this continual sinusoidal perturbation around the optimum, [63] proposes a switched control scheme that reduces the size of perturbation by decreasing the amplitude a_0 after converging within the interior of a neighborhood around the optimal point. The switch proposed in [63] is determined by leveraging a Lyapunov

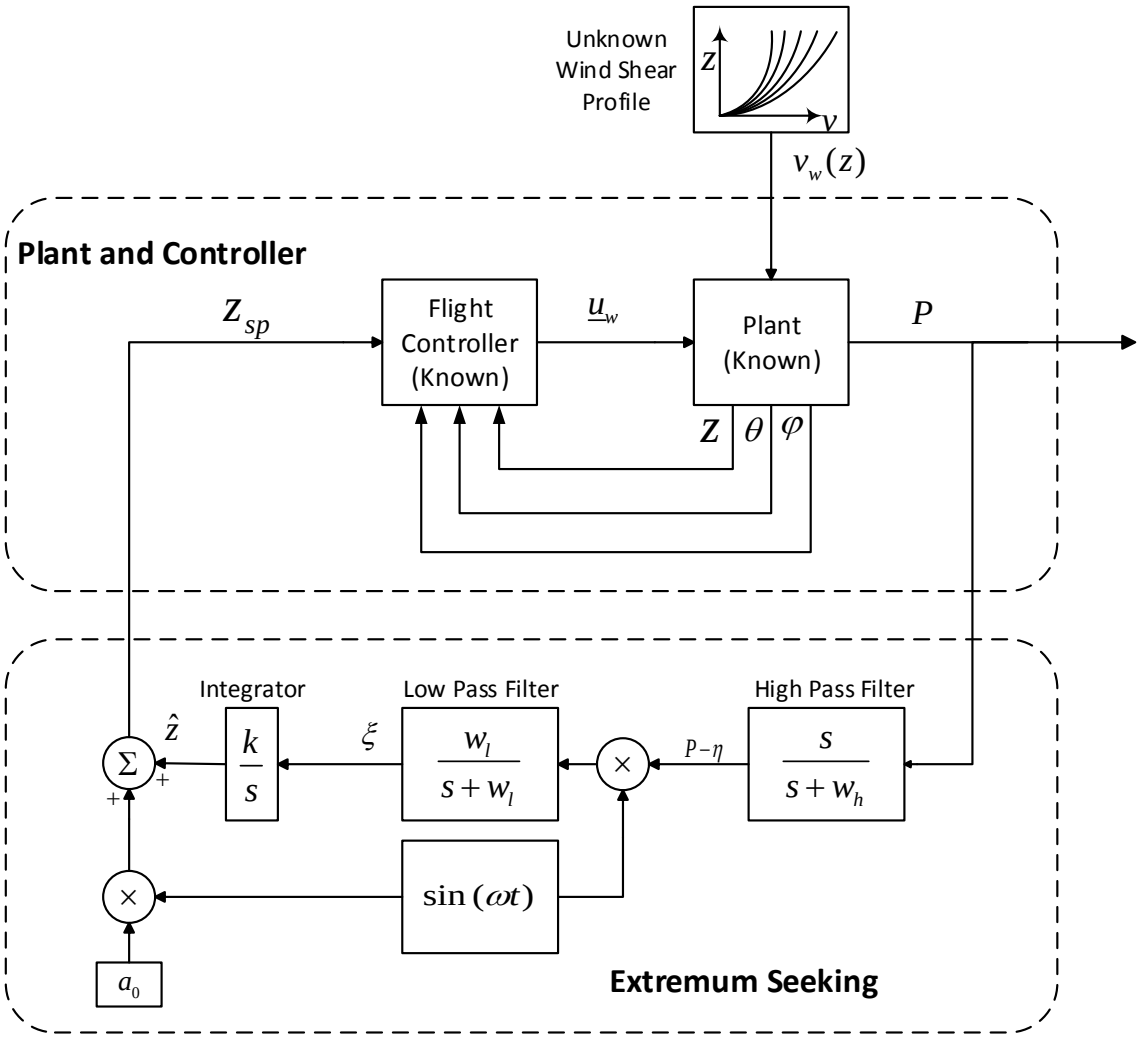

Figure 4.1: Conventional extremum seeking control scheme, as applied to AWE system altitude control.

function designed from an averaged model of the original ES feedback system to estimate the proximity to the optimal point.

In the context of the altitude optimization application at hand, a block diagram for the LSES strategy is shown in Fig. 4.2. When the output of the Lyapunov function is greater than the switch threshold, it means that the signal z is not close enough to z^*, and the amplitude of the perturbation remains equal to a_0. ES in this mode continues to apply a full-sized perturbation (of amplitude a_0) until converging closely enough to z^*. The switch state changes once z is within a sufficiently small region around z^*.

Table 4.1: Parameters in ES Block Diagram

Variable	Description	Unit
z	Altitude	m
P	Objective function (1)	kW
z_{sp}	Setpoint altitude	m
η	Low-level noise	kW
$\hat{z}$	Estimated altitude	m
ξ	Filtered control input	m/s
z^*	Optimal altitude set-point	m
x_a	Average state variable	-
K	Integrator gain	-
ω	Perturbation frequency	rad/s
ω_H	High-pass filter frequency	rad/s
ω_L	Low-pass filter frequency	rad/s
θ	Pitch angle	deg
ϕ	Roll angle	deg
u_m	Control command	m/s
a_0	Perturbation amplitude	m

In this region, the amplitude of perturbation decays. The full-sized perturbation will be reinstated once z^* changes and z becomes sufficiently different than the optimum altitude.

The Lyapunov function used in LSES is a function of an *averaged* (over one oscillation period) state variable, given by:

$$x_a = \frac{\omega}{2\pi} \int_{t-\frac{2\pi}{\omega}}^{t} x(\tau) d\tau, \tag{2}$$

where:

$$x = [\tilde{z} \quad \xi \quad \tilde{\eta}]^T. \tag{3}$$

In defining the state variable in (3), a new coordinate system is used, which shifts the equilibrium/optimal operating point to the origin:

$$\tilde{z} = \hat{z} - z^* \tag{4}$$

$$\tilde{\eta} = \eta - P(z^*) \tag{5}$$

The switch shown in the Fig. 4.2 operates based on the value of a quadratic Lyapunov function, $V(x_a)$, where $V(x_a)$ provides a measure for the proximity of the averaged values (over one extremum seeking period) of $\hat{z}$ and η to their estimated optimal values:

$$V(x) = \frac{1}{2} x^T \bar{P} x, \tag{6}$$

In this work, V is constructed by solving the following Lyapunov equation for $\bar{P}$ under the conditions $Q = Q^T \succ 0$:

$$\bar{P} J_a + J_a^T \bar{P} = -Q \tag{7}$$

where J_a is the Jacobian that approximates the system dynamics near the equilibrium and has been introduced by [64] as follows:

$$J_a = \begin{bmatrix} 0 & K' & 0 \\ \frac{\omega'_L}{2} h''(0) a_0 & -\omega'_L & 0 \\ \omega'_H h'(0) & 0 & -\omega'_H \end{bmatrix}$$

Here, K', ω'_L , and ω'_H are positive constants:

$$K' = \frac{k}{\omega}, \tag{8}$$

$$\omega'_L = \frac{\omega_L}{\omega}, \tag{9}$$

$$\omega'_H = \frac{\omega_H}{\omega}, \tag{10}$$

and the function $h(\Theta) = P(z^* + \Theta) - P(z^*)$ satisfies the following properties:

$$h(0) = 0 \tag{11}$$

$$h'(0) = P'(z^*) \tag{12}$$

$$h''(0) = P''(z^*) < 0 \tag{13}$$

$$h'''(0) = P'''(z^*) < 0 \tag{14}$$

Ultimately, the size of the perturbation signal, $a(t)$, decays when $V(x_a)$ is sufficiently small but remains full-sized otherwise, according to the following relationship:

$$a(t) = \begin{cases} a_0 \quad if \quad V(x_a) > \epsilon \\ \max\{a_{min}, -\gamma \int_{t_{sw}}^{t} a(\tau) d\tau\}, if \quad V(x_a) \leq \epsilon \end{cases} \tag{15}$$

where $a(t_{sw}) = a_0$, x_a is the state variable which is defined in (2), $V(x_a)$ is the value of Lyapunov function at the point x_a as defined in (6), γ is the rate of shrinking for perturbation amplitude, t_{sw} is switching time, and a_{min} is the minimum allowable perturbation size.

Remark 1 (Estimation of z^*). Given that the optimum altitude (z^*) and corresponding power output ($P(z^*)$) are unknown a priori, an estimation procedure is used to

Table 4.2: Parameters in LSES Block Diagram

Variable	Description	Unit
z	Altitude	m
P	Objective function (1)	kW
z_{sp}	Setpoint altitude	m
η	Low-level noise	kW
$\hat{z}$	Estimated altitude	m
ξ	Filtered control input	m/s
z^*	Optimal altitude set-point	m
x_a	Average state variable	-
K	Integrator gain	-
ω	Perturbation frequency	rad/s
ω_H	High-pass filter frequency	rad/s
ω_L	Low-pass filter frequency	rad/s
θ	Pitch angle	deg
ϕ	Roll angle	deg
$\underline{u}_w$	Control command	m/s
a_0	Perturbation amplitude	m
t_{sw}	Switching time	s
ϵ	Switching threshold	-
γ	Amplitude shrink factor	-

calculate *approximate* values of z^*, $P(z^*)$, h', and h'' to be used in (4), (5) and (7). To do this, h' and h'' at the current altitude are estimated using numerical differentiation based on the current and previous values of P and P'. Having the values for P' and P'' at the current altitude, z^* is estimated via extrapolation, approximating the power output to be locally quadratic in z. Previous works ([63] and [64]) have found the algorithm to be robust to estimation errors.

4.2 Stability Analysis and Implementation of LSES

This section includes the design and implementation of an LSES controller in isolation for the altitude optimization problem. Subsection 4.2.1 begins with the stability and convergence analysis of LSES control schemes for this application. Then, the altitude control results using an isolated LSES controller show how this approach

improves the net energy generation.

4.2.1 Stability of LSES

In this subsection, sufficient conditions for stability of the proposed LSES scheme are presented based upon results from [60] and [63]. Then, it is shown that these assumptions hold for the altitude optimization application at hand. In order to conduct a rigorous stability analysis, a simplified model for the altitude adjustment dynamics is utilized and is depicted in Fig. 4.3. Because it is well-established through both simulation and experimental results (see [44]) that altitude tracks the specified set-point, z_{sp}, subject to rate limitations, the simplified altitude adjustment dynamics include only a rate limiter and first-order dynamics that characterize the approximate mechanical system time constant. It is the wind shear profile that adds the complexity to the optimization problem and motivates the use of LSES.

As a first step to assessing the general stability conditions for LSES, we consider the following *general* nonlinear system:

$$\begin{aligned} \dot{\chi} &= f(\chi, u), \\ y &= h(\chi) \end{aligned} \tag{16}$$

where $\chi \in \mathbb{R}^n$ is the state, $u \in \mathbb{R}$ is the input, $y \in \mathbb{R}$ is the output, and $f : \mathbb{R}^n \to \mathbb{R}$ and $h : \mathbb{R}^n \to \mathbb{R}$ are smooth. [60] proves stability of conventional ES for the general system structure described above in (16). [63] shows that applying a Lyapunov-based switch to the ES using an averaging operator does not affect the stability of the system. The stability criteria presented by [60] will be reviewed first, and then the validity of these criteria for our problem will be checked.

Suppose one uses a smooth control law that is parameterized as follows:

$$u = \alpha(\chi, \theta), \tag{17}$$

$$\dot{\chi} = f(\chi, \alpha(\chi, \theta)), \tag{18}$$

where θ is a control parameter. [60], [63], and [64] show that the stability of ES for the general nonlinear dynamic system of (16) is achieved under the following assumptions, which will be shown to hold for our particular altitude optimization problem:

Assumption 1: *There exists a smooth function* $l : \mathbb{R} \to \mathbb{R}^n$ *such that:*

$$f(\chi, \alpha(\chi, \theta)) = 0 \text{ if and only if } \chi = l(\theta) \tag{19}$$

Assumption 2: *For each* $\theta \in \mathbb{R}$*, the equilibrium* $x = l(\theta)$ *of the system (18) is locally exponentially stable with decay and overshoot constants uniform in* θ*.*

Assumption 3: *There exists* θ^* *such that:*

$$(h \circ l)'(\theta^*) = 0 \tag{20}$$

$$(h \circ l)''(\theta^*) < 0 \tag{21}$$

Under the aforementioned assumptions, it is shown in [60] that the control parameter and states converge to their optimal values and corresponding steady states, under a general ES algorithm. It is shown in [63] that this same result extends to the LSES algorithm, as long as Assumptions 1-3 are satisfied.

The altitude optimization problem at hand represents an analog to the general LSES framework, where the general LSES variables and corresponding altitude optimization-specific variables are summarized in Table 4.3. The following proposition establishes the local exponential stability of the AWE system around the optimal altitude, de-

noted as z^*, under the specific strategy that is depicted in Fig. 4.3:

Proposition 4.2.1. *Consider the altitude optimization system of Fig. 4.3, under Assumptions 1-3, with variable equivalences summarized in Table 4.3. There exists a ball of initial conditions around the point* $(z, \hat{z}, \xi, \eta) = (z^*, z^*, 0, P(z^*))$ *and constant* $\bar{\omega}$, $\bar{\delta}$, *and* $\bar{a}$ *such that for all* $\omega \in (0, \bar{\omega})$, $\delta \in (0, \bar{\delta})$, *and* $a \in (0, \bar{a})$, *the solution* $(z(t), \hat{z}(t), \xi(t), \eta(t))$ *exponentially converges to an* $O(\omega + \delta + a)$*-neighborhood of that point. Furthermore,* $P(t)$ *converges to an* $O(\omega + \delta + a)$*-neighborhood of* $P(z^*)$.

Proof 4.2.1. The proof of proposition 4.2.1 requires verification of the validity of Assumptions 1-3 on the specific altitude optimization problem. To verify Assumption 1, note that the system of Fig. 4.3 can be described by:

$$\dot{z} = \begin{cases} \frac{1}{\tau}(z_{sp} - z), & r_{min} \leq \frac{1}{\tau}(z_{sp} - z) \leq r_{max}, \\ r_{max}, & \frac{1}{\tau}(z_{sp} - z) > r_{max}, \\ r_{min}, & \frac{1}{\tau}(z_{sp} - z) < r_{min}. \end{cases} \tag{22}$$

where r_{max} is the maximum achievable rate of altitude variation. Clearly, $\dot{z} = 0$ if and only if $z = z_{sp}$, thereby satisfying Assumption 1. For initial altitudes sufficiently close to z_{sp}, the dynamics are linear with a single eigenvalue at $\lambda = -\frac{1}{\tau}$, from which it follows immediately that the dynamics are uniformly (locally) exponentially stable, thereby satisfying the conditions of Assumption 2. Noting that $P(v_{\mathrm{w}}, \dot{z})$ is a function only of v_{w} at equilibrium, it immediately follows from examination of the wind shear profile at optimal altitude that $P^{'}(z^*) = 0$ and $P^{''}(z^*) < 0$. Therefore, Assumption 3 is satisfied, which completes the proof. ■

Table 4.3: Analogy Between Theorem 3.1 and Altitude Optimization Problem

Generic Variable	Altitude Optimization Variable
θ	z_{sp}
χ	z
$y(\chi)$	$P(z)$
$\alpha(\chi, \theta)$	z_{sp}
$l(\theta)$	z

4.2.2 Results of Implementing LSES Control Scheme

Results of the LSES control strategy shown in Fig. 4.3 have been obtained for the wind data provided in [7] and described in Section 1.8.1. Relevant parameters for calculating instantaneous power production (9), as well as LSES-specific parameters, are summarized in Tables 4.4 and 4.5:

Table 4.4: Cost Function Parameters

Parameter	Description	Value
v_{r}	Rated wind speed of the turbine	12 m/s
k_1	Coefficient of power (related to the power curve of the turbine)	0.0579
k_2	Coefficient of penalty for power required in winches motors	0.09
k_3	Coefficient of power required to maintain the altitude	1.08

In order to demonstrate the advantages of the LSES algorithm proposed in this paper, the system performance under four different control configurations, termed "scenarios" are compared.

Scenario 1: Minimum Constant Altitude (146m): The first scenario is intended to be representative of conventional towered wind turbines. For this comparison, data from the lowest available altitude of 146m is used. This altitude is approximately

Table 4.5: Extremum Seeking Parameters

Parameter	Description	Value	Unit
k	Integrator gain	$3e-5$	kW/m
a	Perturbation magnitude	10	m
ω	Perturbation frequency	0.0262	rad/sec
ω_H	High-pass filter (washout filter) frequency	0.0236	rad/sec
ω_L	Low-pass filter frequency	0.0024	rad/sec
ϵ	Switching threshold	$1e-9$	-

equal to the hub height of the highest towered systems.

Scenario 2: Offline Optimum Constant Altitude: The second scenario involves flying the AWE system at an *optimum constant altitude*. This optimal constant altitude was determined by off-line calculation of energy generation at different altitudes using given wind data. It is worth noting that this calculation requires knowledge of the future wind conditions and is therefore not practically implementable; however, this scenario represents an upper bound on the potential of any constant altitude algorithm. For the time period of interest in this work, the optimum constant altitude was calculated to be equal to 1236m.

Scenario 3: Conventional Extremum Seeking Control: The third control algorithm employs an ES controller to find the optimum altitude. The conventional ES control strategy used in this algorithm addresses the unknown nature of the wind shear profile and applies a sinusoidal perturbation to track the optimal altitude.

Scenario 4: Lyapunov-Based Switched Extremum Seeking Control: The fourth scenario is LSES-based altitude optimization, which curtails the size of the ES perturbation signal to minimize energy consumption once an optimal power generation point has been reached.

Cost function parameters are given in Table 4.4, and Table 4.5 shows the parameters used in conventional and Lyapunov-based switched ES. The maximum allowable

altitude was set to be 1600m, and the run-time was set to 15 days.

Fig. 4.4 and Fig. 4.5 show the resulting altitude path for the four different scenarios. Fig. 4.5 shows a zoomed-in version of Fig. 4.4, which shows how the size of perturbation shrinks in the LSES control strategy as the AWE system approaches the optimal altitude.

Remark 2 (Convergence to Optimal Altitude). As described in Proof 4.2.1, LSES is *locally*, not globally convergent. Consequently, the altitude path of conventional ES and LSES shown in Fig. 4.4 do exhibit differences, especially when the wind shear profile and corresponding optimal altitude change significantly.

Fig. 4.6 demonstrates that the conventional extremum seeking control strategy results in *less* net energy generation at the end of the day than even the offline-optimized constant altitude control strategy. However, the *LSES* results in superior energy production performance when compared to either of the competing scenarios. This is accomplished by combining altitude optimization with consideration of the energy that is used to adjust the altitude.

Fig. 4.7 compares the wind velocities at the operating altitude for the candidate control scenarios.

4.3 Economic Model Predictive Control

Another candidate control strategy for control of altitude and the integrated system is model predictive control (MPC). This section addresses implementation of an *economic* MPC strategy. This control strategy will also be included as the upper level controller of the final integrated controller design as introduced in Chapters 5 and 6.

MPC is a control approach that attempts to find the optimal operating point by minimizing a cost/objective function subject to constraints, over a receding horizon. Unlike extremum seeking, MPC is well-suited to make use of a statistical model for the wind/weather profile based on available historical data. Section 3.1 addresses the statistical characterization of the wind shear profile. This statistical characterization

method has been developed in collaboration with Mr. Shamir Bin Karim in the UNCC CORE lab.

4.3.1 Economic MPC Basics

The basic idea of MPC is to exploit a model of a process to predict the future evolution of the system and to compute control actions by minimizing a cost function that depends on these predictions. In performing this optimization, MPC is one of a select few control strategies that can explicitly consider hard constraints on both the control signal and the system states.

Economic Model Predictive Control has been used in many industrial problems where the control objective involves maximizing profitability rather than tracking setpoints. Application of this control technique in process industry have been reviewed in [68] and [69]. To appreciate the differences between traditional (tracking) MPC and economic MPC, we briefly review both mathematical formulations here. The formulation for tracking MPC is as follows:

$$\begin{aligned} \underset{u\in S(\Delta)}{\text{minimize}} \quad & \sum_{i=0}^{N}(|\tilde{x}(t_i)|^2_{Q_c} + |u(t_i)|^2_{R_c}) \\ \text{subject to} \quad & \dot{\tilde{x}}(t) = f(\tilde{x}(t), u(t), 0) \\ & \tilde{x}(0) = x(\tau_k) \\ & f(\tilde{x}(\tau_N), u_s) = 0, u_s \in U \\ & g(\tilde{x}(t), u(t)) \leq 0, \forall t \in [0, \tau_N) \end{aligned} \tag{23}$$

where $x \in X \subseteq \mathbb{R}^{n_x}$ is the state vector, $\tilde{x}$ is the tracking error, $u \in U \subset \mathbb{R}^{n_u}$ is the manipulated input vector, positive definite matrices $Q_c \succ 0$ and $R_c \succ 0$ are tuning matrices that manage the trade-off between the speed of response and the cost of control action, τ_k is the time sequence where $\tau_k = \tau_0 + k\Delta$, $g : \mathbb{R}^{n_x} \times \mathbb{R}^{n_u}$ denotes the process constraints which may include input and state constraints as well as mixed input and state constraints, and N is the prediction horizon.

Meanwhile, EMPC can be characterized by the following optimization problem:

$$\begin{aligned} \underset{u \in S(\Delta)}{\text{minimize}} \quad & \sum_{i=0}^{N} l_e(\tilde{x}(t_i), u_s) \\ \text{subject to} \quad & \dot{\tilde{x}}(t) = f(\tilde{x}(t), u(t), 0) \\ & \tilde{x}(0) = x(\tau_k) \\ & f(\tilde{x}(\tau_N), u_s) = 0, u_s \in U \\ & g(\tilde{x}(t), u(t)) \leq 0, \forall t \in [0, \tau_N) \end{aligned} \tag{24}$$

where $l_e : \mathbb{R}^{n_x} \times \mathbb{R}^{n_u} \to \mathbb{R}$ is used as a measure of the instantaneous process operating cost (or profit), Δ is the sampling period.

The main difference between MPC and EMPC is that the traditional MPC tries to track a prescribed setpoint, whereas EMPC attempts to maximize some profitability metric. In other words, the objective function of EMPC is an explicit or implicit function of price or cost of the product. In the application at hand, the profitability is the total renewable energy production of the system, which translates directly into profitability.

EMPC has been implemented in many applications, including chemical process systems ([68, 70, 69, 71, 72, 73]), power systems ([74, 75, 76, 77, 78, 79]), and HVAC ([80, 81, 82]).

4.3.2 EMPC for Altitude Optimization Problem

For the spatiotemporal optimization problem at hand, the EMPC optimization aims to maximize the net power production with respect to the following simple dynamics:

$$z(k) = z_{sp}(k) \tag{25}$$

It dosed this, while incetivizing exploration, by maximizing a cost function, J,

subject to the constraints, as follows:

$$\begin{aligned} \underset{z(k)}{\text{minimize}} \qquad & J(\mathbf{z}(k)) = \sum_{i=k}^{k+T-1} \left[J_{\text{exploit}}(\mathbf{z}(i|k)) + w J_{\text{explore}}(\mathbf{z}(i|k)) \right] \\ \text{subject to} \qquad & \mathbf{z}(i|k) \in \Omega, i = k \ ... \ k+T-1 \end{aligned} \tag{26}$$

where T is the EMPC prediction horizon and $\mathbf{z}(k)$ is the altitude trajectory vector to be optimized, given by:

$$\mathbf{z}(k) = \left[\ \mathbf{z}(k|k) \quad \dots \quad \mathbf{z}(k+T-1|k) \ \right]^T. \tag{27}$$

The notation $\mathbf{z}(i|k)$ denotes the value of $z(i)$ for the optimization taking place at step k. Ω represents constraint set within which each instantaneous altitude set-point $\mathbf{z}(i|k)$ must belong. w_1 and w_2 are scalar weighting parameters that set the balance between exploration and exploitation in cost function. As is typical with MPC, the first term in the optimized control input trajectory represents the commanded control input. In this case, the commanded control input is the altitude *setpoint*, given by:

$$z_{sp} = \mathbf{z}^*(k|k), \tag{28}$$

where

$$\mathbf{z}^* = \arg\min_{\mathbf{z}(k)} J(\mathbf{z}(k)). \tag{29}$$

It is assumed in this work that an underlying lower-level flight control system regulates the system's operating altitude (z) to the set-point (z_{sp}). The efficacy of such an altitude control algorithm has been validated both numerically and experimentally in [83] and [44]; therefore, the assumption of this lower-level flight controller is well-founded.

The exploitation term in the cost function ($J_{\text{exploit}}(\mathbf{z}(i|k))$), is equal to the calculated surrogate power deficit P_{sur}, which is detailed in Section 3.3.1. In order to

prohibit excessive exploration, the amount of energy required to change the altitude is added to the exploitation cost function:

$$J_{\text{exploit}}(\mathbf{z}(i|k)) = P_{\text{sur}}(i|k) - w_1 k_3 E[(v_{\text{w}}(t(i), z))]^2 \frac{|\Delta z|}{\Delta t} \tag{30}$$

Here, w_1 is the energy consumption weight. The exploration term is given by:

$$J_{\text{explore}}(\mathbf{z}(i|k)) = \sum_{z'=z_{min}}^{z'=z_{max}} \hat{\sigma}^c \left(v_{\text{w}}(t(i), z')|\mathbf{D}, \mathbf{D}'\right) \tag{31}$$

where z_{max} and z_{min} are the upper and lower bound of explorable altitudes. $\mathbf{D}'$ is given by:

$$\mathbf{D}' = \begin{bmatrix} t(k) & \dots & t(i) \\ \mathbf{z}(k|k) & \dots & \mathbf{z}(i|k) \end{bmatrix}. \tag{32}$$

Thus, at each time step, the exploration term penalizes the 1-norm over altitude of the conditional standard deviation of the wind speed at each step in the EMPC horizon, conditioned upon all measurements taken up to step i. $\mathbf{D}'$ is included in the calculation of the exploitation term expressly for the purpose of considering the contribution of measurements taken *during* the EMPC prediction horizon on the conditional standard deviation of the wind speed prediction. Thus, the 1-norm that is penalized in (31) is kept small by continually exploring the available altitudes domain throughout the EMPC horizon. The results of altitude optimization using MPC are published in [9] and [84].

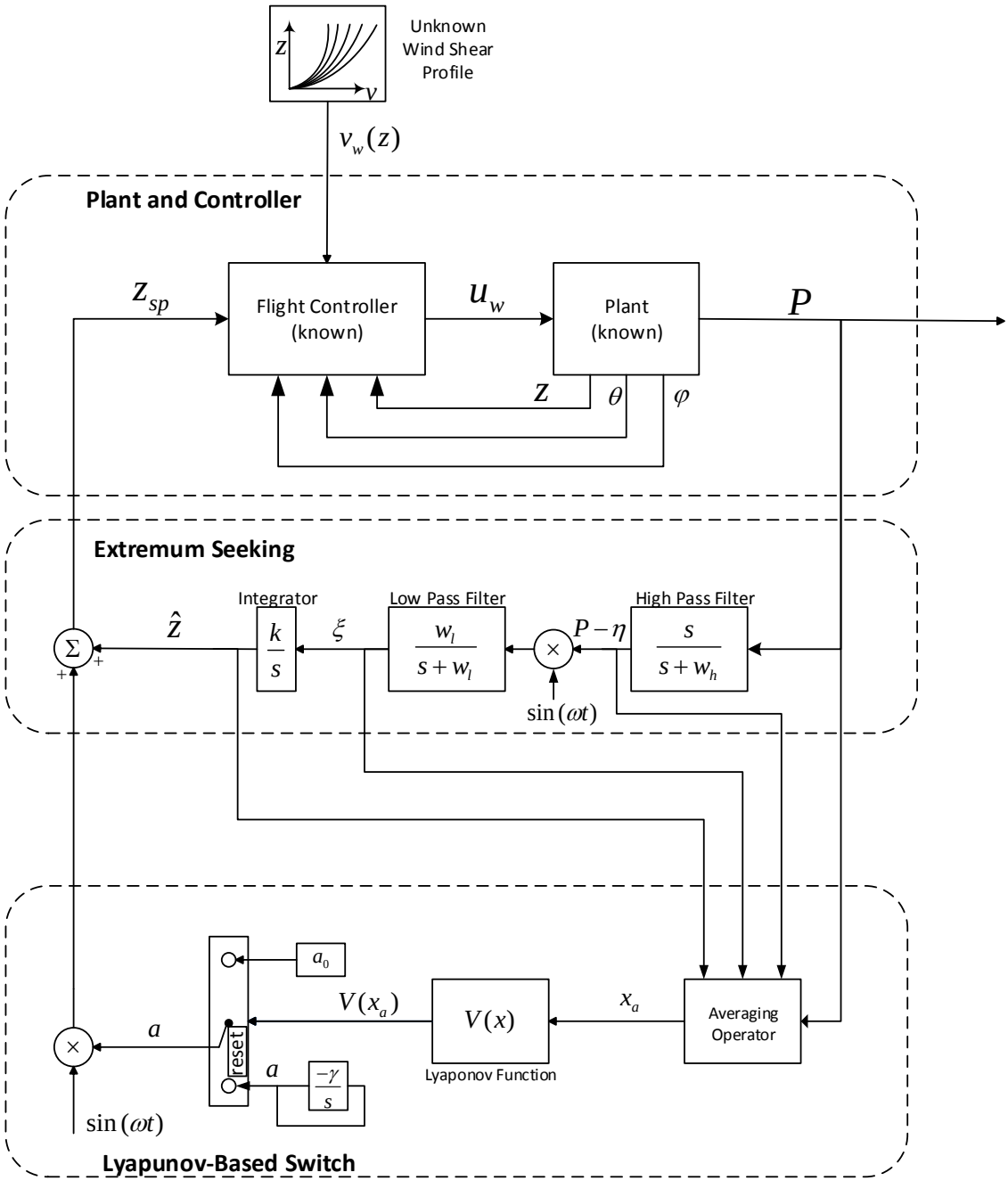

Figure 4.2: Lyapunov-based switched extremum seeking (LSES) control scheme, as applied to AWE system altitude control.

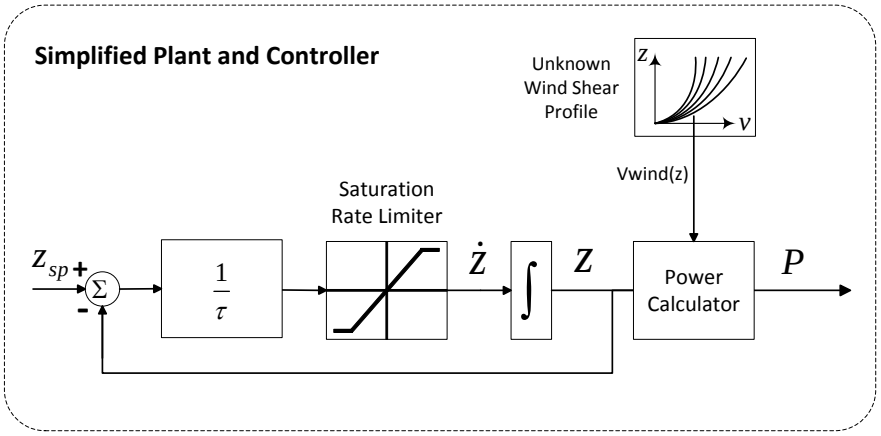

Figure 4.3: Simplified flight controller and plant as a combination of first order dynamics, rate limiter, and power calculation.

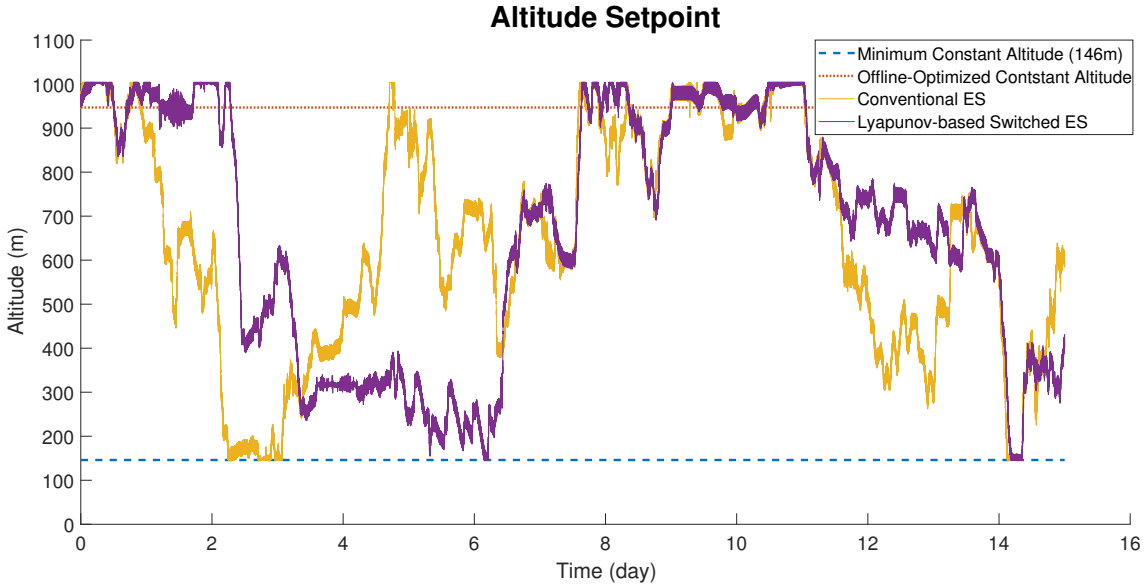

Figure 4.4: Altitude path for conventional ES, LSES, offline-optimized constant altitude, and minimum constant altitude (146m) control strategies.

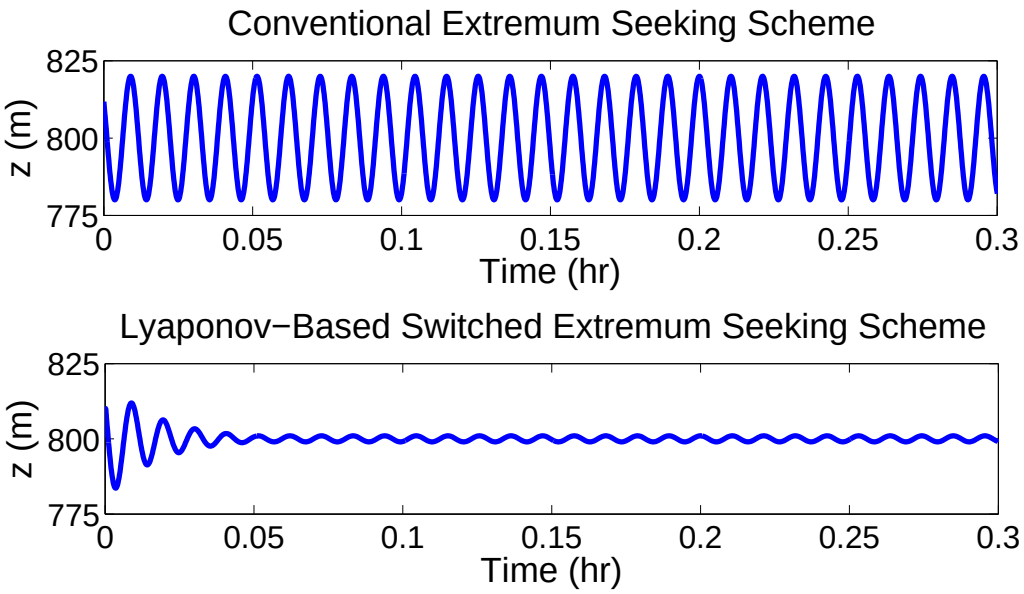

Figure 4.5: Zoomed-in version of Fig. 4.4 that shows the LSES control strategy decreasing the amplitude of the perturbation as the AWE system gets close to the optimal altitude.

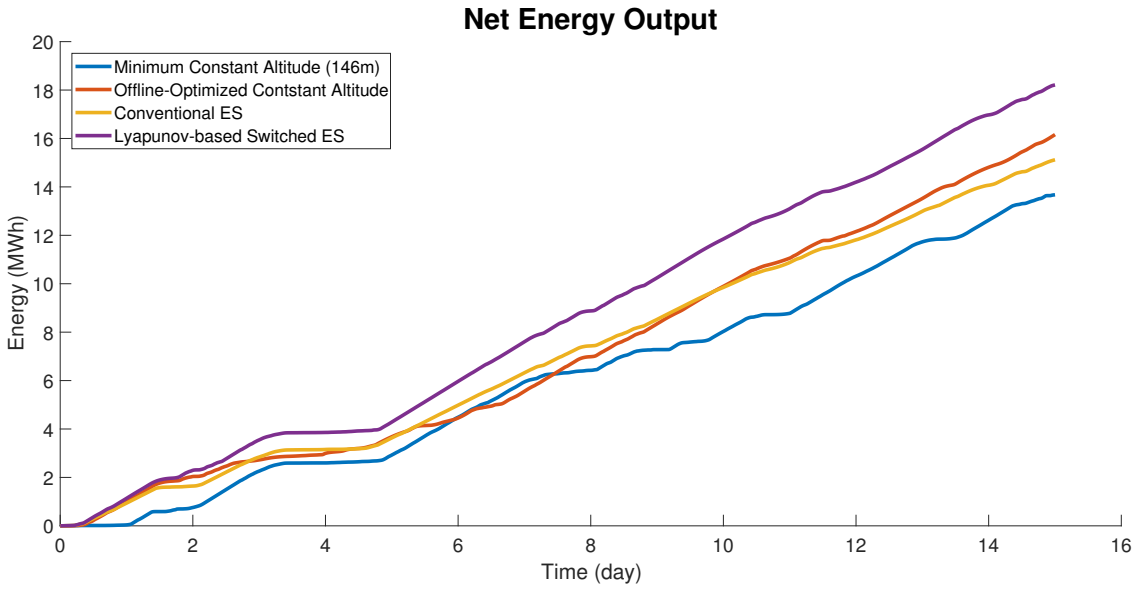

Figure 4.6: Net energy generation for four different control scenarios. Note that the offline-optimized constant altitude strategy is not implementable in practice (as the determination of the optimal constant altitude requires future wind information). However, it represents an upper bound on constant altitude performance.

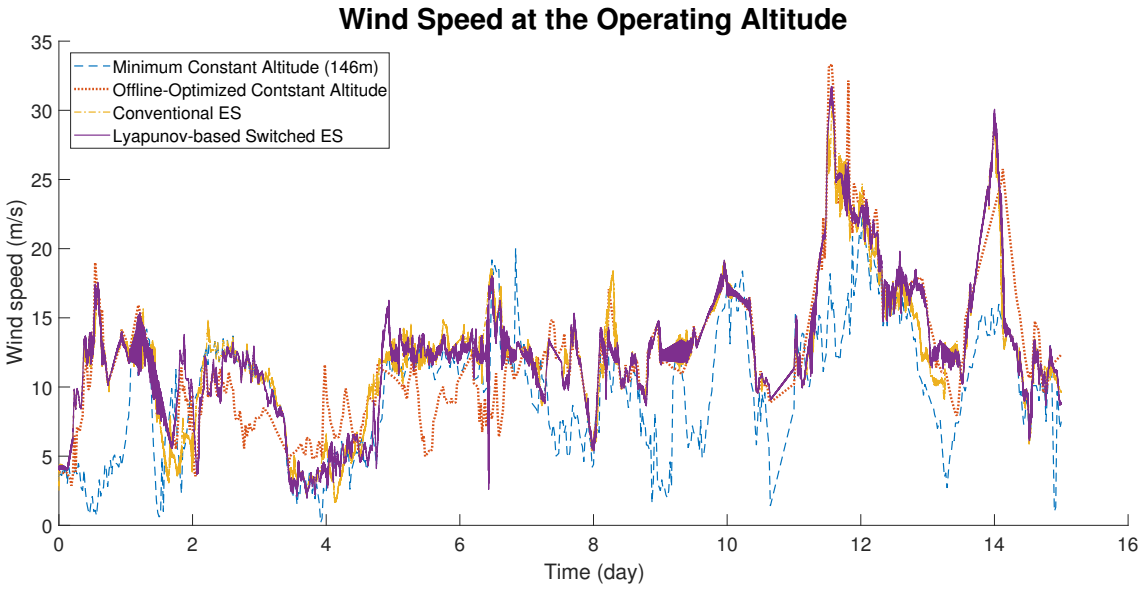

Figure 4.7: Wind velocity at operating altitude of AWE system with four proposed control scenarios

CHAPTER 5: Hierarchical Control Structures for Altitude Optimization of Standalone AWE Systems

The aforementioned MPC and Lyapunov-based switched ES (LSES) control strategies have their own pros and cons. While LSES is computationally inexpensive, it only guarantees local convergence to the optimum. Moreover, LSES as introduced in Section 4.1 does not utilize the available wind velocity data, measured prior to or during the course of operation. On the other hand, MPC, which is introduced in Section 4.3, is capable of employing global optimization tools for minimizing its underlying cost function. However, the global nature of the solution is limited to the finite horizon length of the MPC optimization and the grid resolution used by the underlying dynamic programming or exhaustive search. This becomes particularly important when the optimization is performed over a partially-observable, randomly-varying environment, where uncertainty (modeled through a standard deviation or variance of an estimated state) must be included as a part of the system state in order to use deterministic optimization tools. The MPC controller proposed in Section 4.3 relies on sequential quadratic programming (SQP) for the minimization or the underlying cost function, thereby leading to computational efficiency, but only guaranteeing convergence to local optima.

A critical evaluation of the aforementioned previous results reveals a trade-off between coarse, global optimization techniques and fine, local ones. In this work, we propose three novel mechanisms for fusing coarse, global techniques with fine, local ones in a hierarchical framework. Specifically, we address the following questions:

- What data should be exchanged between different control levels?

- What is the best hierarchical configuration based on MPC and LSES for the partially observable spatiotemporally varying problem at hand?

In fact, the answer to the first question depends on the choice of the controller for the different layers of the hierarchy. Fig. 5.1 provides a generic block diagram of the basic hierarchical control structure under consideration. In this block diagram, the variable χ, which is passed from the upper-level controller to the mid-level controller, represents a distinguishing feature between the three candidate control strategies.

For the hierarchical architectures considered in this work, Table 5.1 shows the controller options for upper and middle levels. In the first candidate control strategy, an upper-level coarse, global MPC selects an altitude set-point that dictates the local domain of altitudes that can be explored by a mid-level LSES controller. In the second candidate strategy, an upper-level coarse, global MPC, selects an altitude that dictates the local domain of altitudes that can be explored by a fine mid-level MPC optimization. In these two controllers, the upper level MPC finds the global optimum up to the grid resolution and finite horizon length, and the mid-level controller explores within the optimal altitude "bin." Finally, in the third candidate strategy, the upper-level controller estimates the difference between the optimal power output of the system and the output at the present altitude; this estimated difference, termed the surrogate power deficit, is used to adjust the perturbation amplitude for a mid-level LSES controller.

The hierarchical control structure of Fig. 5.1 also includes a lower-level flight controller that regulates altitude to its set-point, along with a turbine torque controller. The turbine torque controller is similar to the system described in [43], and the flight control system for the Altaeros BAT is discussed in [44]. Because these lower-level controllers have been validated through simulations and experiments in legacy work, they are not the focal point of this work.

We show through simulations, with actual wind shear data, that fused local-global

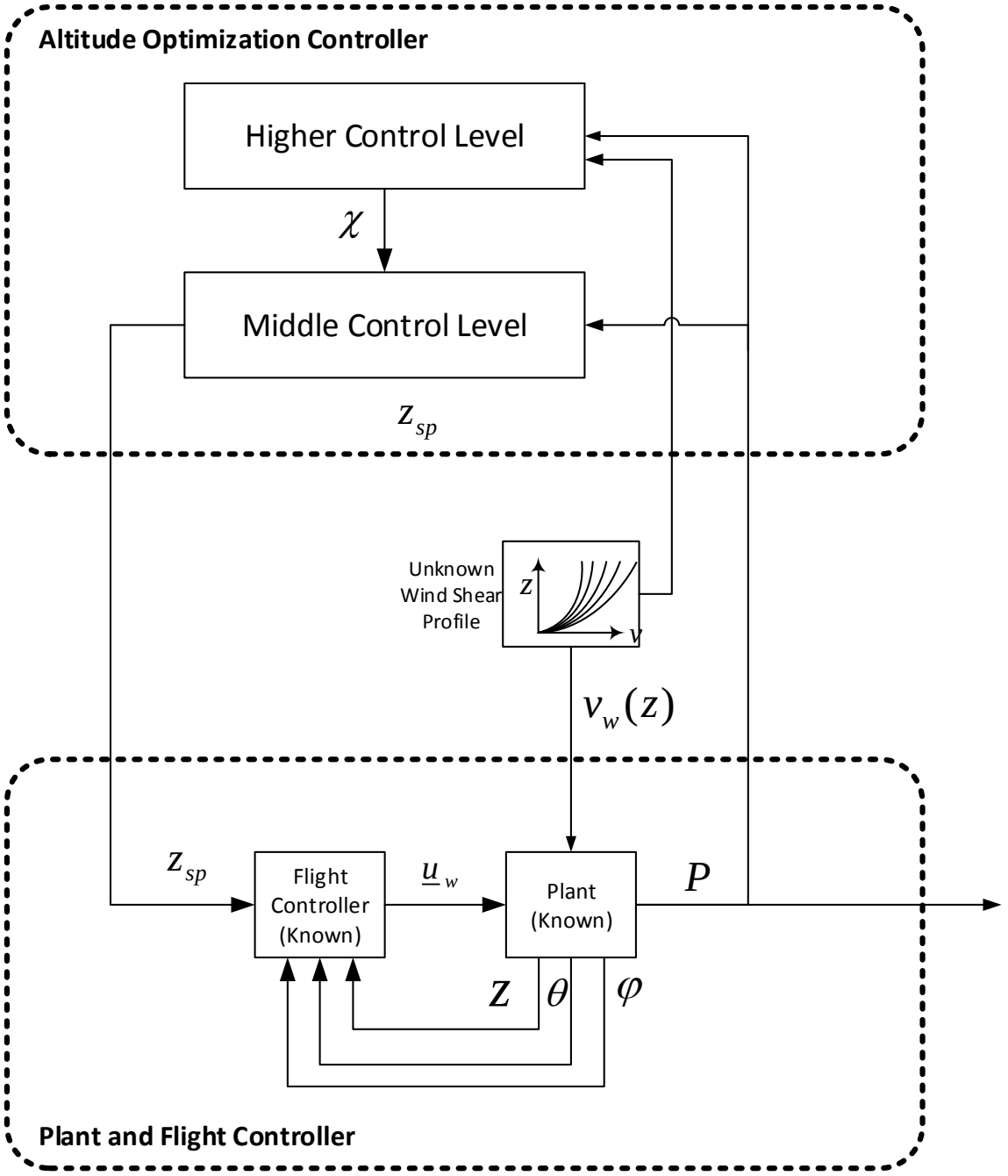

Figure 5.1: Basic block diagram showing the common proposed hierarchical altitude control structure for an AWE system.

Table 5.1: Controller Choice for Each Level of Candidate Hierarchical Structures

Candidate Structure	Upper level	Mid-level
MPC – LSES	Coarse MPC	LSES
MPC – MPC	Coarse MPC	Fine MPC
Globalized LSES	Calculation of LSES perturbation based on surrogate power deficit	LSES

controllers dramatically outperform corresponding standalone controllers. This is mainly because the hierarchical controllers are able to consider much finer altitude grids, within reasonable computational limitations, than their standalone, centralized counterparts [85].

5.1 Implementing MPC Over a Global, Quantized Grid

The MPC formulation for the altitude optimization problem is initially introduced in Section 4.3. Here, we focus on *globally minimizing* the MPC objective function of equation (26). We propose two candidate tools for performing this optimization in real time, namely an exhaustive grid search and dynamic programming. Both tools are restricted to a relatively coarse grid in order to ensure computational tractability.

5.1.1 Exhaustive grid search

The first candidate optimization tool is an exhaustive search algorithm over a predetermined altitude-time grid. This algorithm evaluates the value of cost function for all admissible altitude trajectories over the horizon to search for the lowest cost. Thus, this exhaustive search algorithm is as follows:
where Z is a set of all possible trajectories $\mathbf{z}(k)$.

This optimization algorithm guarantees global convergence to the optimum altitude trajectory, subject to the grid resolution and horizon length. However, the number of

Algorithm 1 Exhaustive grid search algorithm

1: **for** all $\mathbf{z}(k) \in Z$ **do**
2: $\quad J(\mathbf{z}(k)) = \sum_{i=k}^{k+r-1} J_{\text{exploit}}(\mathbf{z}(i|k)) + wJ_{\text{explore}}(\mathbf{z}(i|k))$
3: **end for**
4: $\mathbf{z}^*(k) = \arg\min(J(\mathbf{z}(k)))$

required function evaluations increases exponentially with altitude quantization level and horizon length. Denoting n as the number of allowable altitudes and r as the horizon length, the required number of full cost function evaluations at each time step for an exhaustive search algorithm, assuming that all altitudes are accessible, is given by:

$$N_{\text{exh}} = n^r. \tag{1}$$

5.1.2 Dynamic programming

As an alternative to an exhaustive grid search, dynamic programming (DP) is a very useful optimization tool that leverages Bellman's principle of optimality (see [86]). In particular, it can be easily applied to non-linear systems with or without constraints on the control and state variables.

In standard (deterministic) DP, only the present state and control decision are required to determine the next state and associated stage cost (i.e., the incremental cost of going from step i to step $i+1$). If either the stage cost or successor state are *probabilistic* functions of the control input, then the appropriate tool to solve the problem is stochastic dynamic programming (SDP) (see [87]). In order to use standard DP, the stage cost of making a particular control decision (i.e., selecting a particular altitude set-point) at step i must depend only on the control decision and the state at step i, not sequence of control decisions leading up to step i. To satisfy this requirement, we include both the altitude (z) and conditional standard deviation of our estimated wind shear profile ($\hat{\sigma}^c$) as states for the DP formulation. Specifically,

we take:

$$\mathbf{x}_{DP} = [z \quad \hat{\sigma}^c(v_{\mathrm{w}}(z_1)) \quad ... \quad \hat{\sigma}^c(v_{\mathrm{w}}(z_n))]^T, \tag{2}$$

where n is the number of allowable altitudes. As a result, the next value of $\mathbf{x}_{DP}$ and the corresponding stage cost are deterministic functions of the control decision.

Because the DP problem must be solved at each time step, and because the initial state ($\mathbf{x}_{DP}(k)$) is known, the most computationally efficient mechanism for DP for the altitude optimization problem at hand is *forward recursion*. By Bellman's principle of optimality, the optimal cost (and corresponding optimal path) from initial state $\mathbf{x}_{DP}(k)$, to state $\mathbf{x}_{DP}(i+1)$, through intermediate state $\mathbf{x}_{DP}(i)$, is given by:

$$J^*_{\mathbf{x}_{DP}(k)\to\mathbf{x}_{DP}(i+1)} = J^*_{\mathbf{x}_{DP}(k)\to\mathbf{x}_{DP}(i)} + J_{\text{exploit}}(\mathbf{x}_{DP}(i)) + wJ_{\text{explore}}(\mathbf{x}_{DP}(i)) \tag{3}$$

To evaluate the required number of function evaluations (computational complexity) versus grid coarseness for DP, we assume that altitude and conditional standard deviation (a characterization of uncertainty) values are discretized into n and p values, respectively. To be consistent with MPC formulation (23), r represents the MPC horizon length. The maximum required number of function evaluations for each DP optimization step, $N_{\mathrm{DP}}^{\max}$, assuming that all altitudes are accessible, is equal to:

$$N_{\mathrm{DP}}^{\max} = (r-1) \times n \times (n \times p^n) + n. \tag{4}$$

This expression for $N_{\mathrm{DP}}^{\max}$ can be interpreted as follows. Since the initial state is known, only n function evaluations are required at step k. At each of the $r-1$ successive steps, n control actions can be taken, and at most $n \times p^n$ states can be reached. Because some uncertainty states are not reachable, and are therefore *inadmissible*, these can be discarded in the DP implementation. Discarding inadmissible states at each step, the number of function evaluations from DP will never exceed those of an

exhaustive search. Thus, the required number of function evaluations with DP can be bounded by:

$$N_{\mathrm{DP}} \leq \min\{N_{\mathrm{exh}}, N_{\mathrm{DP}}^{\max}\} \tag{5}$$

Fig. 5.2 compares the required number of function evaluations for an exhaustive grid search (N_{exh}) and upper limit on function evaluations for DP ($\min\{N_{\mathrm{exh}}, N_{\mathrm{DP}}^{\max}\}$), considering horizon lengths of $r = 6$ and $r = 10$, altitude quantization levels $n \in [1, 10]$, and uncertainty quantization levels $p \in [1, 10]$. Because of the computational expense associated with including uncertainty as part of the state for DP, the exhaustive search is just as efficient as DP for large values of p and short horizon lengths (small r).

5.2 Candidate Hierarchical Structures

The MPC controller described in Section 4.3 guarantees global optimality over the prediction horizon, but only up to the grid resolution. On the other hand, LSES is computationally inexpensive relative to MPC, but it is a local optimization tool and does not use the available historical wind data that is logged prior to or during the course of operation of the AWE system [88].

In this work, we propose and critically assess three candidate hierarchical control structures that leverage the desired features of the aforementioned control strategies while circumventing their deficiencies. The first strategy, which we term the "MPC-LSES hierarchical controller", fuses a coarse, global MPC optimization at the upper level with LSES at the level below it. The second strategy, termed "MPC-MPC", fuses a coarse, global MPC optimization at the upper level with a fine MPC optimization over a smaller altitude domain and shorter horizon at the level below it. Finally, the third strategy, termed "Globalized LSES", uses the surrogate power deficit estimate from the upper level to adjust the size of the perturbation that is used by the LSES

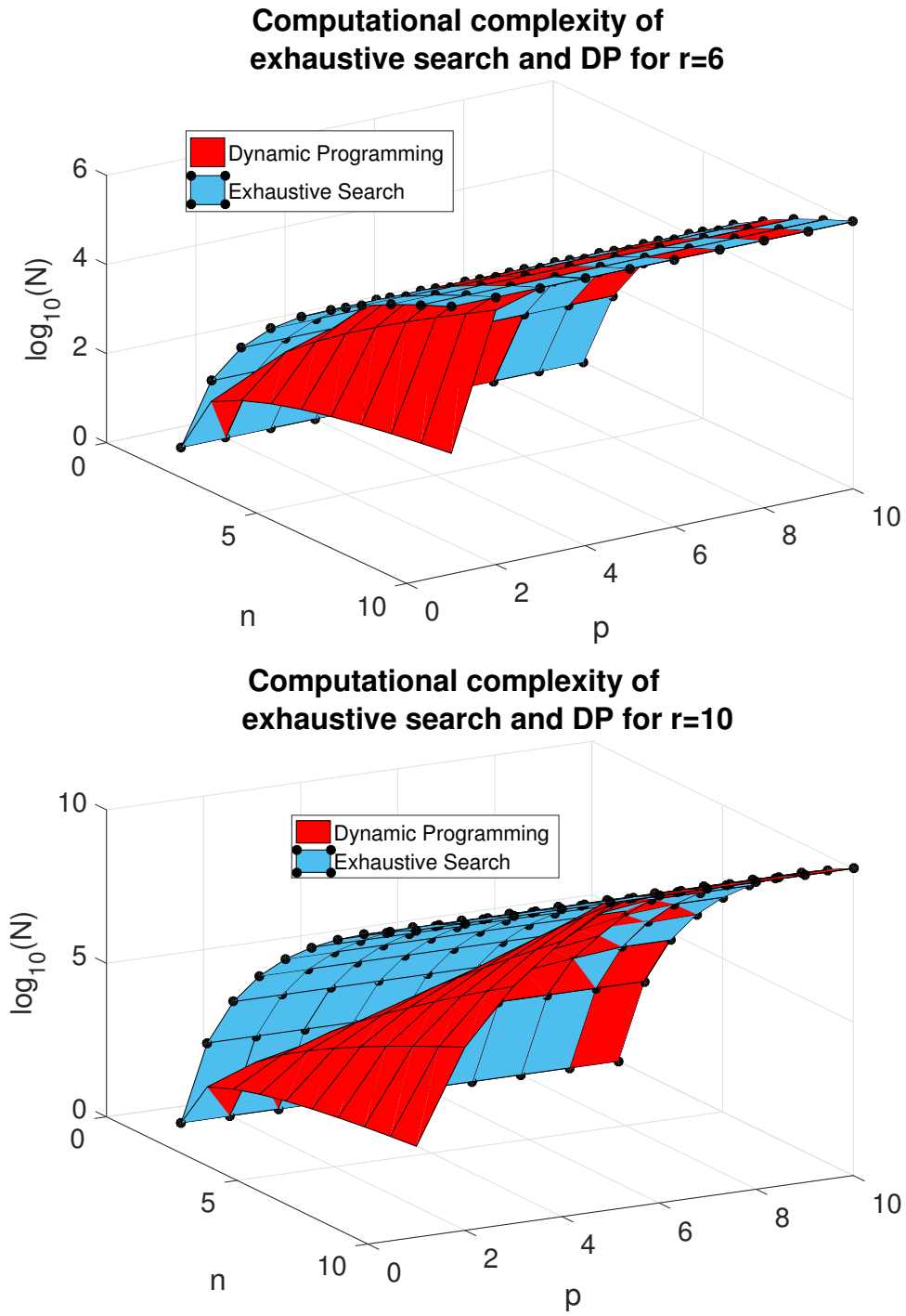

Figure 5.2: Comparison of the number of required function evaluation for an exhaustive grid search and dynamic programming (DP) for $r = 6$ (top) and $r = 10$ (bottom).

controller at the level below it.

5.2.1 MPC-LSES Hierarchical Controller

In the MPC-LSES hierarchical structure, a discrete-time optimization is performed at the upper level, while the middle level is a continuous controller. At the upper level, MPC, as described in Section 4.3, optimizes the altitude trajectory over the horizon length, using the cost formulation of (23).

At the middle level, LSES searches for the optimal altitude within the altitude bin determined by MPC before the upper level updates again. The wind velocity is measured at all visited altitudes, and this information is communicated back to the upper-level MPC for use at the next optimization step.

Fig. 5.3 shows the basic block diagram for the MPC-LSES hierarchical control structure, along with a demonstration of a sample output profile at each level. Note that the MPC optimization determines which bin to explore, whereas LSES explores locally within the chosen bin. The initial condition of the LSES integrator (see Fig. 4.2) is reset to z_{MPC} at the beginning of each upper-level sampling interval. Upper and lower saturation limits on $\hat{z}$ are set based on the bin width, Δ_{bin}, as follows:

$$\hat{z}_{\max} = z_{\mathrm{MPC}} + \frac{\Delta_{\mathrm{bin}}}{2} \tag{6}$$

$$\hat{z}_{\min} = z_{\mathrm{MPC}} - \frac{\Delta_{\mathrm{bin}}}{2} \tag{7}$$

In this work, the altitude domain is divided into 6 bins ($n_{\mathrm{up}} = 6$). MPC using an exhaustive grid search finds the optimized altitude trajectory as shown in Fig. 5.3 (b). The first element of this trajectory is bin no. 3. LSES as the mid-level controller searches within the third bin continuously to find the optimum.

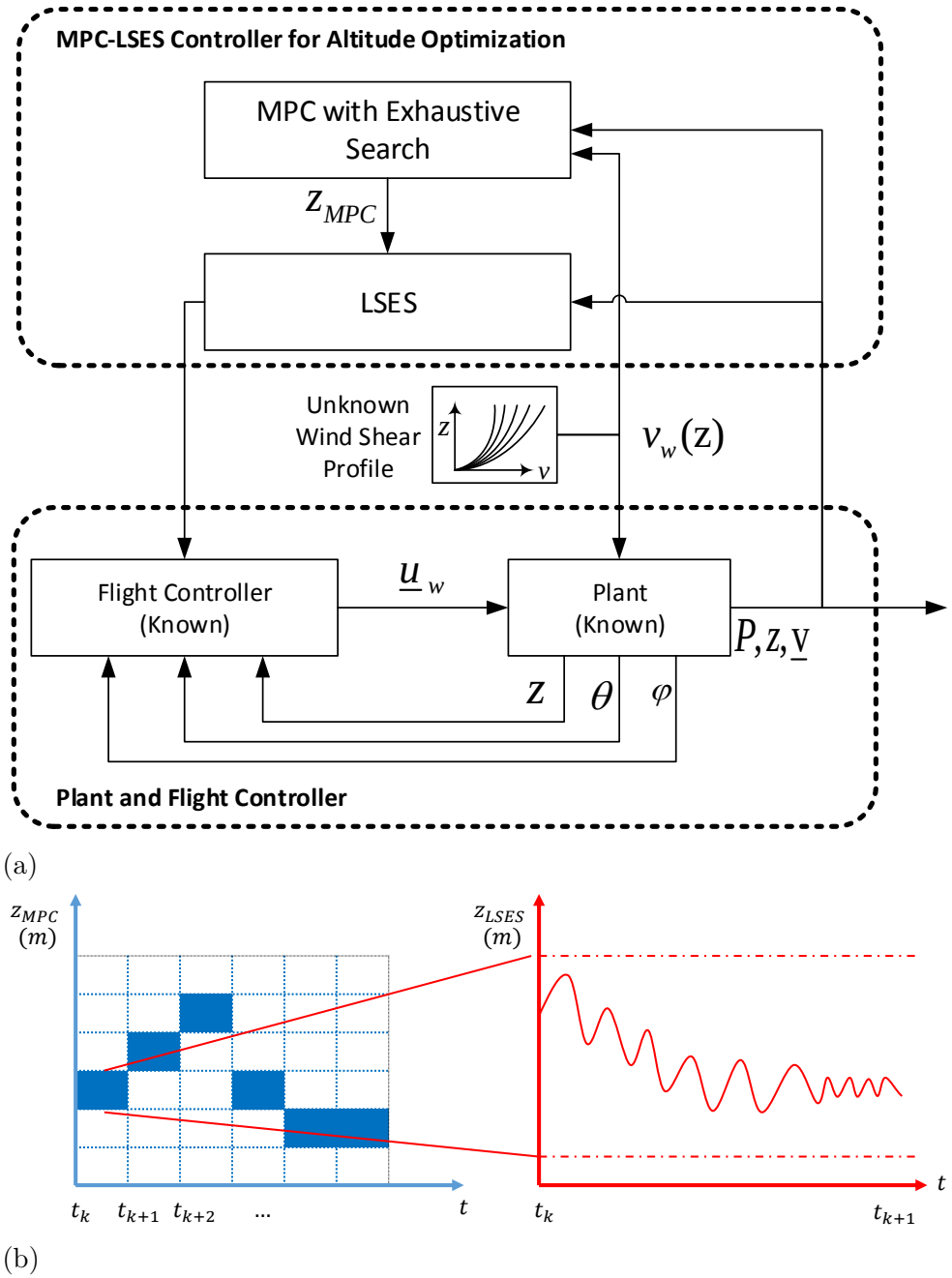

Figure 5.3: MPC-LSES hierarchical control structure for altitude optimization of AWE systems. (a) shows the block diagram for the MPC-LSES controller. A sample output profile at the two control levels is depicted in (b). The upper level (left) determines the altitude bin with estimated cost function, and the mid-level controller (right) searches within that bin for the optimum altitude using a continuous perturbation until the upper level prescribes the next set-point.

5.2.2 MPC-MPC Hierarchical Controller

Another option for the mid-level controller is to use MPC with a short horizon length and a localized search domain of allowable altitudes. The mid-level MPC quantizes the altitude bin prescribed by the upper level into a number of more finely quantized bins and uses a short-horizon exhaustive search to search for the optimal altitude. This reduces the computational complexity significantly, allowing for rapid updates to take place. Unlike MPC-LSES, the controller at both levels are implemented in discrete time. However, the quantization levels of altitude and horizon lengths at the two control levels are different.

The accessible altitude domain of the mid-level MPC is limited to the size of altitude bin quantized by the upper level MPC. The total time horizon of the mid-level is also equal to the time step of the upper level MPC. In the example shown in Fig. 5.4, the altitude quantization level for both control levels is 6 ($n_{\text{up}} = n_{\text{mid}} = 6$).

5.2.3 Globalized LSES

For general objective functions, extremum seeking only guarantees convergence to local optima. The possibility of modifying extremum seeking to be global in the presence of local extrema is studied in [89]. In particular, [89] proposes a method by which the perturbation amplitude can be adjusted to converge to a global optimum. In this third candidate hierarchical controller, this concept is used to globalize the mid-level extremum seeking. For this purpose, the mid-level controller uses a calculation of the surrogate power deficit from the upper level to adjust the level of perturbation used by LSES at the middle level. Specifically, the upper control level uses the conditional probability model of available power described in Subsection 3.1.2 to calculate the surrogate power deficit metric. The mid-level LSES uses this information to adjust the perturbation size, a_0, in order to avoid getting stuck in local optima. Therefore, the third controller is termed *Globalized LSES*.

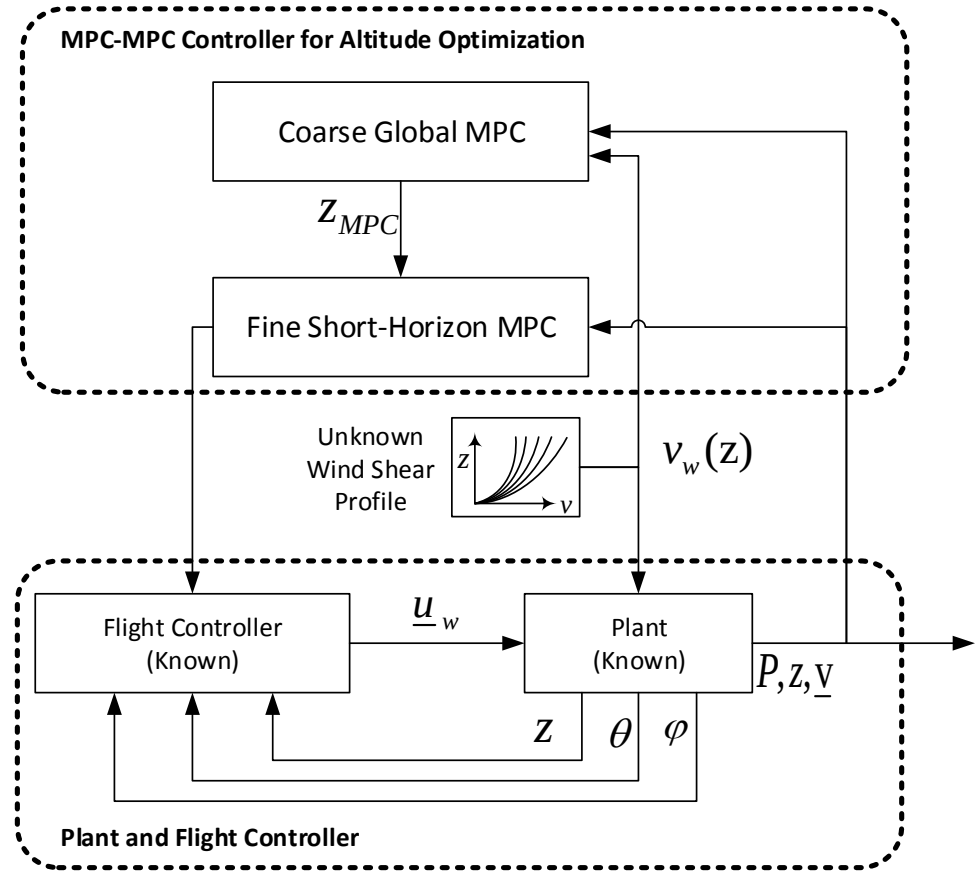

(a)

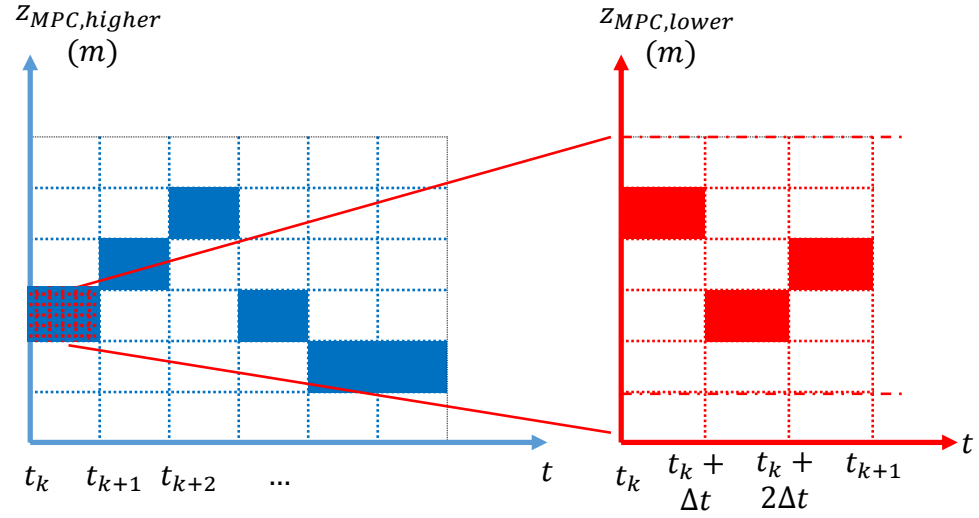

(b)

Figure 5.4: MPC-MPC hierarchical control structure. (a) shows the block diagram. (b) illustrates how mid-level MPC (right) quantizes the altitude bin selected by the upper level (left) to search for the optimum altitude in a short-horizon.

The surrogate power deficit metric introduced in Section 3.3.1 gives an estimate of how well the altitude controller is working. Large values of P_{sur} suggest that the controller is likely not operating near its globally optimal altitude, whereas smaller values suggest that it is. Therefore, the LSES perturbation amplitude (a_0 in Fig. 4.2 and Fig. 5.5) is chosen to be proportional to the surrogate power deficit metric. The perturbation frequency is modified based on the value of a_0. Fig. 5.5 shows the block diagram of the proposed globalized LSES controller, as well as a demonstration of how these two control levels are related. Specifically, perturbation amplitude a_0 is given by:

$$a_0 = \frac{P_{\text{sur}}}{P_{\text{sur,max}}} \left(w_a a_{\text{base}} - a_{\text{min}}\right) + a_{\text{min}} \tag{8}$$

where w_a is the maximum magnifying coefficient of the perturbation amplitude, a_{base} and a_{min} are the base and minimum perturbation amplitudes, respectively. $p_{\text{sur,max}}$ is the maximum value of the surrogate metric, which occurs when the current power production is zero and the power at all other altitude bins is equal to the rated power:

$$p_{\text{sur,max}} = (n_f - 1) p_{\text{rated}} \tag{9}$$

5.3 Results

Wind data obtained from [7] were used to simulate the AWE system under the aforementioned control structures. Simulations using the available real wind data provide a fair comparison of the performance of the proposed altitude optimization tools. Simulations were performed over 15 days in March 2014. Time steps for upper and mid-control levels in the MPC-MPC hierarchical structures were taken to be 30 min and 6 min, respectively. A time step of 30 minutes was used for standalone MPC controller, as well as the upper level MPC in MPC-LSES control structure. LSES as a standalone or mid-level controller is continuous. Tables 5.2, 5.3, 5.4,and 5.5 give

Table 5.2: AWE System Parameters

Parameter	Description	Value
v_{r}	Rated wind speed of the turbine	12 m/s
z_h	Maximum allowable altitude	1.04 km
z_l	Minimum allowable altitude	0.146 km
r_z	Rate of altitude change (in winch speed)	0.5 m/s
k_1	Coefficient of power production related to the power curve of the turbine	0.0579 $\frac{kWs^3}{m^3}$
k_2	Coefficient of power required to maintain altitude	0.09 $\frac{kWs^2}{m^2}$
k_3	Coefficient of power required to change altitude	1.08 $\frac{kWs^3}{m^3}$

the parameter values considered in simulations for AWE system, and LSES, MPC, and hierarchical controllers, respectively.

Six different control configurations, termed "scenarios" are compared in this section.

Scenario 1: Off-line Optimized Constant Altitude: This scenario involves flying the AWE system at a *constant altitude* that is determined by off-line calculation of available power at different altitudes using given wind data. It is worth noting that this calculation requires omniscient knowledge of wind velocity over all altitudes and times. It is therefore not practically implementable; we use this scenario to provide an upper bound on the potential of any constant altitude algorithm.

Scenario 2: Standalone MPC: The second controller employs MPC alone to find

Table 5.3: LSES Parameters

Parameter	Description	Value	Unit
k	Integrator gain	$3e-5$	kW/m
a	Perturbation magnitude	10	m
$a_{\min}$	Minimum perturbation magnitude	1	m
ω	Perturbation frequency	0.0262	rad/sec
ω_H	High-pass filter (washout filter) frequency	0.0236	rad/sec
ω_L	Low-pass filter frequency	0.0024	rad/sec
ϵ	Switching threshold	$1e-9$	-

Table 5.4: MPC Parameters

Parameter	Description	Value
w	Exploration weight	1
w_1	Energy consumption weight	10 m
m_0	Constant 1 in conditional standard deviation model	1
m_1	Constant 2 in conditional standard deviation model	0.0052
m_2	Constant 3 in conditional standard deviation model	0.5102

the optimum altitude. The altitude of the AWE system is adjusted when the MPC updates and is constant for the upper-level time step specified in Table 5.5. As discussed in Section 4.3, the exploitation term in the cost function includes the surrogate power deficit metric introduced in Section 3.3.1. The parameters used in the simulation are shown in Table 5.4. The altitude is quantized into 10 bins ($n_{\text{up}} = 10$), and the time step is 30 minutes ($t_{\text{up}} = 30$ mins).

Scenario 3: Lyapunov-Based Switched Extremum Seeking Control: The third scenario is LSES-based altitude optimization alone as introduced in Section 4.1, which

Table 5.5: Hierarchical Control Architecture Parameters

Parameter	Description	Value
$t_{\mathbf{up}}$	Upper level time step	30 min
$t_{\mathbf{mid}}$	Mid-level time step	6 min
$n_{\mathbf{up}}$	Upper level altitude quantization level	10
$n_{\mathbf{mid}}$	Mid-level altitude quantization level	9

curtails the size of the ES perturbation signal to minimize energy consumption once an optimal power generation point has been reached. Table 5.3 gives the values for LSES parameters.

Scenario 4: MPC-LSES Hierarchical Controller: This control structure employs MPC and LSES controllers as higher and mid-level controls, respectively, in a hierarchical structure conforming to Fig. 5.3. MPC at the upper level provides the mid-level with an estimate of the neighborhood of the optimal altitude. LSES then searches for the optimal altitude within that neighborhood. The parameters for the upper-level MPC and mid-level LSES are shown in Table 5.4 and 5.3, respectively. As shown in Table 5.5, the time step for the upper-level MPC is 30 minutes ($t_{\text{up}} = 30$ mins) and the altitude quantization level for MPC is 10 minutes ($n_{\text{up}} = 10$).

Scenario 5: MPC-MPC Hierarchical Controller: In this scenario, a global coarse MPC is used in the upper level, while the mid-control uses a short-horizon fine-grid MPC, as depicted in Fig. 5.4. As with scenario 4, the upper-level MPC uses a global optimization over a coarse grid to find the optimal altitude bin. The mid-level MPC searches within the prescribed bin for the optimum. Table 5.4 gives the common parameters for MPC in both levels, and Table 5.5 shows the values of specific parameters for each control level.

Scenario 6: Globalized LSES: The globalized LSES control scheme as shown in Fig.

5.5, uses the conditional probability model of power to modify the size of the LSES perturbation when it detects that the LSES controller is likely to be stuck in a local optimum.

Key Results and Interpretations: The cumulative energy yield of the six control scenarios are compared in Fig. 5.6 and summarized in Table 5.6. This figure and the table clearly show that globalized LSES outperforms the other scenarios in terms of net energy generation. In light of the results obtained, several explanations for the superior performance of globalized LSES exist:

1. Extremum seeking is a continuous optimal control technique. Therefore, the hierarchical structures based on LSES are capable of faster response to changes in the wind shear profile.

2. The MPC-LSES control architecture requires the extremum seeking integrator to be reset every time that a new altitude bin is commanded by the upper level MPC algorithm. Because the convergence of extremum seeking is limited by its corresponding perturbation frequencies and filter time constants (which are limited by the dynamics of the system), the convergence of LSES will, in many cases, be slow, relative to the upper level time step. In these cases, it will not be possible for LSES to converge to the optimal altitude before its integrator is reset.

3. The MPC-MPC control architecture places limitations on what the mid-level controller is allowed to do. In particular, the mid-level MPC may only explore within the altitude bin prescribed by the upper level MPC.

Table 5.6 shows that the hierarchical strategies, which fuse local and global tools, outperform their coarse-global only and fine-local only counterparts. In particular, this table shows that globalized LSES is superior in energy production compared to other scenarios. This is mainly because historical wind data is introduced to an

Table 5.6: Total Energy Production of a 100 kW AWE System Under Different Control Scenarios

No.	Controller	Energy Production
1	Off-line Optimized Constant Altitude	39.68 MWh
2	Standalone LSES	37.66 MWh
3	Standalone MPC	39.15 MWh
4	MPC-LSES	40.04 MWh
5	MPC-MPC	38.69 MWh
6	Globalized LSES	43.27 MWh

originally model-free, gradient based algorithm. This helps the LSES to find the *global* optimum. The second best performing algorithm is MPC-LSES. Putting LSES as the mid-level control results in greater energy production than using MPC for the mid-level controller.

The altitude trajectory and wind velocity at the operating altitude of the AWE system under different control scenarios are shown in Figs. 5.7 and 5.8, respectively. These plots show that the wind velocity of the AWE system with globalized LSES aligns more closely with the rated wind speed of the turbine. Moreover, the globalized LSES controller results in a significantly lower power deficit, compared to other control scenarios, most of the time.

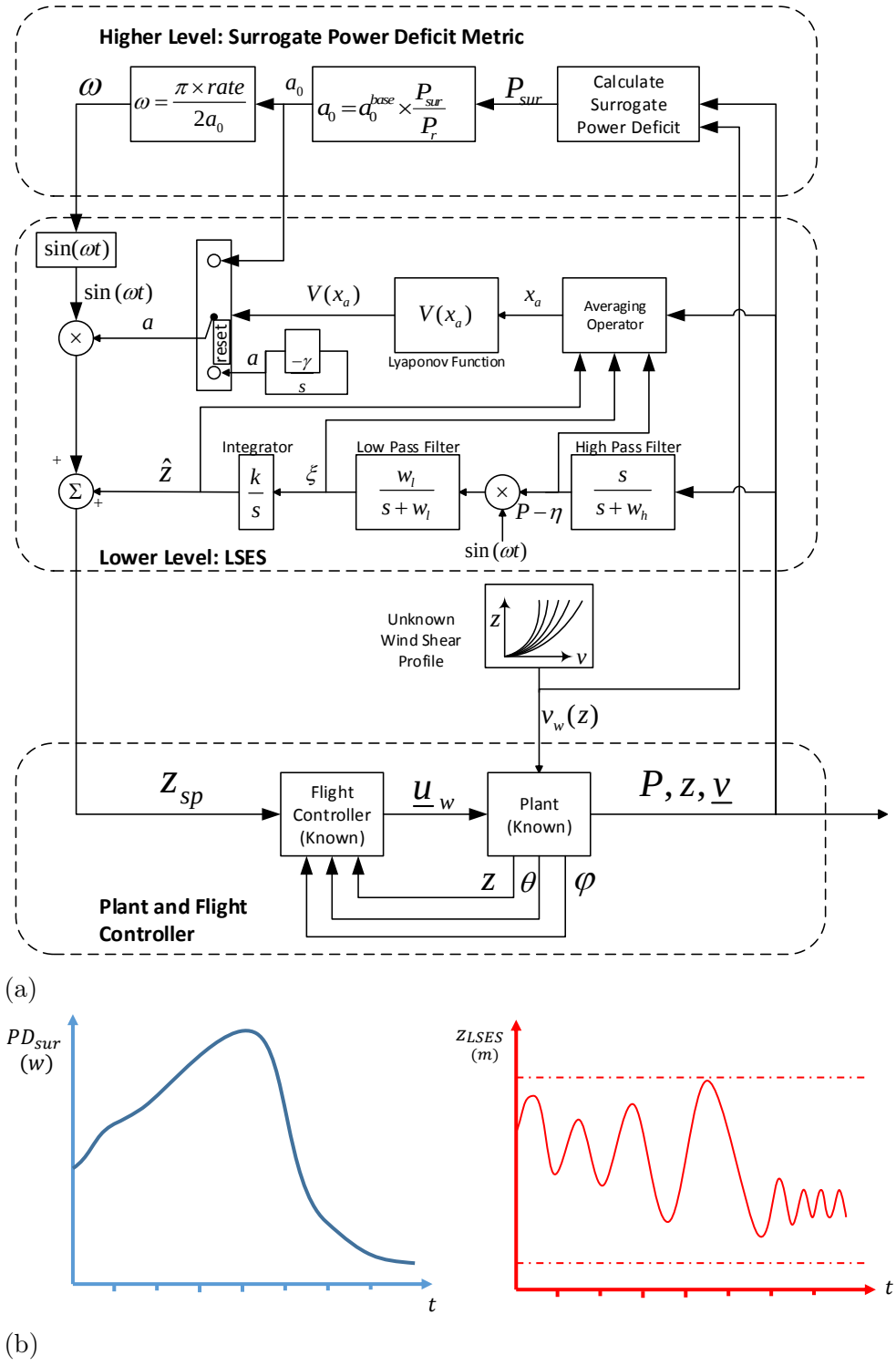

Figure 5.5: Globalized LSES hierarchical control structure. (a) shows the block diagram and (b) illustrates how the top level calculation and LSES are correlated. The top level performs a statistical characterization of available power to calculate the surrogate power deficit metric. The mid-level controller is LSES, whose maximum perturbation size is adjusted using information from the upper level. Specifically, when the value of the surrogate metric increases, the perturbation amplitude is increased.

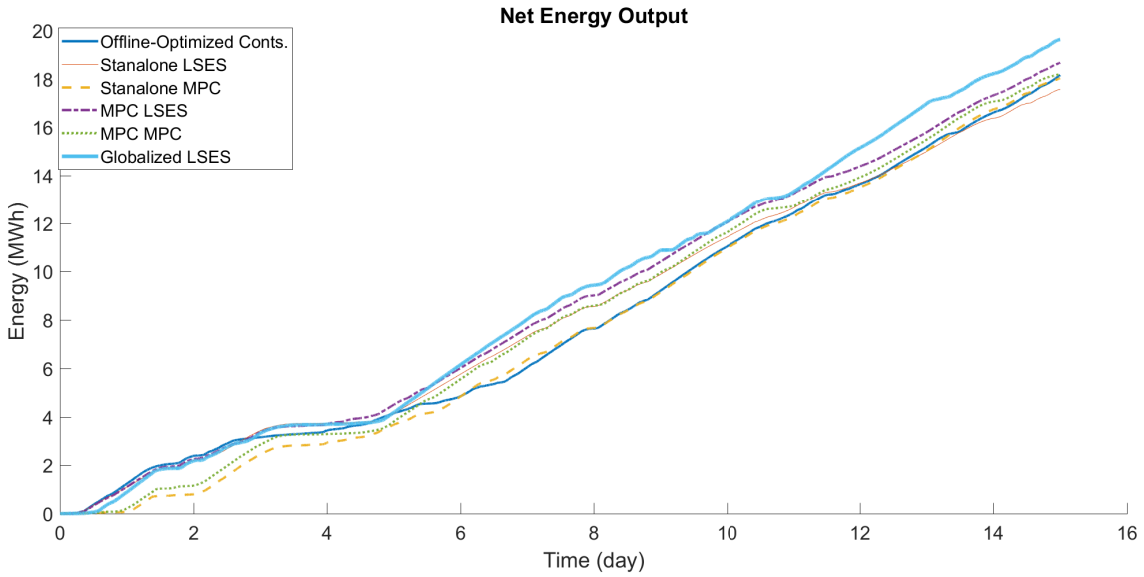

Figure 5.6: Comparison of cumulative net energy generation for simulating AWE system operation with 6 proposed control scenarios.

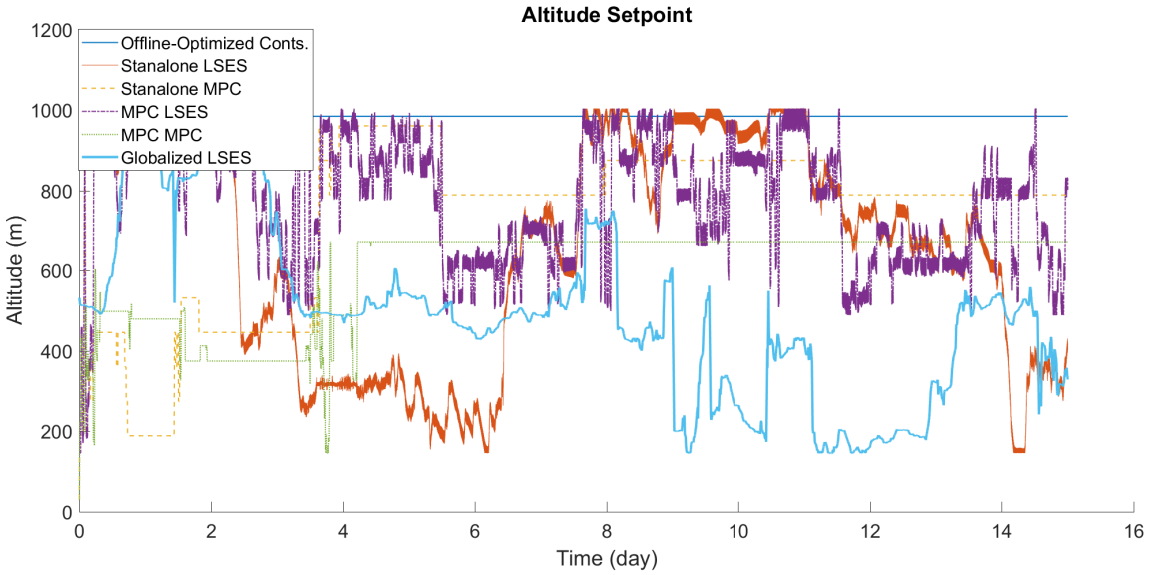

Figure 5.7: Altitude trajectory of the AWE system with 6 proposed control scenarios.

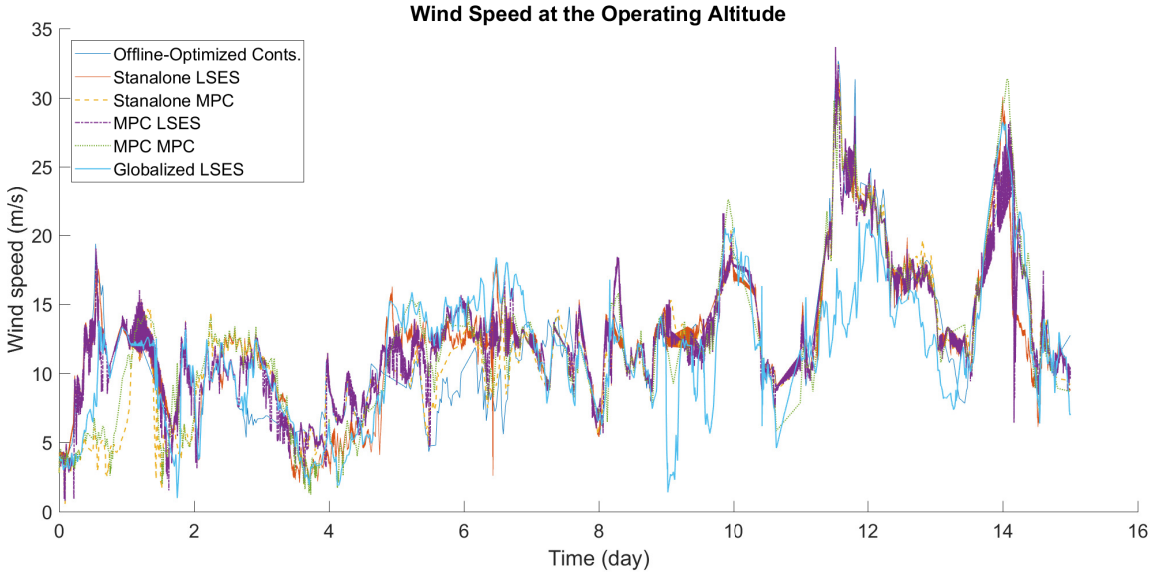

Figure 5.8: Wind velocity at operating altitude of AWE system with 6 proposed control scenarios.

CHAPTER 6: Hierarchical Control Structures for Altitude Optimization of Integrated AWE Systems

The candidate controllers developed in previous chapters have been validated only on a stand-alone AWE system (without an integrated dispatchable power source and energy storage system). Even [90] merely evaluates the economic performance of an idealized AWE-battery-generator system but still bases its optimization solely on the power output of the turbine alone.

The integrated AWE system considered in this dissertation consists of a $100kW$ wind turbine and a $80kW - hr$ battery storage system. According to the energy generation model introduced in Section 2.1, a part of power generated by the wind turbine is consumed in rejecting the disturbances under typical levels of turbulence in order to maintain the operating altitude at its altitude setpoint. Consequently, the maximum output power of AWE system is $87kW$. The battery was sized such that it can address the average load for two hours.

An integrated AWE-generator-battery system is studied in [8] and is illustrated in Fig. 6.1. Because the results of Chapter 5 identified GLSES as the leading candidate hierarchical strategy, this chapter will focus on several formulations of GLSES for the purpose of minimizing generator energy consumption in the integrated system. Specifically, several candidate hierarchical GLSES control formulations, each conforming to the general structure of Fig. 6.2, will be described and evaluated. These candidate structures consist of :

1. An upper-level controller that calculates auxiliary generator and battery setpoints, as well as the amplitude of perturbation signal to be used in the mid-level extremum seeking for altitude control, based on the surrogate generator

excess metric.

2. A mid-level controller that uses LSES scheme for adjusting the operating altitude set-point of the AWE system;

3. A lower-level flight controller that tracks the altitude set point dictated by the middle level. Because lower-level flight controllers have already been developed and validated in the literature (see [44]), this work focuses on the upper- and mid- level controllers.

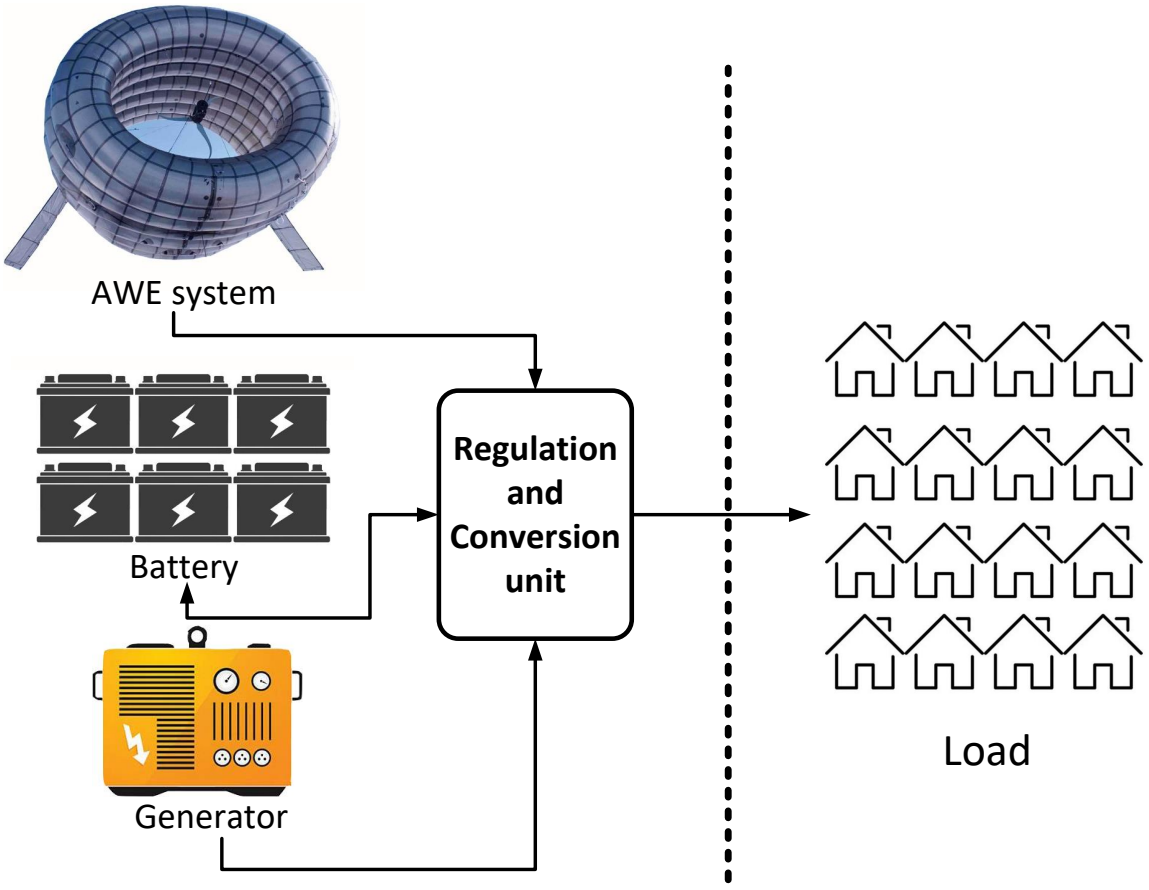

Figure 6.1: Schematic of an integrated AWE system, including the airborne turbine (here Altaeros BAT [6]), battery, and auxiliary generator ([8]).

6.1 Requirements for Designing a Controller for an Integrated AWE System

This section reviews the requirements for designing the hierarchical control structure for integrated AWE-battery-generator system. first, adjustment of the pertur-

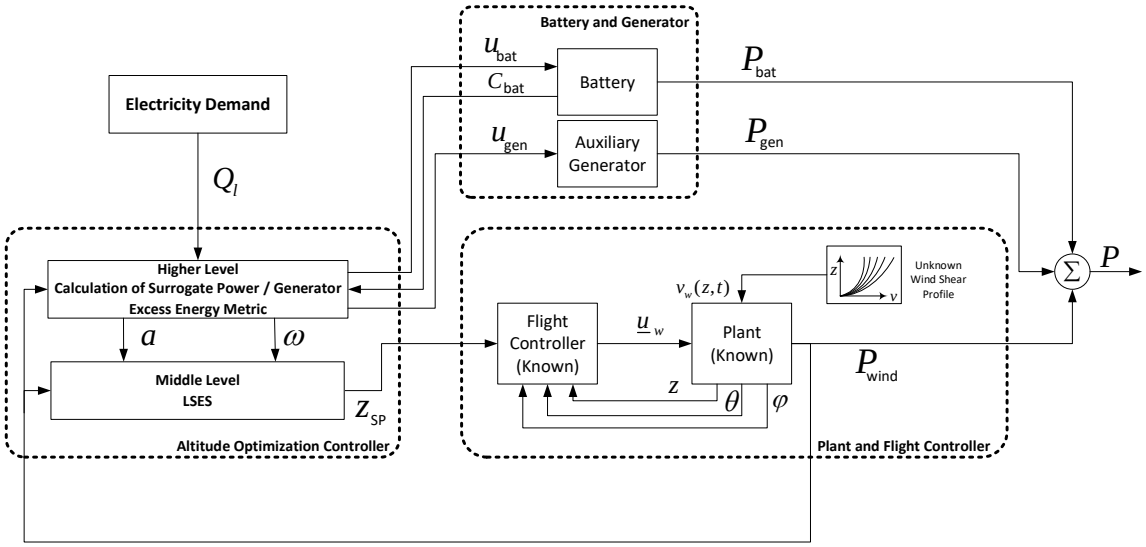

Figure 6.2: Basic block diagram of GLSES controller for altitude optimization of an integrated AWE system ([8]).

bation amplitude of the LSES in middle level controller, using the surrogate metric information from the upper level, is described. Then, the calculation of battery and generator setpoints are reviewed.

6.1.1 The Adjustment of LSES Perturbation Using Surrogate Metric from the Upper Level

The surrogate generator excess metric introduced in Section 3.3.2 gives an estimate of how much better the altitude controller can work if another altitude setpoint were chosen. Large values of M_{sur} suggest that the controller is likely not operating near its globally optimal altitude, whereas smaller values suggest that it is. Therefore, the LSES perturbation amplitude (a_0 in Fig. 4.2 and Fig. 6.2) is chosen to be proportional to the surrogate generator excess metric. The perturbation frequency is modified based on the value of a_0. Fig. 6.2 shows the block diagram of the proposed globalized LSES controller, as well as a demonstration of how these two control levels are related. Specifically, perturbation amplitude a_0 is given by:

$$a_0 = \frac{M_{\text{sur}}}{M_{\text{sur,max}}} \left(w_a a_{\text{base}} - a_{\text{min}}\right) + a_{\text{min}} \tag{1}$$

where w_a is the maximum magnifying coefficient of the perturbation amplitude, a_{base} and a_{min} are the base and minimum perturbation amplitudes, respectively. $M_{\text{sur,max}}$ is the maximum value of the surrogate metric, which occurs when the current generator excess is equal to the maximum electricity demand, and the generator excess energy at all other altitude bins is zero:

$$M_{\text{sur,max}} = (n_f - 1) Q_{l,\text{max}} \Delta t \tag{2}$$

6.1.2 Battery and Generator Setpoints

The battery state of charge at the next time step, as detailed in Section 2.2, is given by:

$$C_{\mathbf{b}}(k+1) = \begin{cases} C_{\mathbf{b}}(k) - \frac{1}{\eta_{bat}} E_{\mathbf{bat}}(k), & E_{\mathbf{bat}}(k) > 0 \\ C_{\mathbf{b}}(k) - \eta_{bat} E_{\mathbf{bat}}(k), & \text{otherwise.} \end{cases} \tag{3}$$

where η_{bat} is the charging/discharging efficiency of the battery, and $E_{\mathbf{bat}}(k)$ is the amount of energy discharged from the battery:

$$E_{\mathbf{bat}}(k) = \begin{cases} \eta_{bat} C_{\mathbf{b}}(k), & E_{\mathbf{d}}(k) > \eta_{bat} C_{\mathbf{b}}(k) \\ \frac{1}{\eta_{bat}} (C_{\mathbf{b}}(k) - C_{\mathbf{max}}), & E_{\mathbf{d}}(k) < \frac{1}{\eta_{bat}} (C_{\mathbf{b}}(k) - C_{\mathbf{max}}) \\ E_{\mathbf{d}}(k), & \text{otherwise} \end{cases} \tag{4}$$

and the generator energy setpoint is given by:

$$E_{\mathbf{gen}}(k) = \max\{0, E_{\mathbf{d}}(k) - E_{\mathbf{bat}}(k)\} \tag{5}$$

6.2 Results

We simulated the integrated AWE system controller for different combinations of objective functions at top and mid-level controllers. These controllers are based on a GLSES hierarchical control structure. In one candidate, the calculation of surrogate generator excess metric in upper level is performed for a receding horizon using load forecast. The real wind and electricity demand data used in simulations are obtained from [7] and PJM, respectively. The simulations have been performed for the period of March 2014 (31 days). The values of parameters used in simulations are given in Tables 6.1 and 6.2.

Table 6.1: AWE System Parameters

Parameter	Description	Value	Unit
total time	Individual simulation period	31	days
v_{r}	Turbine rated wind speed	12	m/s
z_h	Max. allowable altitude	1040	m
z_l	Min. allowable altitude	146	m
r_z	Max. rate of altitude change	0.3	m/s
k_1	Coefficient of power production of the turbine	0.0579	$\frac{kWs^3}{m^3}$
k_2	Coefficient of power required to change altitude	0.09	$\frac{kWs^2}{m^2}$
k_3	Coefficient of power required to maintain altitude	1.08	$\frac{kWs^3}{m^3}$

Table 6.3 shows the optimum weights for individual forecasts in the combined load forecast model at each time step. The MAPE of the 13 individual candidate forecasts in addition to the combined forecast model, are given in Table 6.4

To assess the performance of the GLSES and compare it to several benchmarks, eight different control scenarios are simulated in this work. Five controllers are based on the GLSES structure, two scenarios are based on stand-alone LSES, and one omniscient scenario assumes that the wind velocity data is available for all altitudes over the simulation time.

Scenario 1: Globalized LSES with Generator Set-point at Upper and Wind Power

Table 6.2: LSES Parameters

Parameter	Description	Value	Unit
k_{wind}	Integrator gain when the objective is to maximize the net power	$3e-5$	kW/m
k_{gen}	Integrator gain when the objective is to minimize the generator power	$-5e-7$	kW/m
a	Perturbation magnitude	10	m
$a_{\min}$	Minimum perturbation magnitude	5	m
ω	Perturbation frequency	0.0262	rad/sec
ω_H	High-pass filter (washout filter) frequency	0.0236	rad/sec
ω_L	Low-pass filter frequency	0.0024	rad/sec
ϵ	Switching threshold	$1e-9$	-
N	Horizon length for forecast-based GLSES	4	-

Table 6.3: Optimum Weights in Combined Forecast Model

Forecasting model	Step 1	Step 2	Step 3	Step 4
ARIMA10	0.1267	0.0758	0.0599	0.0560
ARIMA6	0.5514	0.4495	0.3324	0.2371
LinReg00	0.0297	0.0422	0.0498	0.0632
LinReg01	0.0288	0.0435	0.0517	0.0652
LinReg02	0.0289	0.0412	0.0651	0.0600
LinReg10	0.0270	0.0316	0.0413	0.0539
LinReg11	0.0279	0.0435	0.0475	0.0625
LinReg12	0.0285	0.0443	0.0658	0.0735
LinReg20	0.0274	0.0400	0.0479	0.0636
LinReg21	0.0335	0.0454	0.0661	0.0789
LinReg22	0.0313	0.0508	0.0592	0.0617
2NN	0.0319	0.0508	0.0638	0.0701
8NN	0.0270	0.0413	0.0494	0.0543

at Lower Control Level (GLSES Gen - Wind): This is a hierarchical GLSES controller where the objective function at the upper level is the instantaneous generator power (to be minimized), whereas the lower level objective function is the instantaneous wind power output (to be maximized).

Scenario 2: Globalized LSES with Generator Set-point at Upper and Wind Power

Table 6.4: Comparison of MAPE for Combined and 13 individual Forecasting Models

Forecasting Model	MAPE
ARIMA10	0.0855
ARIMA6	0.0556
LinReg00	0.0810
LinReg01	0.0731
LinReg02	0.0710
LinReg10	0.0787
LinReg11	0.0718
LinReg12	0.0707
LinReg20	0.0745
LinReg21	0.0697
LinReg22	0.0710
2NN	0.0707
8NN	0.0602
Combined Model	0.0419

at Lower Control Level (GLSES Gen - Wind with forecast): This is a hierarchical GLSES controller where the objective function at the upper level is the instantaneous generator power (to be minimized), whereas the lower level objective function is the instantaneous wind power output (to be maximized). In this scenario, load forecasting is used to calculate the surrogate generator excess metric over a horizon.

Scenario 3: Globalized LSES with Wind Power at Both Levels (GLSES Wind - Wind): This controller is a hierarchical GLSES controller wherein the objective function at both levels is the instantaneous wind power output of the system.

Scenario 4: Globalized LSES with Wind Power at Upper and Generator Set-point at Lower Control Level (GLSES Wind - Gen): This is a hierarchical GLSES controller where the objective function at the upper level is the instantaneous power output of the AWE system, whereas the lower level objective function is the instantaneous generator power.

Scenario 5: Globalized LSES with Generator Set-point at Both Levels (GLSES Gen - Gen): This is a hierarchical GLSES controller where the objective function at both

levels is the instantaneous generator power (to be minimized).

Scenario 6: LSES Standalone with Wind Power (LSES Standalone Wind): This controller is a single level LSES (with no upper-level controller to adjust the extremum seeking perturbation size), where the objective function (to be maximized) is equal to the instantaneous power output of the AWE system.

Scenario 7: LSES Standalone with Generator Set-point (LSES Standalone Gen): This controller is a single level LSES (with no upper-level controller to adjust the extremum seeking perturbation size), where the objective function (to be minimized) is the instantaneous generator power set-point of the AWE system.

Scenario 8: Upper Bound: In this scenario, it is assumed that we have access to omniscient knowledge of wind velocity over all altitudes at all times, including the future, which is not available during the operation of a real AWE system. However, this scenario gives an upper bound to compare other results against.

For the control scenarios considered in this work, Table 6.5 shows the controller options for the upper and middle levels.

Simulation results under the 8 control scenarios are shown in Figs. 6.3, 6.4, 6.5, and 6.6. The actual generator excess energy is plotted in Fig. 6.3. This figure shows that incorporating load forecasting to the GLSES Gen-Wind controller significantly reduces the energy required by the generator. This arises mainly because the AWE system is encouraged to explore more than other scenarios when there is no need to use generator to address the electricity demand, as inferred from Figs. 3.7 and 6.5. In other words, the predicted future trend of the electricity demand is considered in balancing exploration and exploitation. Therefore, exploration is incentivized when the electricity demand is expected to increase in the coming time steps.

Table 6.5: Controller Choice for Each Level of Candidate Hierarchical Structures

Scenario	Candidate Structure	Upper level	Mid-level
1	GLSES Gen-Wind	Calculation of M_{sur} for a single step	LSES to maximize power
2	GLSES Gen-Wind with Forecast	Calculation of M_{sur} for multi-step with load forecasting	LSES to maximize power
3	GLSES Wind-Wind	Calculation of P_{sur}	LSES to maximize power
4	GLSES Wind-Gen	Calculation of P_{sur}	LSES to minimize generator expenditure
5	GLSES Gen-Gen	Calculation of M_{sur}	LSES to minimize generator expenditure
6	LSES Standalone Wind	-	LSES to maximize power
7	LSES Standalone Gen	-	LSES to minimize generator expenditure
8	Upper Bound	-	Omniscient optimization

Table 6.6: Generator Energy Expenditure and Net Energy Generation for 8 Control Scenarios

Scenario Number	Candidate Structure	Generator Expenditure Energy (MWh)	Net Energy Output (MWh)
1	GLSES Gen - Wind	5.355	46.85
2	GLSES Gen - Wind with Forecast	4.731	48.53
3	GLSES Wind - Wind	6.695	43.27
4	GLSES Wind - Gen	7.705	41.48
5	GLSES Gen - Gen	7.413	40.44
6	LSES Standalone Wind	7.607	40.48
7	LSES Standalone Gen	6.871	40.27
8	Upper Bound	3.634	51.78

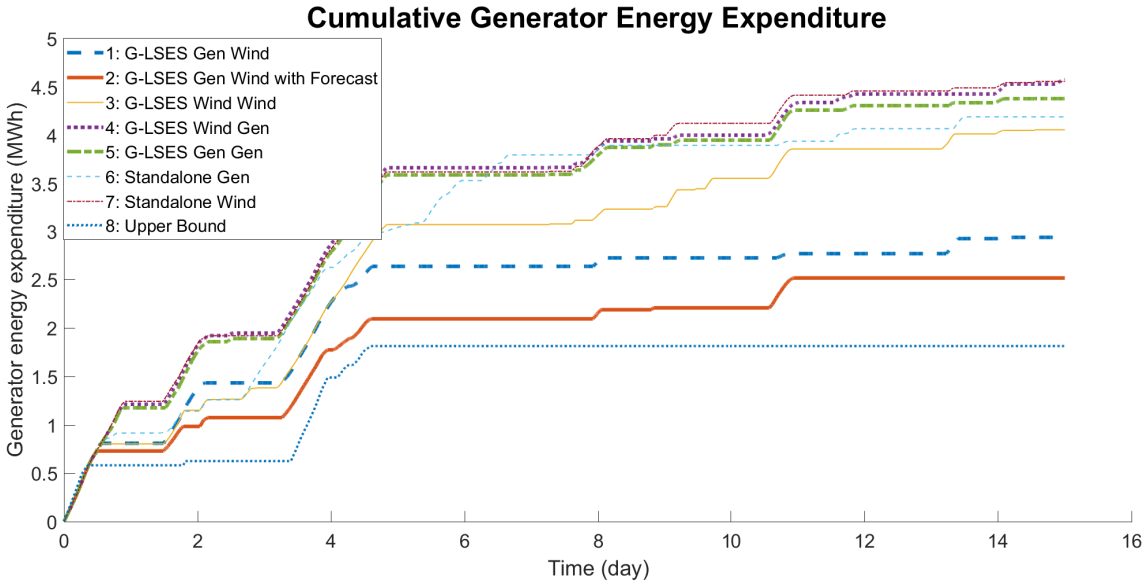

Figure 6.3: Generator excess energy set-point for 8 control scenarios. Note that it is preferred to *minimize* the generator excess energy.

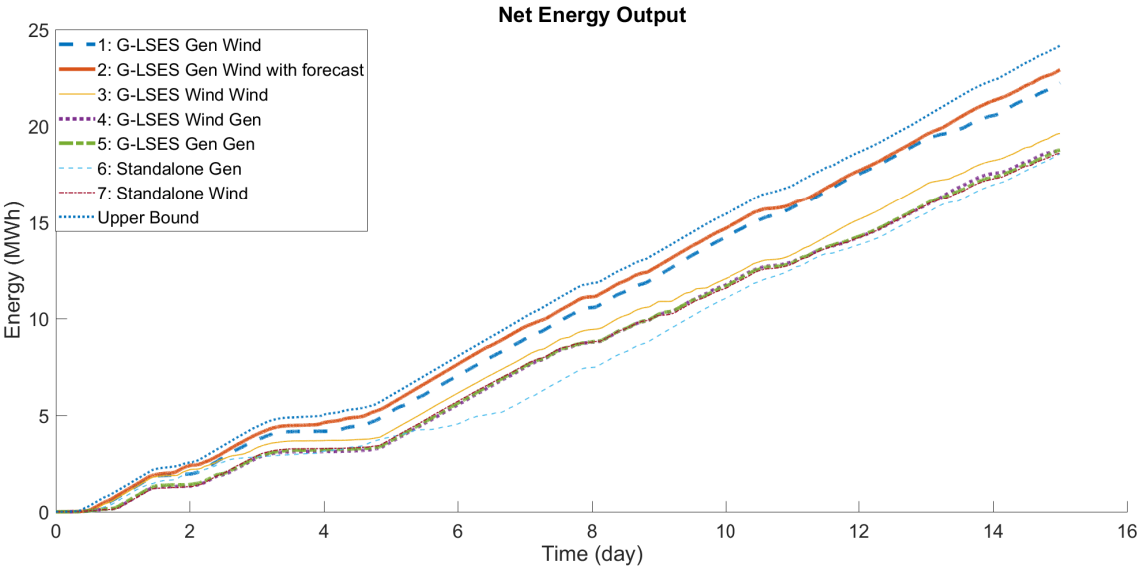

Figure 6.4: Net energy generation for 8 control scenarios.

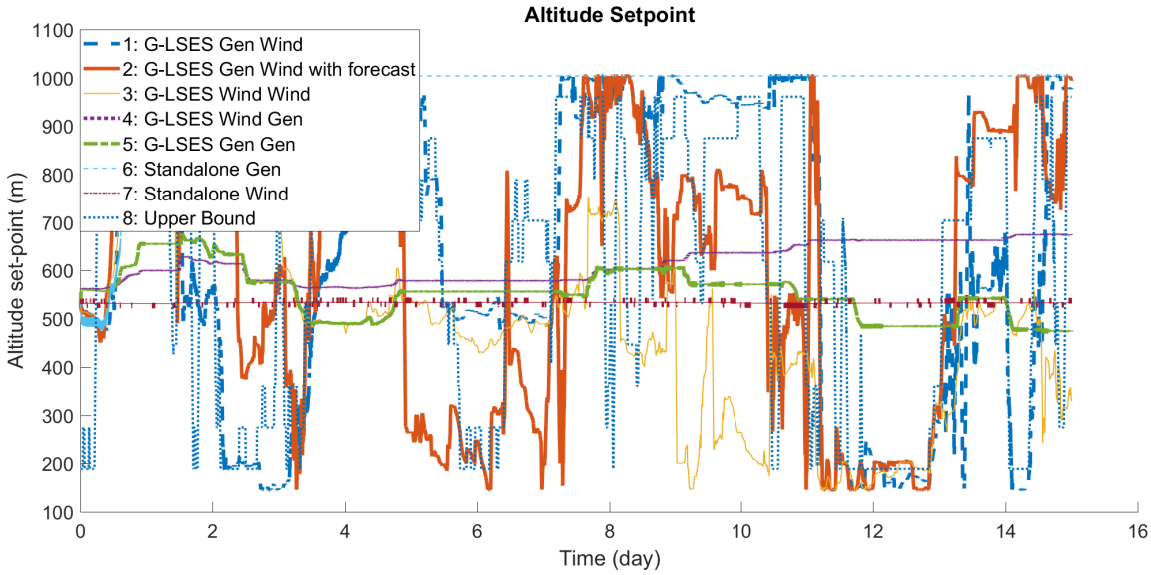

Figure 6.5: Altitude set-point trajectory for 8 control scenarios.

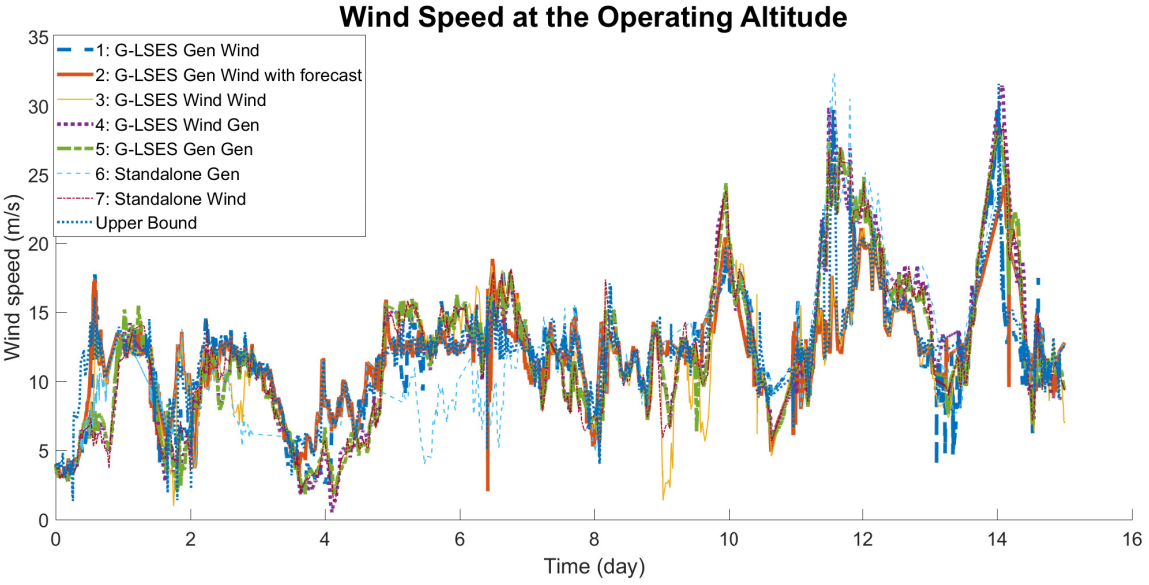

Figure 6.6: Wind velocity at the operating altitude for 8 control scenarios.

Bibliography

[1] US Department of Energy. Office of Energy Efficiency and Renewable Energies, http://energy.gov/eere/wind/inside-wind-turbine-0.

[2] International Renewable Energy Agency. Renewable Energy Technologies, Cost Analysis Series, 2012. Report, International Renewable Energy Agency, 2012.

[3] Joby Energy Inc. Joby Energy Inc. , Images extracted from https://inhabitat.com/high-flying-turbines-could-tap-870-terawatts-of-wind-power/.

[4] Antonello Cherubini, Andrea Papini, Rocco Vertechy, and Marco Fontana. Airborne wind energy systems: A review of the technologies. *Renewable and Sustainable Energy Reviews*, 51:1461–1476, 2015.

[5] Makani Power (now part of Google-X) Website. http://www.makanipower.com/.

[6] Altaeros Energies Website. http://www.altaerosenergies.com/.

[7] Cristina Archer. Wind Profiler At Cape Henlopen, Lewes, Delaware , http://www.ceoe.udel.edu/our-people/profiles/carcher/fsmw, 2014. Report, University of Delaware.

[8] Alireza Bafandeh and Chris Vermillion. Optimal altitude control of an integrated airborne wind energy system with globalized lyapunov-based switched extremum seeking. In *European Control Conference (ECC), 2018*, Limassol, Cyprus, 2018. IEEE.

[9] Shamir Bin-Karim, Alireza Bafandeh, and Chris Vermillion. Spatio-temporal optimization through model predictive control: A case study in airborne wind energy. In *2016 IEEE 55th Conference on Decision and Control (CDC)*, Las Vegas, NV, 2016.

[10] U.S. Energy Information Administration. Electric Power Monthly Report, January 2016.

[11] American Wind Energy Association. U.S. Wind Industry Fourth Quarter 2014 Market Report. Report, American Wind Energy Association, 2015.

[12] Colm O'Gairbhith. Assessing the viability of high altitude wind Resources in Ireland. *Paper, Loughborough University*, 2009.

[13] Miles L Loyd. Crosswind kite power (for large-scale wind power production).

Journal of Energy, 4(3):106–111, 1980.

[14] Sky Windpower Company Website. http://www.skywindpower.com/.

[15] Ampyx Power Website. http://www.ampyxpower.com/.

[16] KITEnrg Website. http://www.kitenergy.net/.

[17] Windlift Website. http://www.windlift.com/.

[18] KiteGen. Kitegen websit, http://www.kitegen.com/.

[19] Massimo Canale, Lorenzo Fagiano, M Ippolito, and M Milanese. Control of tethered airfoils for a new class of wind energy generator. In *45th IEEE Conference on Decision and Control, 2006*, pages 4020–4026, San Diego, CA, 2006.

[20] Massimo Canale, Lorenzo Fagiano, and Mario Milanese. Kitegen: A revolution in wind energy generation. *Energy*, 34(3):355–361, 2009.

[21] Massimo Canale, Lorenzo Fagiano, and Mario Milanese. Power kites for wind energy generation. *IEEE Control Systems Magazine*, 27(6):25–38, 2007.

[22] Lorenzo Fagiano, Mario Milanese, and Dario Piga. Optimization of airborne wind energy generators. *International Journal of Robust and Nonlinear Control*, 22(18):2055–2083, 2012.

[23] Sebastien Gros, Mario Zanon, and Moritz Diehl. A relaxation strategy for the optimization of airborne wind energy systems. In *2013 European Control Conference (ECC)*, pages 1011–1016. IEEE, 2013.

[24] Aldo U Zgraggen, Lorenzo Fagiano, and Manfred Morari. Real-time optimization and adaptation of the crosswind flight of tethered wings for airborne wind energy. *IEEE Transactions on Control Systems Technology*, 23(2):434–448, 2015.

[25] Aldo U Zgraggen, Lorenzo Fagiano, and Manfred Morari. On real-time optimization of airborne wind energy generators. In *52nd Annual Conference on Decision and Control (CDC), 2013*, pages 385–390, Firenze, Italy, 2013. IEEE.

[26] Mitchell Cobb, Kira Barton, Hosam Fathy, and Chris Vermillion. Iterative learning-based waypoint optimization for repetitive path planning, with application to airborne wind energy systems. In *2017 IEEE 56th Conference on Decision and Control (CDC)*, Melbourne, Australia, 2017.

[27] Parvin Nikpoorparizi, Nihar Deodhar, and Christopher Vermillion. Modeling, control design, and combined plant/controller optimization for an energy-harvesting tethered wing. *IEEE Transactions on Control Systems Technology*, pages 1–13., 2017.

[28] Nihar Deodhar, Alireza Bafandeh, Joe Deese, Brian Smith, Tim Muyimbwa,

Christopher Vermillion, and Peter Tkacik. Laboratory-scale flight characterization of a multitethered aerostat for wind energy generation. *AIAA Journal*, 55(6):1823–1832, 2017.

[29] Mitchell Cobb, Nihar Deodhar, and Christopher Vermillion. Lab-scale experimental characterization and dynamic scaling assessment for closed-loop crosswind flight of airborne wind energy systems. *Journal of Dynamic Systems, Measurement, and Control*, pages 071005–12, 2017.

[30] Islam I Hussein, David Olinger, and Gretar Tryggvason. Stability and control of ground tethered energy systems. In *AIAA Guidance, Navigation, and Control Conference, 2001*, Portland, OR.

[31] Matthew W Isaacs, Jesse B Hoagg, Islam I Hussein, and David Olinger. Retrospective cost adaptive control for a ground tethered energy system. In *50th IEEE Conference on Decision and Control and European Control Conference (CDC-ECC), 2011*, pages 824–829, Orlando, FL, 2011. IEEE.

[32] Paul Williams, Bas Lansdorp, and Wubbo Ockels. Modeling and control of a kite on a variable length flexible inelastic tether. In *AIAA Guidance, navigation and control conference, 2007*, Boston, MA.

[33] Paul Williams, Bas Lansdorp, and Wubbo Ockels. Nonlinear control and estimation of a tethered kite in changing wind conditions. *Journal of Guidance, Control, and Dynamics*, 31(3):pp: 793–799, 2008.

[34] Paul Williams, Bas Lansdorp, Richard Ruiterkamp, and Wubbo Ockels. Modeling, simulation, and testing of surf kites for power generation. In *AIAA Modeling and Simulation Technologies Conference and Exhibit, 2008*, Honolulu, Hawaii.

[35] C. Vermillion and L. Fagiano. Electricity in the air: Tethered wind energy systems. *ASME Dynamic Systems and Control Magazine*, 2013.

[36] Chris Vermillion. Altitude and crosswind motion control for optimal power-point tracking in tethered wind energy systems with airborne power generation. In *ASME 2013 Dynamic Systems and Control Conference, 2013*, Munger Center Palo Alto, CA. American Society of Mechanical Engineers.

[37] U. Goersdorf J. Dibbern, D. Engelbart. Operational aspects of wind profiler radars. Report, World Meteorological Organization, 2003.

[38] N. Deve M. Boquet, P. Callard. Return on investment of a lidar remote sensing device. *DEWI MAGAZIN*, 37, August 2010.

[39] James F Manwell, Jon G McGowan, and Anthony L Rogers. *Wind energy explained: theory, design and application*. John Wiley and Sons, 2010.

[40] William D Bonner. Climatology of the low level jet. *Monthly Weather Review*,

96(12):833–850, 1968.

[41] H Mark Helfand and Siegfried D Schubert. Climatology of the simulated Great Plains low-level jet and its contribution to the continental moisture budget of the United States. *Journal of Climate*, 8(4):784–806, 1995.

[42] Ali Baheri, Shamir Bin-Karim, Alireza Bafandeh, and Christopher Vermillion. Real-time control using Bayesian optimization: A case study in airborne wind energy systems. *Control Engineering Practice*, 69:131–140, 2017.

[43] Lucy Y Pao and Kathryn E Johnson. Control of wind turbines. *IEEE Control Systems Magazine*, 31(2):44–62, 2011.

[44] Chris Vermillion, Trey Grunnagle, Ronny Lim, and Ilya Kolmanovsky. Model-based plant design and hierarchical control of a prototype lighter-than-air wind energy system, with experimental flight test results. *IEEE Transactions on Control Systems Technology*, 22(2):531–542, 2014.

[45] Kartik B Ariyur and Miroslav Krstic. *Real-time optimization by extremum-seeking control*. John Wiley and Sons, 2003.

[46] PJM Website. Estimated hourly load for pjm region, http://www.pjm.com/markets-and-operations/energy/real-time/loadhryr.aspx, 2016.

[47] Alireza Bafandeh and Chris Vermillion. Real-time altitude optimization of airborne wind energy systems using lyapunov-based switched extremum seeking control. In *American Control Conference (ACC), 2016*, Boston, MA, 2016. IEEE.

[48] Ted KA Brekken, Alex Yokochi, Annette Von Jouanne, Zuan Z Yen, Hannes Max Hapke, and Douglas A Halamay. Optimal energy storage sizing and control for wind power applications. *IEEE Transactions on Sustainable Energy*, 2(1):69–77, 2011.

[49] John E Pinder, James G Wiener, and Michael H Smith. The weibull distribution: a new method of summarizing survivorship data. *Ecology*, 59(1):175–179, 1978.

[50] Debasis Kundu and Mohammad Z Raqab. Generalized Rayleigh distribution, different methods of estimations. *Computational statistics and data analysis*, 49(1):187–200, 2005.

[51] J Marcus Jobe. *Lognormal Distributions: Theory and Applications*. Taylor and Francis Group, 1989.

[52] Haym Benaroya, Seon Mi Han, and Mark Nagurka. *Probabilistic Models for Dynamical Systems*. CRC Press, 2013.

[53] Tao Hong and Shu Fan. Probabilistic electric load forecasting: A tutorial review. *International Journal of Forecasting*, 32(3):914–938, 2016.

[54] Ibrahim Moghram and Saifur Rahman. Analysis and evaluation of five short-term load forecasting techniques. *IEEE Transactions on power systems*, 4(4):1484–1491, 1989.

[55] Tao Hong. *Short term electric load forecasting*. Ph.D. Dissertation, North Carolina State University, 2010.

[56] Martin T Hagan and Suzanne M Behr. The time series approach to short term load forecasting. *IEEE Transactions on Power Systems*, 2(3):785–791, 1987.

[57] PF Blackman. Extremum-seeking regulators. In *An exposition of adaptive control, 1962*, pages 36–50, London, 1962. New York: Macmillan.

[58] Charles Stark Draper and Yao Tzu Li. *Principles of optimalizing control systems and an application to the internal combustion engine*. American Society of Mechanical Engineers, 1951.

[59] IS Morosanov. Method of extremum control. *Automatic and Remote Control*, 18:1077–1092, 1957.

[60] Miroslav Krstić and Hsin-Hsiung Wang. Stability of extremum seeking feedback for general nonlinear dynamic systems. *Automatica*, 36(4):595–601, 2000.

[61] Hsin-Hsiung Wang and Miroslav Krstic. Extremum seeking for limit cycle minimization. *IEEE Transactions on Automatic Control*, 45(12):2432–2436, 2000.

[62] Darryl DeHaan and Martin Guay. Extremum-seeking control of state-constrained nonlinear systems. *Automatica*, 41(9):1567–1574, 2005.

[63] Scott J Moura and Yiyao A Chang. Asymptotic convergence through Lyapunov-based switching in extremum seeking with application to photovoltaic systems. In *American Control Conference (ACC)*, pages 3542–3548, Chicago, 2010.

[64] Scott J Moura and Yiyao A Chang. Lyapunov-based switched extremum seeking for photovoltaic power maximization. *Control Engineering Practice*, 21(7):971–980, 2013.

[65] Nicu Bizon. Energy harvesting from the FC stack that operates using the MPP tracking based on modified extremum seeking control. *Journal of Applied Energy*, 104(0):326–336, 2013.

[66] C. Manzie and M. Krstic. Extremum seeking with stochastic perturbations. *IEEE Transactions on Automatic Control,*, 54(3):580–585, 2009.

[67] Kihwan Kim, Cosku Kasnakoglu, Andrea Serrani, and Mo Samimy. Extremum-seeking control of subsonic cavity flow. *AIAA journal*, 47(1):195–205, 2009.

[68] Matthew Ellis, Helen Durand, and Panagiotis D Christofides. A tutorial review of economic model predictive control methods. *Journal of Process Control*,

24(8):1156–1178, 2014.

[69] James B Rawlings, David Angeli, and Cuyler N Bates. Fundamentals of economic model predictive control. In *51st Annual Conference on Decision and Control (CDC), 2012*, pages 3851–3861, Maui, HI. IEEE.

[70] Vahid Hemmati. *Investigation of weathering effects on performance of intumescent coatings used in fire protection of wood structures*. Thesis, ProQuest Dissertations Publishing, 2017.

[71] David Q Mayne, James B Rawlings, Christopher V Rao, and Pierre OM Scokaert. Constrained model predictive control: Stability and optimality. *Automatica*, 36(6):789–814, 2000.

[72] David I Mendoza-Serrano and Daniel J Chmielewski. Demand response for chemical manufacturing using economic MPC. In *American Control Conference (ACC), 2013*, pages 6655–6660, Washington DC. IEEE.

[73] Babak Bahrani, Vahid Hemmati, Aixi Zhou, and Stephen L Quarles. Effects of natural weathering on the fire properties of intumescent fire retardant coatings. *Fire and Materials*, 2018.

[74] Oluwasanmi Adeodu and Daniel J Chmielewski. Control of electric power transmission networks with massive energy storage using economic MPC. In *American Control Conference (ACC), 2013*, pages 5839–5844, Washington DC. IEEE.

[75] Wesley J Cole, David P Morton, and Thomas F Edgar. Optimal electricity rate structures for peak demand reduction using economic model predictive control. *Journal of Process Control*, 24(8):1311–1317, 2014.

[76] Rasmus Halvgaard, Niels Kjølstad Poulsen, Henrik Madsen, and John Bagterp Jørgensen. Economic model predictive control for building climate control in a smart grid. In *Innovative Smart Grid Technologies (ISGT), 2012*, pages 1–6, Washington, DC. IEEE.

[77] Tobias Gybel Hovgaard, Kristian Edlund, and John Bagterp Jørgensen. The potential of economic MPC for power management. In *49th IEEE Conference on Decision and Control (CDC), 2010*, pages 7533–7538, Atlanta, GA. IEEE.

[78] Benjamin P Omell and Donald J Chmielewski. IGCC power plant dispatch using infinite-horizon economic model predictive control. *Industrial and Engineering Chemistry Research*, 52(9):3151–3164, 2013.

[79] Laura Standardi, Niels Kjolstad Poulsen, John Bagterp Jorgensen, and Leo Emil Sokoler. Computational efficiency of economic MPC for power systems operation. In *Innovative Smart Grid Technologies Europe (ISGT EUROPE), 2013*, pages 1–5, Lyngby, Denmark. IEEE.

[80] David I Mendoza-Serrano and Daniel J Chmielewski. HVAC control using infinite-horizon economic MPC. In *51st Annual Conference on Decision and Control (CDC), 2012*, pages 6963–6968, Maui, HI. IEEE.

[81] Jingran Ma, Joe Qin, Timothy Salsbury, and Peng Xu. Demand reduction in building energy systems based on economic model predictive control. *Chemical Engineering Science*, 67(1):92–100, 2012.

[82] Jingran Ma, S Joe Qin, Bo Li, and Tim Salsbury. *Economic model predictive control for building energy systems*. IEEE, 2011.

[83] Chris Vermillion, Trey Grunnagle, and Ilya Kolmanovsky. Modeling and control design for a prototype lighter-than-air wind energy system. In *American Control Conference (ACC), 2012*, pages 5813–5818, Montreal, Canada, 2012. IEEE.

[84] Shamir Bin-Karim, Alireza Bafandeh, Ali Baheri, and Christopher Vermillion. Spatiotemporal optimization through gaussian process-based model predictive control: A case study in airborne wind energy. *IEEE Transactions on Control Systems Technology*, PP, Issue: 99 :1 – 8, 2017.

[85] Alireza Bafandeh, Shamir Bin-Karim, Ali Baheri, and Christopher Vermillion. A comparative assessment of hierarchical control structures for spatiotemporally-varying systems, with application to airborne wind energy. *Control Engineering Practice*, 74:71–83, 2018.

[86] Donald E Kirk. *Optimal control theory: an introduction*. Courier Corporation, 2012.

[87] Martin L Puterman. *Markov decision processes, discrete stochastic dynamic programming*. John Wiley and Sons, 2014.

[88] Alireza Bafandeh, Shamir Bin-Karim, and Chris Vermillion. Fused local-global control of spatiotemporally-varying systems, a case study in airborne wind energy. In *IEEE Conference on Control Technology and Applications (CCTA)*, Kohala Coast, Hawaii, 2017.

[89] Ying Tan, D Nesic, Iven MY Mareels, and Alessandro Astolfi. On global extremum seeking in the presence of local extrema. *Automatica*, 45(1):245–251, 2009.

[90] Alireza Bafandeh and Chris Vermillion. Altitude optimization of airborne wind energy systems via switched extremum seeking–design, analysis, and economic assessment. *IEEE Transactions on Control Systems Technology*, PP(99):1–12, 2017.